Phase Transformations in Layered Electrode Materials for Sodium Ion Batteries

by

Alexandra Jeanne Toumar

Submitted to the Department of Materials Science and Engineering
in partial fulfillment of the requirements for the degree of

Doctor of Philosophy in Materials Science and Engineering

at the

MASSACHUSETTS INSTITUTE OF TECHNOLOGY

June 2017

© Massachusetts Institute of Technology 2017. All rights reserved.

Author . . . .
Department of Materials Science and Engineering
March 29, 2017

Certified by . . . .
Gerbrand Ceder
Professor
Thesis Supervisor

Accepted by . . . .
Donald Sadoway
Chairman, Department Committee on Graduate Theses

Phase Transformations in Layered Electrode Materials for Sodium Ion Batteries

by

Alexandra Jeanne Toumar

Abstract

In this thesis, I investigate sodium ion intercalation in layered electrode materials for sodium ion batteries. Layered metal oxides have been at the forefront of rechargeable lithium ion battery technology for decades, and are currently the state of the art materials for sodium ion battery cathodes in line for commercialization. Sodium ion intercalated layered oxides exist in several different host phases depending on sodium content and temperature at synthesis. Unlike their lithium ion counterparts, seven first row layered TM oxides can intercalate Na ions reversibly. Their voltage curves indicate significant and numerous reversible phase transformations during electrochemical cycling. These transformations arise from Na-ion vacancy ordering and metal oxide slab glide but are not well understood and difficult to characterize experimentally. In this thesis, I explain the nature of these lattice differences and phase transformations for O and P-type single-transition-metal layered systems with regards to the active ion and transition metal at hand.

This thesis first investigates the nature of vacancy ordering within the O3 host lattice framework, which is currently the most widely synthesized framework for sodium ion intercalating oxides. I generate predicted electrochemical voltage curves for each of the Na-ion intercalating layered TM oxides using a high-throughput framework of density functional theory (DFT) calculations and determine a set of vacancy ordered phases appearing as ground states in all Na_xMO_2 systems, and investigate the energy effect of stacking of adjacent layers. I also examine the influence of transition metal mixing and transition metal migration on the materials' thermodynamic properties.

Recent work has established the P2 framework as a better electrode candidate structure type than O3, because its slightly larger interlayer spacing allows for faster sodium ion diffusion due to lower diffusion barriers. However, little has been resolved in explaining what stabilizing mechanisms allow for the formation of P-type materials and their synthesis. This work therefore also investigates what stabilizes P2, P3 and O3 materials and what makes them synthesizable at given synthesis conditions, both for the optimization of synthesis techniques and for better-guided material design. It is of further interest to understand why some transition metal oxide systems readily

form P2 or P3 compounds while others do not. I investigate several possible stabilizing mechanisms that allow P-type layered sodium metal oxides to by synthesized, and relate these to the choice of transition metal in the metal oxide structure.

Finally, this work examines the difficulty of sodium ion intercalation into graphite, which is a commonly used anode material for lithium ion batteries, proposing possible reasons for why graphite does not reversibly intercalate sodium ions and why co-intercalation with other compounds is unlikely. This thesis concludes that complex stabilizing mechanisms that go beyond simple electrostatics govern the intercalation of sodium ions into layered systems, giving it advantages and disadvantages over lithium ion batteries and outlining design principles to improve full-cell sodium ion battery materials.

Thesis Supervisor: Gerbrand Ceder
Title: Professor

Acknowledgments

I'd like to thank my committee, Professors Jeff Grossman and Silvija Gradečak, for their cheerful and expansive support and advice. Thank you goes also to my advisor Gerd Ceder for his continued mentorship and guidance, and his encouragement at times when I needed it most. His unique combination of cleverness, humor, conversational and management skills made for an exciting and valuable PhD journey, and I look forward to chatting about life and science with him over Belgian beers for many years to come. I am very grateful to past and present members of the Ceder group for their teaching, collaborations and their moral support throughout the years, especially occupants of 13-5041 at MIT and those that continued the MIT tradition when the group transplanted to Berkeley, California. In particular I'd like to thank Will Richards and Ian Matts, who started in the Ceder group at the same time as I did, and whose friendship, collaboration and support was indispensable.

I want to thank the members of various committees, volunteer groups, and clubs, official and unofficial, that made my time at MIT so much more rewarding than just the work presented in this thesis can show. In particular, I want to thank fellow members and colleagues in Graduate Women at MIT, the Graduate Materials Council, the Title IX Student Working Group, Sexual Misconduct Education and Prevention Task Force, MIT iREFS, MIT Volunteer Consulting Group, Women of Materials Science, the Edgerton Center, MADMEC, and the staff at the Thirsty Ear Pub, who normalized drinking to excess in the most healthy, supportive and convivial way possible. I'd also like to thank people to played various supporting roles for us graduate students at MIT and beyond, particularly Kathy Simons, Alice Muller, Angelita Mireles, Elissa Haverty and Mike Tarkanian. Thank you also goes to Carolyn, Ayelet and Maria, who helped me through dark times in my personal life that would have otherwise impaired my ability to persevere in my work, and reminded me of the value of perspective.

I want to thank my family for their support from afar, their acceptance of me missing special occasions for many years to follow my vague ambitions, and for only

rarely asking when it is I will finally graduate.

Lastly, I could not have survived the last five-odd years without my incredible, amazing, glorious friends. My friends at home in New Zealand and in various parts of the globe reminded me of the great big world out there beyond the walls of MIT, and kept me laughing, cheerful and content. There are too many to list by name, but I'd like to thank Emjay, Martin, Simon, Julia, George, Nina, Karen, and Vera, whose presents, postcards and pick-me-ups I still proudly display on my wall and in my office. I am so grateful for the friends that helped me during my transition from the East to the West Coast, James, Natalie, Nadja, Harold, Elizabeth, Haley and the rest. Finally, my heart swells with love and appreciation for my amazing friends in DMSE, especially Dina Yuryev, Brent Keller, Michelle Sing, and Corentin Monmeyran, who will continue to be my best friends for years to come. Thank you all.

Contents

List of Figures

14

17

List of Tables

Chapter 1

Introduction

1.1 Motivation

Rechargeable battery technology has become increasingly prominent in the 20th and 21st centuries with a worldwide surge in demand for communications technology, electric appliances, vehicles and portable electronics. Large scale electrochemical energy storage is also growing in importance as more of the world turns to intermittent renewable energy sources such as solar and wind for sustainable energy. Several rechargeable battery technologies have emerged and become commercially available in the last century, as seen in Fig. 1-1, each with their own particular functional, safety and production drawbacks. Lithium ion battery technology has been leading the field in high-energy-density energy storage for portable applications for over 40 years, with an exemplary energy density that allows for highly mobile and versatile applications. However with increasing demand lithium precursor materials are growing in cost. Additionally, the highest energy density lithium ion battery cathodes utilize cobalt, which is not globally abundant and costly to source, and they require the use of copper as a current collector on the anode side, while cheaper aluminum can be used in sodium ion cells[14].

Sodium ion battery technology is conceptually similar to lithium ion battery technology and can utilize the processing capabilities already in place for producing commercial lithium ion batteries. Similarly to lithium ion batteries, sodium ion batteries

can use layered transition metal oxides as the active material for their cathodes. For layered oxide morphologies, a wider chemical space of transition metal oxides has been found to reversibly cycle sodium ions than lithium ions, thereby presenting a larger field in which to search for potential electrode materials that do not necessarily utilize cobalt. Sodium ion battery materials present different challenges, however. The standard electrode potential of sodium compared to that of lithium means the intercalation voltage is inherently lower, all else being equal. While the technology is still in its infancy, extensive study is needed to understand the differences between sodium and lithium ion battery technology, as well as the potential pitfalls, advantages and design principles of sodium ion battery electrode materials. Though experimental synthesis and characterization may be guided to some extent by previous work conducted on lithium ion materials, computational materials science has a significant advantage for determining functional properties of new materials in a deliberate and high-throughput manner. Combining the speed and accuracy of first principles calculations can lead us to understand these active materials on an atomic scale, as well as to draw design principles from trends we see in numerous computational studies over large chemical spaces.

1.2 Alkali-ion rechargeable battery technology

A rechargeable (secondary) alkali-ion battery cell consists of two electrodes with an electronic-insulating electrolyte sandwiched in between. It stores chemical energy reversibly by means of an electrochemical oxidation-reduction (redox) reaction. The anode or negative electrode gives up electrons to the external circuit and is oxidized during discharge, while the cathode ("positive") electrode accepts electrons and is reduced during discharge. [15] During charging of rechargeable batteries, of course, these redox reactions are reversed, but for ease and consistency, the terms cathode and anode are still used for their respective components.

The electrolyte separates the two electrodes and is an ionic conductor and electronic insulator. It provides a medium to transfer charge in the form of "working
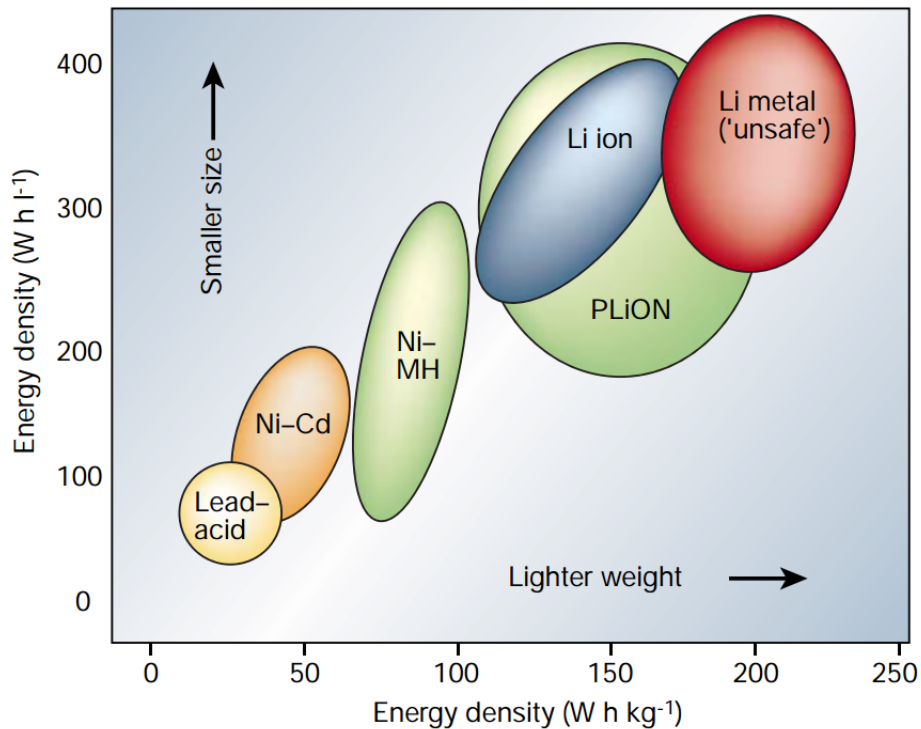
Figure 1-1: A schematic depicting different types of battery technologies with respect to volumetric and gravimetric energy densities. Except for lithium metal batteries, it summarizes the secondary battery types which are currently commercially available: lead acid, nickel-cadmium (Ni-Cd), nickel metal-hydride (Ni-MH), lithium-ion (Li-ion), and plastic lithium-ion (PLiON). Originally published by Tarascon and Armand [1].

ions" (lithium or sodium ions for example) between the electrodes during charge and discharge. In conventional lithium and sodium ion batteries, the electrolyte is usually a liquid solvent with dissolved salts which provide ionic conductivity, however solid state electrolytes for rechargeable alkali ion batteries have been developed in recent years[16].

In an alkali cell, the electrochemically active cathode material is typically mixed with carbon to provide electronic conductivity and electrons are collected by current collectors at both electrodes. Thus, the electrodes are electronic conductors and when connected to an external circuit, the battery can be charged or discharged depending on whether a (positive) voltage is applied. Taking a standard, commercial lithium ion cell as an example, a charged lithium cell will have the majority of the lithium (working) ions intercalated in the anode (typically graphite). When the circuit is completed without a positive applied voltage, the cell will discharge by shuttling lithium ions through the electrolyte and the electrons through the external circuit to intercalate into the cathode (often a layered cobalt oxide). When the circuit is broken in the charged state, the separation of charges acts as the electrochemical energy storage[17]. In standard lithium ion batteries, and the sodium ion batteries discussed in this thesis, the energy "stored" in the electrode materials results from the standard electrode potential of the working ion intercalated into the anode, as well as the oxidation of the transition metal ions in the cathode lattice.

The main components in an alkali-ion rechargeable cell, as well as their direction of movement during charge and discharge, are shown in Fig. 1-2.

1.2.1   Functional Properties of Alkali-Ion Rechargeable Batteries

Rechargeable batteries have several functional properties that will be referenced throughout this thesis. The overall reaction of a rechargeable alkali-ion battery with a pure metal anode can be written:
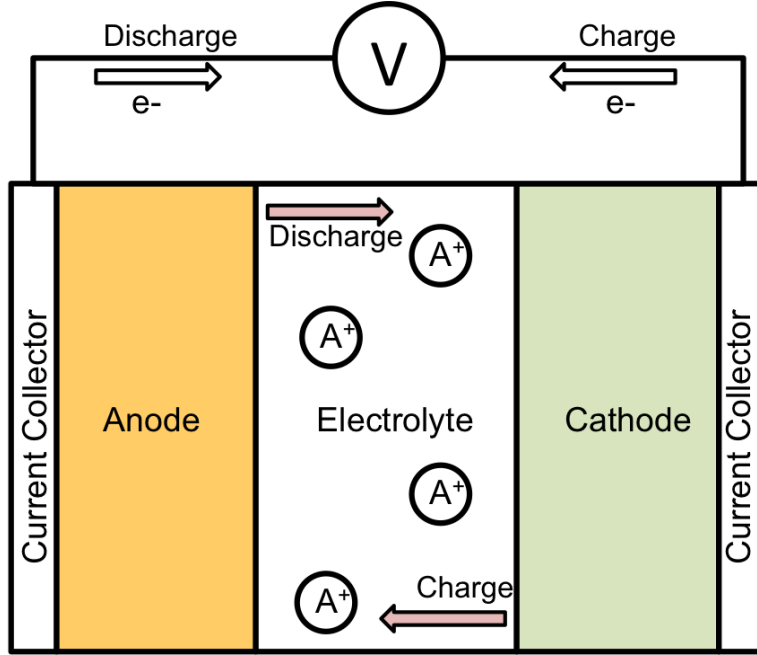
Figure 1-2: Schematic representation of an alkali-ion battery cell (e.g. lithium or sodium ion) with major active components shown.

$$A_{n-x}(s) + xA(s) \leftrightarrow A_n H \qquad (1.1)$$

Where x is the amount of the alkali ion A^+ which is intercalated into the solid host crystal structure $A_n H$. The forward reaction indicates discharge while the backward reaction is charge.

The *voltage* or *potential* of the cell is determined by the energy difference of the electrochemical reactions occurring in the active materials in the cell, i.e. the difference in energy of the working ion intercalated into the anode versus the working ion intercalated into the cathode. The open circuit voltage is governed by the chemical potentials of the alkali ion via the Nernst equation.

$$voltage = -\frac{\mu^c - \mu^a}{z \cdot F} \qquad (1.2)$$

Where μ^c and μ^a are chemical potentials of the working ion in the cathode and anode respectively (both in joules per mole), z is the working ion valence (+1 for Li, Na or other Group 1 ions) F is the Faraday constant (98,485 Coulombs per mole).

The *reversible capacity* of a battery electrode is the amount of active ion which can be reversibly shuttled between the cathode and the anode. The reaction at the electrode is determined by the nature of the active ion and the electrode material, but generally the active ion can alloy with, chemically react with (conversion), or intercalate into the electrode. The specific capacity of the electrode material in Ampere-hours is derived from the equivalent weights of the active reactants.

$$capacity = \frac{z \cdot N}{3600 \cdot M} \tag{1.3}$$

Where N is the number of working ions moved between electrodes, M is the molecular weight of the electrode material in grams per mole, z is the valence of the working ion and 3600 is a conversion factor. This gravimetric capacity can be related to volumetric capacity by way of density of the active material. The theoretical capacity of a material is the specific capacity computed with all of the working ion reversibly intercalated. This is the upper limit for the capacity of an electrode material and is not typically reached in practice as the structural relaxation of the material leads to irreversible phase transformations away from the topotactic structure needed for reversible cycling. The specific capacity of the cell refers to the actual amount of active ion reacted or intercalated reversibly, and usually changes during electrochemical cycling as the materials degrade or fail over time or as a solid electrolyte interfacial (SEI) layer is formed[18].

The *rate capability* of a battery electrode is the rate at which it can be charged or discharged while still retaining usable capacity. For a battery to exhibit good rate capability, the ionic and electronic conductivity must be good throughout the electrode materials, and the electrolyte must have high ionic conductivity while being an electronic insulator. For a liquid electrolyte, ionic conductivity is very fast and

not seen as a limiting factor. Electronic conductivity is improved in the electrodes by mixing the active material with carbon, as mentioned above, or by doping of the active material, and will not be discussed extensively in this thesis. Ionic conductivity (and diffusivity) through a (crystalline) solid is the common limiting factor to a battery cell's rate capability. The intrinsic ionic diffusivity in an active material is dependent on the chemical make up of the material, the size and valence of the working ion, the available diffusion pathways and the diffusion mechanism. For lithium ion layered oxides, for example, the diffusion mechanism involves migration of alkali ions through tetrahedral sites neighboring octahedral sites[19]. Percolating pathways for the working ion are needed for the material to work, and these are characterized by their dimensionality, with layered transition metal oxides characterized as two-dimensional pathway materials[20]. Practically, smaller particle sizes of active material can improve the rate capability of a cell because they give the active or working ions a smaller distance to traverse to reach the material surface [21].

Cost and safety are also significant to consider in battery material design, though they are not strictly functional properties of battery materials. Sodium ion precursors are typically cheaper and much more abundant than lithium ion precursors for comparable applications. More significant still is the cost of transition metal used, making cheap, abundant transition metals such as Fe, Mn and Ni preferable to Co, which is frequently used as an active component in lithium ion batteries[22, 23].

As the field of applications expands, rechargeable battery safety is also becoming a prominent concern. Batteries must be safe in order to be used in any practical applications, even at the cost of other performance and production metrics. Metal anodes, described in Chapter 4, are considered unsafe because of the low melting points of sodium and lithium as well as the propensity for dendritic growth over repeated cycling, which can short-circuit a battery, heating it up to unsafe temperatures. Until these risks can be adequately mitigated by technological advances, such as reliable thin film coating, lower density anodes must be used, typically carbonic anodes in both sodium and lithium ion batteries. In cathodes, safety concerns relate to the decomposition of active materials at high voltages, which can lead to oxygen

gas evolution, which in itself can react with commonly used battery electrolytes to cause thermal runaway and, in extreme cases, explosions[24, 25].

1.3 Sodium Ion Batteries

1.3.1 Sodium layered transition metal oxides

Layered transition metal oxides have been studied since the 1970s as potential electrode materials for sodium ion batteries, and have had a recent resurgence as the highest energy density materials currently available for this application. Sodium ion batteries have been highlighted in recent years for their potential as an inexpensive, geopolitically neutral alternative to Li-based rechargeable batteries, largely due to the global abundance and low cost of sodium-containing precursor materials [26, 27]. There is increasing interest in sodium, with several companies around the world beginning to prototype and commercialize sodium ion batteries, such as Faradion in the United Kingdom and Aquion and Valence Technologies in the United States[28]. Compared to their lithium ion counterparts, sodium ion batteries in similar transition metal oxide environments tend to have lower voltages and a steeper voltage curve with several apparent first order phase transitions as shown in the layered CoO_2 framework in Fig. 1-3. In general, sodium ion cathode voltages are lower than those of their lithium ion counterparts in numerous chemical compounds as shown in Fig. 1-4 due to the difference in standard electrode potential for sodium and lithium ions (-2.71 and -3.04 V respectively).

Layered TMOs maintain their layered configuration as alkali ions are repeatedly shuttled in and out of their layers, with the percentage of reversibly cycle-able alkali content (reversible capacity) determined by the layered structure, transition metal selection, cycling rate and alkali ion. Fig. 1-5 shows a comparison of energy densities for known lithium and sodium ion layered and polyanionic cathode materials.
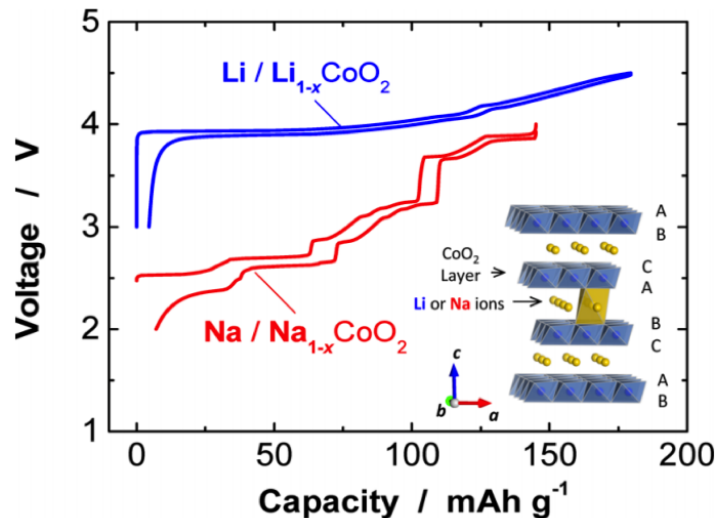
Figure 1-3: Comparison of charge and discharge voltage curves for $O3\text{-}Na_xCoO_2$ and $O3\text{-}Li_xCoO_2$ with inset depiction of crystal structure with octahedral alkali sites. Originally published by Yabuuchi et al.[2]
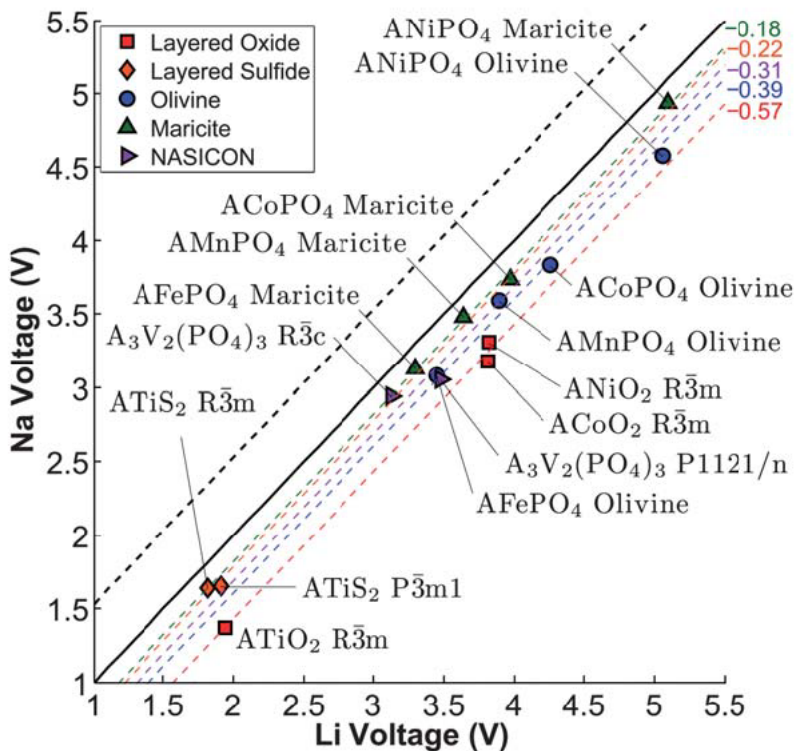
Figure 1-4: Comparison of calculated Na and Li voltages for a variety of known crystal structures. The black dashed line indicates the +0.35V difference in the standard electrode potentials of Na and Li, while the colored dashed lines indicate the fitted average voltage difference $\Delta\,V_{Na\text{-}V}$ between Na and Li containing crystal structures for that structure type. Originally published by Ong et al.[3]
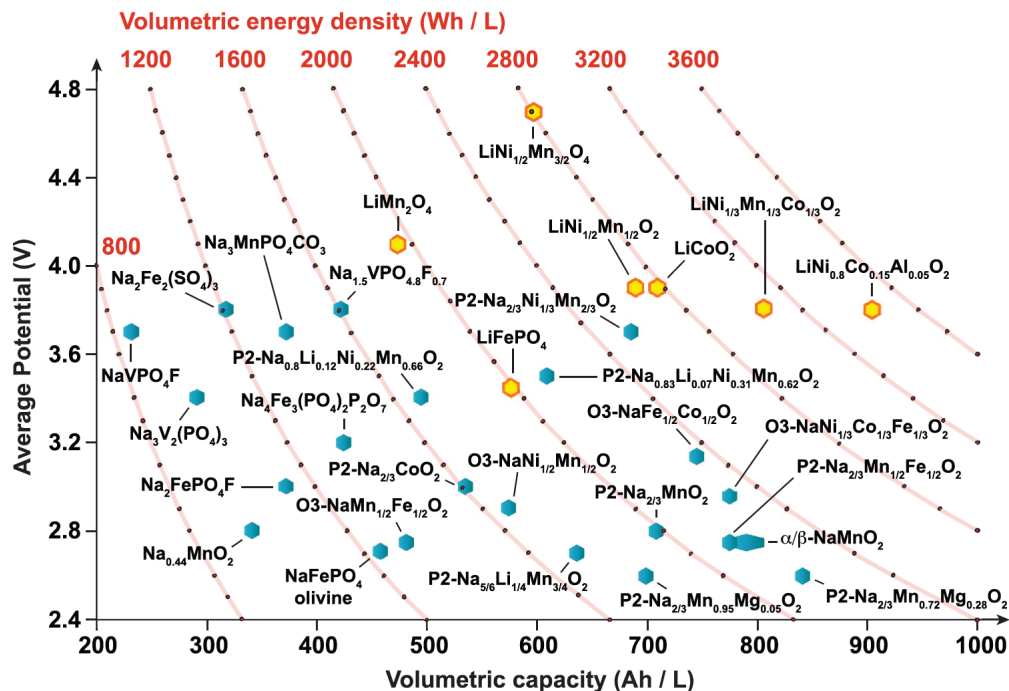
Figure 1-5: Collection of cathode materials for Li and Na ion batteries. Originally published by Clément et al.[4]

1.3.2 Electronic structures and physical properties of first row transition metals

Redox reactions of transition metals are the most significant energy storage mechanism in alkali ion cathode materials. First row ($3d$ series) transition metals are compared throughout this thesis, and thus it is useful to understand their electronic and ionic properties in order to understand the trends and variations we discover. Transition metals refer to three series of elements that make up the short groups in the periodic table and are described by the filling of shells of d orbitals across each series ($3d$, $4d$ and $5d$). First row transition metals hereafter refer to the seven members of the $3d$ series that lie between Ti and Cu in the periodic table[29].

When a transition metal ion is surrounded by an octahedral arrangement of six negative ions (in the case of this thesis, we mainly speak of oxide ions), its five d orbitals are split into two groups, the lower energy three t_{2g} orbitals and the higher energy two e_g orbitals[30, 31]. In transition metal oxides found in this work, the
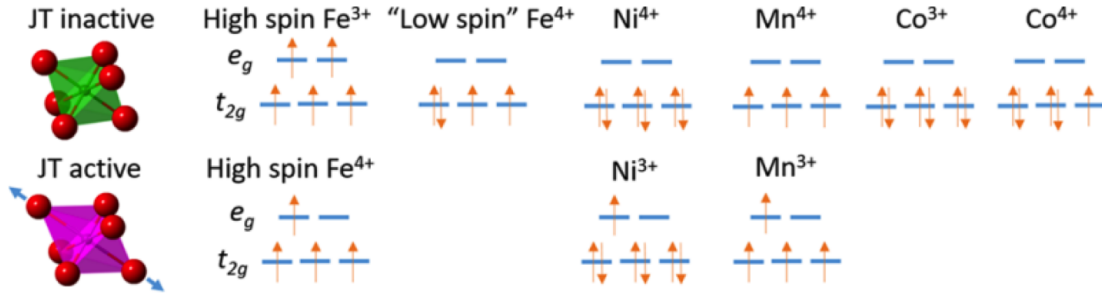
Figure 1-6: Low and high spin octahedral complexes for first row transition metals. Fe4+, Ni3+ and Mn3+ are Jahn-Teller active due to a degeneracy in their electron configurations. [5]

average transition metal ion oxidation state during electrochemical cycling ranges between 3+ and 4+, with a few exceptions for mixed transition metal systems. For example, a transition metal may donate an electron to a neighboring transition metal in a mixed system which has tendency to reduce, such as Ni, which typically appears as 2+ in mixed transition metal oxide systems [11]. Some octahedral complexes with low-spin electronic configurations as shown in Figure 1-6 have degenerate electronic orbitals and are deemed Jahn-Teller active or Jahn-Teller unstable, meaning they are driven to distortion from perfect octahedral symmetry[32]. A Jahn-Teller distortion in an octahedral configuration typically leads to a loss of symmetry in the crystal, as it results in the elongation of the octahedron along one axis[33, 34, 9, 5]. In this thesis, Jahn-Teller distortion is considered for Ni3+ and Mn3+ ions and taken into account when initializing relaxation calculations for structures containing these ions (Jahn-Teller distortion is considered weak for Fe4+ ions and is not discussed extensively in this thesis).

1.3.3 Phase transitions of sodium ion layered oxide cathodes

Conceptually, electrochemical cycling of layered transition metal oxide materials is seen as topotactic, meaning the crystal structure containing the working ion does not change as it (de-)intercalates. In reality, however, the structure remains unchanged only in the sense that it retains its layered formation, and in fact it undergoes sig-

nificant structural relaxation often accompanied by numerous structural phase transitions.

During electrochemical cycling, sodium ion layered oxides undergo several types of reversible and irreversible phase transitions. As sodium de-intercalates, the remaining sodium and vacancies rearrange themselves into patterns within the sodium layers to form ordered structures.[35] This is a reversible first order phase transition and is seen as a step and plateau on the electrochemical cycling voltage curve, as apparent in Figure 1-3.

Sodium layered transition metal oxides (as well as those containing larger alkali ions such as potassium[36] can also undergo slab-glide transformation, which refers to the coordinated translation of adjacent metal oxide layers to change the shape of the site in which the sodium ion sits. The majority of known layered sodium ion transition metal oxides (as well as all layered lithium transition metal oxides) are synthesized as stoichiometric AMO_2 (where A is the alkali) in the O3 configuration, which indicates octahedral alkali sites and oxygen stacking which repeats with every three sodium layers, and corresponds to the $R\bar{3}m$ crystal space group. According to the notation developed by Delmas et al, O3-type materials can transform (glide) to P3-type materials and vice versa[6].

Sodium layered oxides can also be synthesized at partial sodium ion content in the P2 configuration, typically with the $P6_3/mmc$ space group. Similarly to the O3 materials, P2 materials can reversibly transform to O2 materials and vice versa through slab glide[6], as can be seen in Figure 1-7. While O3 can be transformed into P2 at high temperature, a transformation at operating temperatures between O3 and P2 is not likely, as it cannot be achieved by pure slab glide and requires the breaking of metal oxygen bonds[37]. For all these structures, a phase with a loss of symmetry through lattice distortion or sodium ion removal (to a monoclinic phase) is indicated with a "prime" symbol, O3 becoming O'3, for example in O'3-NaMnO$_2$ which has a monoclinic distortion due to the Jahn-Teller distortion in the MnO$_6$ octahedra containing Mn3+ ions[38].
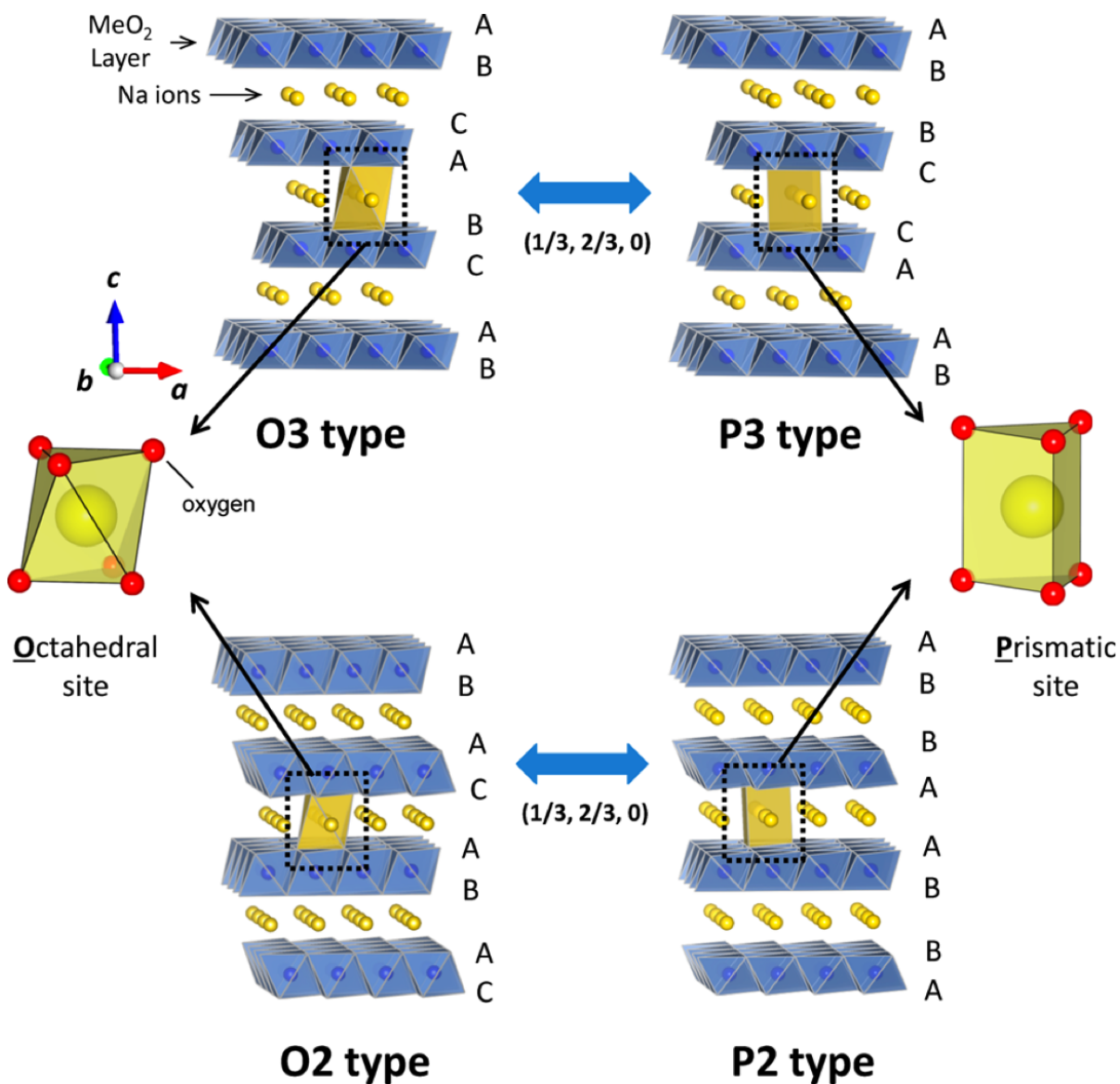
Figure 1-7: Possible layer stacking of sodium ion layered transition metal oxides, according to the naming convention coined by Delmas et al[6]. O3 can reversibly transform by a translation or glide of the metal oxide layers in the a and b lattice directions to P3, and P2 can do so to the O2 structure. A, B and C indicate oxygen layers which repeat in the vertical c lattice direction. Originally published by Yabuuchi et al.[2]

1.4 First Principles Computational Materials Design for Rechargeable Battery Materials

Macroscopic materials properties ranging from thermodynamic stability to mechanical properties to appearance can be ascribed to quantum mechanical phenomena in many-atom, many-electron systems. Until recent decades, the quantum mechanical approach to materials science and engineering was not accessible to researchers and materials designers, as the Schrödinger equation is not analytically solvable for such systems. This has changed with powerful advances in computation[39]. With the on-set of first principles computer simulations, one could begin applying quantum mechanical insights to solid systems, thereby vastly increasing the physical insight into materials and allowing for efficient materials design. Though such calculations are computer simulations, they can perhaps be better thought of as computational experiments, because they derive results from first principles and not from extrapolation or interpolation of empirically derived models.

Relevant battery material properties can be related to structural components of the material which can in turn be computed using first principles methods. In the Ceder Group, formerly at MIT and currently at UC Berkeley and Lawrence Berkeley National Laboratory, a comprehensive codebase and internal computer cluster set up allows for high throughput computing and data-mining of material properties, as well as in-depth analysis of individual known and hypothetical compounds.

1.4.1 Density Functional Theory for Battery Materials

A popular way to apply first principles techniques without sacrificing large computational costs is density functional theory (DFT). DFT is an approach to solving the Schrödinger equation which treats all electronic wave-functions in a system as a functional of spatially dependent electronic density. [40] This starts with the Born-Oppenheimer approximation, which treats the electrons and nuclei of an atom as separate and distinct, with the nuclei treated as heavy, fixed points in the atom[41].

DFT is powerful due to its balance of accuracy and efficiency, and when approximations are chosen correctly and consistently, it can give important insights into material properties on an atomistic level.

An acceptably accurate DFT calculation for a solid material requires for the materials problem to be translated into an atomistic model, computed with the correct chosen approximations for its specific requirements and validated by experimental results. From these energy calculations, several properties are derived, including thermodynamic stability, which is represented as the distance above an energy hull. Other properties, such as spatial charge distribution, electronic density of states, magnetic moments and band structure are easily gleaned from DFT calculations.

1.4.2 Application of Density Functional Theory

DFT energy calculations throughout this work are performed using the Vienna Ab initio Simulation Package (VASP) [42] within the projector-augmented wave approach[43]. The Perdew-Burke-Ernzerhof (PBE) exchange-correlation functional is used to address self-interaction. The generalized gradient approximation (GGA) and the +U correction are mainly utilized in this thesis[44].

U Value Determination and Magnetic Moment Selection

The Hubbard U value in the Hamiltonian is used to open up a Hubbard gap in band structure, effectively localizing electronic density to transition metals, and therefore has a meaningful effect on the energy. The U value removes self-interaction in metal d orbitals, leading to strong charge localization and significant changes in ground state structures. The self-interaction error is the incomplete cancellation of the non-physical electron self-interaction when an electron is transferred between significantly different environments. The U value can be determined by self-consistent linear response theory (calculating how occupation of TM orbitals changes with local potential) or by fitting to experimental oxidation energies[45, 46].

In Wang's 2006 study, GGA was found to overestimate oxidation energies due to an

overestimation of the binding strength in the O_2 molecule and a correlation error in $3d$ orbitals. Oxidation energies found with GGA were compared to experimental values, and consistently found to be less negative, so the U correction was fit to the formation enthalpies of non-transition metal oxides such as MgO[45]. While the accuracy of U values depends on the system at hand, those fit by Wang et al were found to be remarkably consistent in predicting oxidation energies for transition metals, and are used throughout this thesis for the sake of consistency and reproducibility.

Table 1.1: U Values for Seven First Row Transition Metals in an Oxide Environment

Element (Oxide Env.)	U value (eV)
Ti	0.0
V	3.1
Cr	3.5
Mn	3.9
Fe	4.0
Co	3.4
Ni	6.0

Magnetic moments of Co^{3+}, Co^{4+}, Ni^{3+} and Ni^{4+} ions are initialized throughout the work as low spin, which has been previously determined to improve energy convergence. U corrections for the transition metals in an oxide environment optimized in a previous work are tabulated in Table 1.1 [47]. A U correction is not assigned for calculations in the Ti system, to better represent the delocalized nature of electrons in reduced Ti oxides[47]. The average intercalation potential of the cathode can then be obtained using energies computed within DFT using the following equation[48, 3],

$$V = -\frac{E(A_nH) - E(A_{n-x}H) - xE(A)}{xe} \qquad (1.4)$$

where A is the alkali ion, H is the host structure and e is the electronic charge. DFT energy calculations can be time-consuming, particularly for large supercells (e.g. with hundreds of atoms). To make energy calculations considerably faster and to enable the computation of free energy at finite temperatures, the total energy Hamiltonian can be parametrized in terms of the occupancies of sites on the crystal lattice in question by fitting effective interaction coefficients for clusters of sites. This method

is called a cluster expansion and is described in the following section.

1.4.3 Cluster Expansion and Monte Carlo Methods

A cluster expansion (CE) is a generalized Ising model method[49]. Thermodynamic material properties such as total energy are expanded in a cluster expansion in terms of the occupancy of the sites in the crystal lattice[50, 51, 52]. The Ising Hamiltonian is given by:

$$H = \sum_{\alpha} J_{\alpha}\sigma_{\alpha} \tag{1.5}$$

$$\sigma_{\alpha} = \sigma_i\sigma_j...\sigma_l, l \in \alpha \tag{1.6}$$

Where σ_{α} is the product of all spins in a collection of lattice sites called a cluster α, and J_{α} is the effective interaction for the cluster. The spin variable σ_p for a lattice site p can have two values, up (+1) or down (-1) which lends itself well to studying configurations of ionic arrangements on lattice sites which can either be empty or occupied. Thus, the total energy for an atomic configuration σ can be expanded as:

$$E(\sigma) = E_0 + \sum_{\beta} J_{\beta}\sigma_{\beta} \tag{1.7}$$

Where each product in the summation is a product of occupancy values for all possible sizes of clusters (single site, double, triplet etc.). Though the Hamiltonian is a summation of all possible clusters on a lattice in a periodic crystal structure, in practice this sum is truncated to those clusters that have the most significant effective cluster interactions (ECIs). Once the energy of the system is parametrized in this linear way and the ECIs are determined accurately, energy computational time is reduced dramatically. Finding the energy of any given composition or configuration of ions on the lattice becomes very simple and allows one to identify the lowest energy "ground state" configurations with ease.

A CE allows for the implementation of Monte Carlo methods, which can be used to calculate finite temperature thermodynamics and predict composition-temperature phase diagrams. The accuracy of the cluster expansion is strongly dependent on the accuracy and size of the initial dataset from which it is created as well as the sampling method. A systematic error in a dataset created from DFT calculations leads to a completely inaccurate CE, for example. In this thesis, CE fitting is conducted using the compressive sensing method[53] as well as quadratic programming, and utilizes Ewald summation of ionic systems for higher fitting accuracy.

1.4.4 Computational Methods for Predicting Diffusivity Mechanisms

Nudged elastic band (NEB) calculations allow for the determination of transition state barriers which can then be calibrated to estimate the ease of diffusion between neighboring sites[54]. Fig. 1-8 shows NEB profiles for the transition of the working ion between two sites in different crystalline systems. The maximum height of the profile indicates the diffusivity barrier in the crystal, and can thus be related back to the rate capability of the battery. In transition metal oxides, diffusion barriers of around 500 meV or lower are typically required for the material to be a viable electrode.

Abinitio molecular dynamics utilize density functional theory calculations to perform molecular dynamics simulations. This is a computationally expensive but effective method, particularly when the diffusion pathways of an ion are not known. Figure 1-9 shows the simulated pathways of sodium ion migration in P2 $Na_{0.56}CoO_2$, achieved by molecular dynamics simulations conducted at non-dilute sodium ion concentrations.
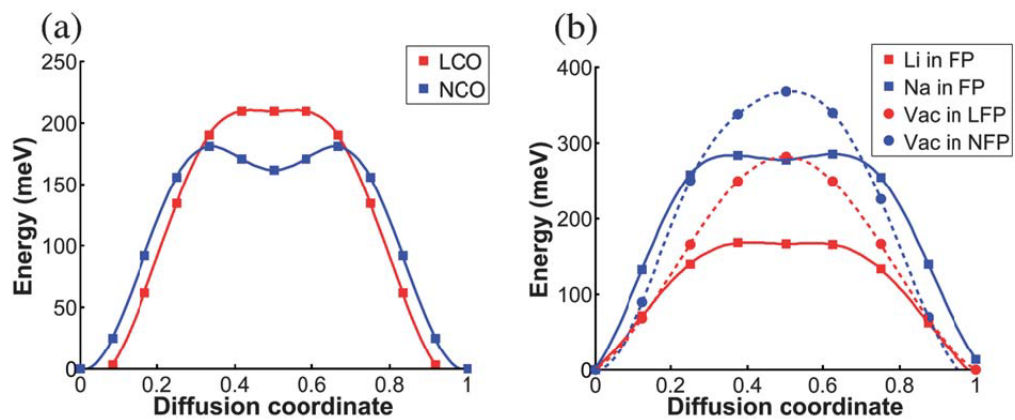
Figure 1-8: Comparison of NEB results for alkali diffusion in O3-type Na_xCoO_2 and Li_xCoO_2 with inset depiction of crystal structure with octahedral alkali sites. Originally published by Ong et al.[3]
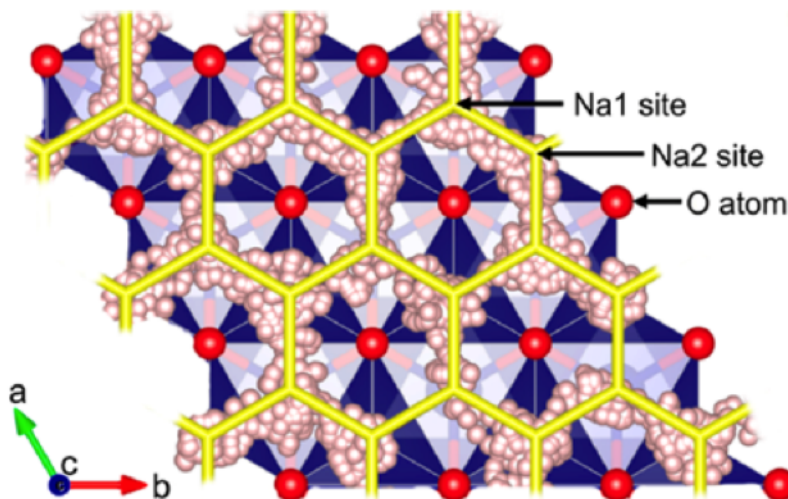
Figure 1-9: Ab initio pathways of sodium ions within a P2-type layered oxide layer. Originally published by Mo et al.[7]

1.5 Experimental Synthesis and Characterization

Computational materials design is only useful if it leads to the synthesis and testing of novel and improved functional materials. Therefore, in this thesis, first principles computational results are verified using known experimental techniques. Experimental synthesis and characterization measurements throughout this thesis is conducted by collaborators or quoted from the established literature.

1.5.1 Synthesis methods for predicted materials

The majority of alkali-intercalating layered metal oxides which have been characterized in literature have been synthesized by solid-state methods, though other methods are also sometimes utilized when solid-state methods are insufficient. In the solid-state method, which is most frequently used for alkali battery cathode materials [55, 11, 24], precursors are ground or milled into a powder, frequently pelletized to press the compounds close together, then heated in an appropriate environment (oxidizing, reducing or inert) in order for synthetic reactions to occur.

1.5.2 Characterization of Synthesized Materials

The most important forms of characterization for evaluating battery materials in this thesis are structural characterization, most often and easily done by x-ray diffraction (XRD), and electrochemical characterization, which tests the electrode material against a reference (typically alkali metal) electrode to establish its capacity, average voltage and observe phase transitions. XRD uses coherent x-ray radiation aimed at the sample, which is diffracted through the crystal structures present in the sample giving a spectrum, which can then be analyzed against known spectra to identify the crystal structures and symmetries present.

Electrochemical characterization is done by placing the sample material into a test electrochemical cell, typically with a metal reference electrode. The output gives a voltage during a particular time of charge or discharge. Low rates are typically used as they usually result in maximizing capacity and allow for more clear depiction of
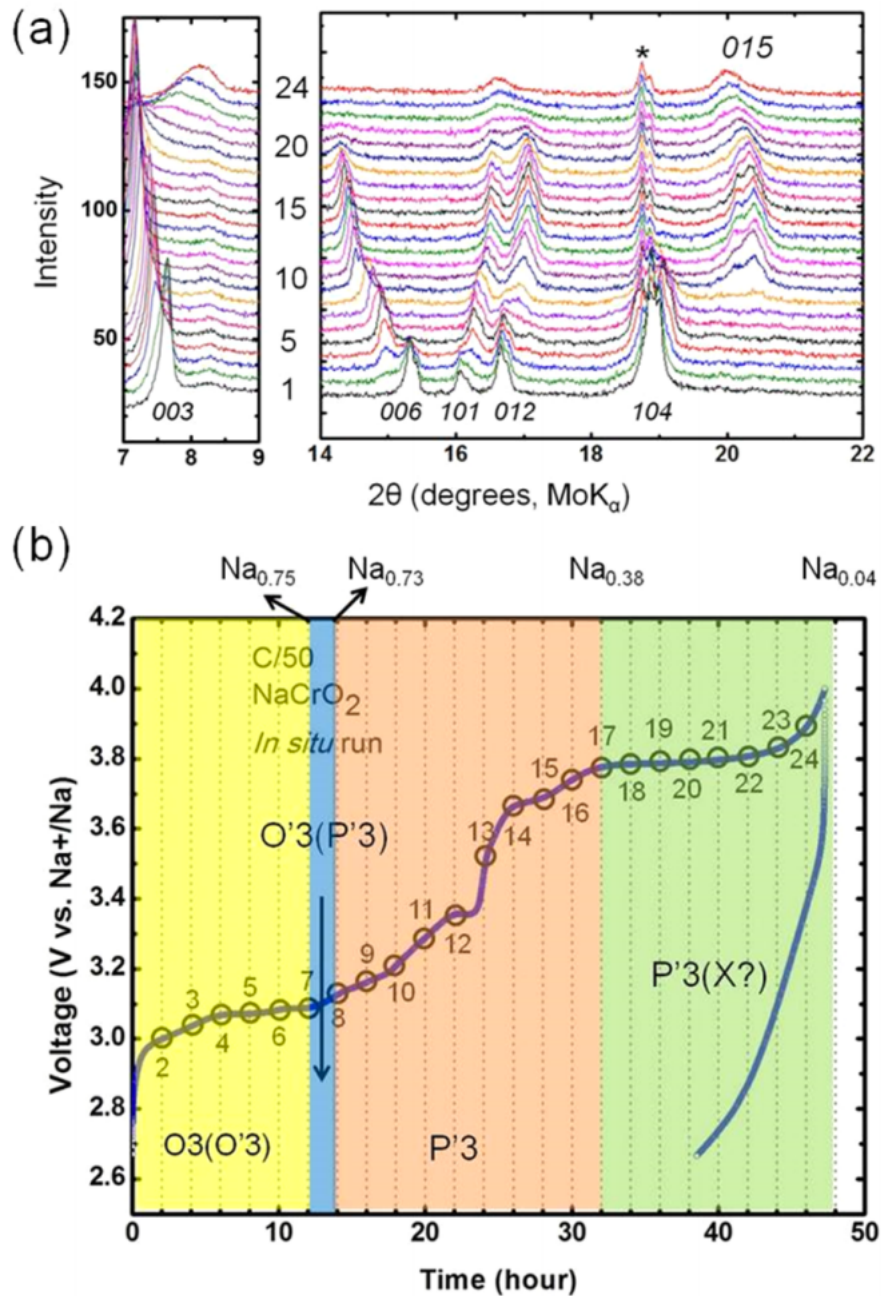
Figure 1-10: (a) Shows 24 $in-situ$ XRD patterns collected during the first charge of O3-type Na_xCrO_2. (b) Shows the corresponding electrochemical cycling data, with scan numbers placed on top of the voltage curve. Color-shaded regions correspond to four reactions associated with stacking variations. Originally published by Bo et al.[8]

41

features such as steps and plateaus on the voltage curve. At low rates, kinetic effects such as polarization are minimized[56]. $In-situ$ XRD characterization combines these methods by periodically analyzing the XRD spectrum of a battery cell while it is charged, thereby allowing the observation of the change in crystal structure and lattice parameters during battery operation. An example of $In-situ$ XRD characterization combined with electrochemical characterization is shown in Fig 1-10. This is an extremely important technique for identifying phase transitions that may hinder electrode function and cause failure. XRD techniques are relatively high level, however, and require other analysis to identify phases with accuracy and precision. In these cases, it is very advantageous to combine computational and experimental efforts, to relate high-level characterization to what is occurring on the atomic scale.

1.6 Thesis Overview

This thesis examines layered electrode materials for sodium ion batteries and investigates the influence of working ion concentration, transition metal selection, and layer stacking on sodium ion cathode material function during electrochemical cycling. Specifically, the work of this thesis delves into the reversible and irreversible phase transformations that occur during electrochemical cycling. The most common phase transformation - that of alkali-ion and vacancy ordering within the alkali layer, is examined first in the topotactic O3-type system.

Chapter 2 looks at topotactic deintercalation of sodium (desodiation) from O3-type versions of all single first row transition metal oxides that reversibly intercalate sodium ions. Theoretical topotactic voltage curves are predicted and specific vacancy ordered structures are examined. Chapter 2 also investigates at the energetic significance of layer stacking in O3 sodium ion layered transition metal oxides, as well as the influence of transition metal oxidation state ordering and mixing. **Chapter 3** extends this analysis to P-type layered TMOs to gain an understanding of the energy differences between O and P-type sodium intercalating layered oxides and the stabilization mechanisms of P-type structures. It proposes necessary design criteria for

P-type layered oxide synthesis and the potential existence of a P2-Na$_x$NiO$_2$ material.

Chapter 4 extends the methods used in the prior chapters to examine the potential intercalation of sodium ions into graphite for use as an anode. This chapter shows that the use of pure graphite as a sodium ion anode is not thermodynamically plausible, even when co-intercalating the sodium with other alkali ions, disputing previously published experimental work. **Chapter 5** concludes the thesis.

Chapter 2

O3-type layered transition metal oxide cathodes for sodium ion batteries

2.1 Sodium ion and vacancy ordering in O3-type layered metal oxide sodium-ion battery cathodes

2.1.1 Introduction

As introduced in Chapter 1, sodium ion batteries have been highlighted in recent years for their potential as an inexpensive, geopolitically neutral alternative to Li-based rechargeable batteries, largely due to the global abundance and low cost of sodium-containing precursor materials[26]. The number of layered transition metal oxide compounds that can intercalate Na ions reversibly is large compared to its Li-ion counterparts, implying a much broader chemical space in which electrode materials can be optimized. This, together with sodium's abundance, balances the disadvantage in energy density due to the standard potential of Na^+, making Na-ion batteries excellent candidates for large-scale energy storage[57, 27]. Theoretical work[3] has pointed out the fundamental difference between Na and Li intercalation that makes

Na cathodes more stable against transformation into other structures. Vast progress has been made in the exploration of potential cathode, anode and electrolyte materials for Na-ion batteries, with publications relating to sodium energy storage materials increasing to hundreds per year in 2013 and beyond.[2]

Na-ion intercalating transition metal oxides were first studied for their potential electrochemical properties in the 1980s, showing reversible Na intercalation for seven layered oxide systems with $3d$ transition metals (TMs): Na_xMO_2 (M = Ti[58], V[59], Cr[60, 61], Mn[62], Fe[63], Co[6], Ni[60]). This is in sharp contrast to their Li-equivalents which only reversibly exchange Li for M = Co and Ni[64, 61, 3]. Several layered Na-TM oxides approach the energy densities of their Li-ion counterparts. In particular, mixed O3 TM oxides can deliver specific energy densities close to 600 Wh/kg (for example, $Na(Mn_{0.25}Fe_{0.25}Co_{0.25}Ni_{0.25})O_2$ delivers 578 Wh/kg)[9], with single TM oxides such as Na_xMnO_2 reaching capacities of nearly 200 mAh/g[38].

Reversible intercalation of Na ions from layered TM oxide hosts results in several reversible first order phase transformations appearing as large steps and plateaus in the electrochemical voltage curve. Such steps are most numerous and apparent in single TM oxide systems, such as O3-type $NaNiO_2$ [65], O3-type $NaMnO_2$[38], O3-$NaVO_2$[10] and P2-$NaVO_2$[66] (here O3 and P2 refer to the Delmas naming convention[67]). These phase transitions have been found to result from sodium vacancy ordering and the gliding of TM oxide layers and are apparent even at the highest cycling rates cited in literature (typically C/10)[38, 11]. While Li-intercalating layered TM oxides are synthesizable only in the O3 structure, Na-ion intercalating layered oxides demonstrate two types of stacking varieties: O3, which can transform reversibly through slab glide to P3[67], and P2 which can transform reversibly to O2[68]. Of particular importance is the study of Na-vacancy ordering common between TM chemistries, and its driving force. Such Na-vacancy ordering occurs through clear first order transitions in single TM compounds, and therefore can be best studied in these systems. Though some work has been done on predicting alkali ion ordering in several Li-ion and Na-ion systems[69, 70, 71, 72, 73], this has only been undertaken for the entire intercalation range in very few cases, and with little

46

comparison between similar systems.

Phase transformations and the shape of the voltage curve can strongly influence the function of a battery cathode material. A voltage curve with many large first order phase transition steps can lead to poor cyclability because these phase transitions act as additional energy barrier in moving the Na-ions from their octahedral sites and can lead to defect formation and propagation during cycling. Steepness of the voltage curve contributes to slower kinetics. For example, slow kinetics have been evidenced in O3-type $NaVO_2$[59], which shows numerous first order phase transitions in the steep, experimental voltage curve. Conversely, a recent study in a P2 type material showed that when ordering phase transitions are suppressed, kinetics and cycle life are excellent[74]. It is thus important to understand these phase transformations to facilitate better material design. The objectives of this study are to explore the low energy vacancy ordering transitions within the O3-type lattice structure and to draw comparisons across the spectrum of different TM systems. We discover, through an extensive computational search of O3-type Na-ion intercalating systems, the vacancy ordering patterns common to all seven TM systems. We further investigate the magnitude of the ordering energies and the effect of layer stacking, examining the effect of interaction between adjacent Na layers on total energy.

2.1.2   Computational Methods

This study is restricted to the O3-type layered structure as classified by Delmas[67] and its monoclinic derivatives formed by the coordinated distortion of the TM oxide octahedra due to Jahn-Teller instabilities[9] and oxidation state ordering[10]. The O3 structure is shown in Fig. 2-1. We investigate the case of topotactic electrochemical deintercalation, where the fundamental O3 structure is not disturbed and there is no ion migration between the TM and Na layers, though the lattice parameters and unit cell internal degrees of freedom are fully relaxed. The majority of calculations are performed on unit cells with a single Na-ion layer repeat period perpendicular to the layers. Except for an established structure at 5/8 Na concentration which has been characterized experimentally and confirmed computationally in previous work
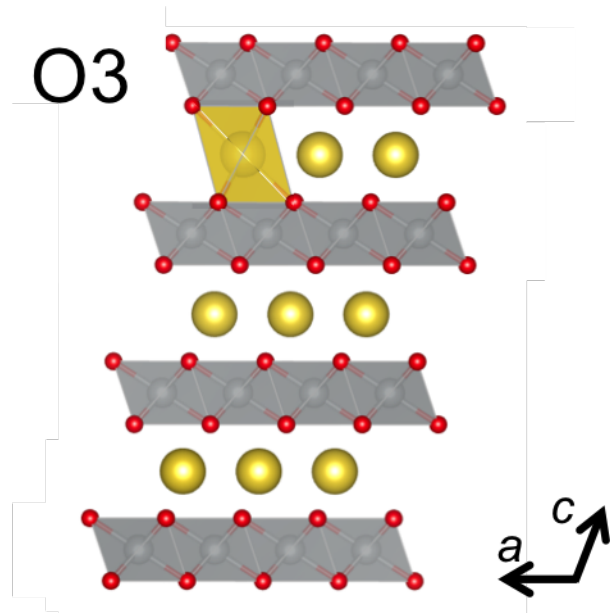
Figure 2-1: O3-type layered metal oxide structure. The sodium ion sits in octahedral sites between layers of metal oxide octahedra, oxygen stacking repeats after three layers.

(Fig. 2-6(j).)[9], Na ions are assumed to remain in octahedral sites and not moved into highly distorted or tetrahedral sites in the Na layer. All initial structures are obtained by replacing the alkali and Co^{3+} ion in the $R\bar{3}m$ $LiCoO_2$ structure, except in the cases of Jahn-Teller active Ni^{3+} and Mn^{3+} ions where the monoclinic distortion is imposed on metal oxide octahedra.

The energies were calculated for a large trial set of possible Na-vacancy ordered structures within the layered metal oxide framework. The trial set consisted of structures that commonly occur as ground state orderings on the triangular lattice, such as those determined by Kaburagi and Kanamori[75] to be ground states with up to 3rd neighbor interactions, as well as the possible ground states for $O3$-$NaCoO_2$ found by Wang, Ding and Ni[70]. In addition, potential structures were generated at Na concentrations of 1/4, 1/3, 1/2, 2/3 and 3/4. At these concentrations ground states have been predicted for Li intercalating layered oxides, such as Li_xNiO_2 [76]. Potential vacancy orderings at these compositions were generated on supercells restricted to a single Na layer, and included repeating patterns up to 12 Na_xMO_2 unit cells in size. Potential structures were generated using an enumeration algorithm developed

by Hart and Forcade and implemented in python as part of the pymatgen[77, 47] codebase. For the selected concentrations, between 10 and 60 unique structures were calculated depending on supercell size, giving a total of approximately 500 calculations for each TM system. The total trial set was then calculated in a high-throughput framework using density functional theory (DFT) to generate convex energy hulls for each of the seven Na_xMO_2 systems, such as that for the M = Cr system shown in Fig. 2-3. From these, any ordering occurring as a ground state in any of the systems was collected, leading to a set of 18 low-energy ordering types.

For each of the 18 orderings appearing as ground states in any of the seven TM systems, we further investigated the effect of interplanar interactions by generating all possible adjacent-layer stacking variants of the ordering along the c-axis. These supercells were generated by laterally translating the Na-vacancy ordering pattern in adjacent layers by all linear combinations of the primitive in-plane lattice vectors for the AMO_2 unit. Symmetrically equivalent stackings were removed from the dataset. An example of this is given in Fig. 2-2, which shows two structures with a projection of three identically ordered Na layers and how these can be positioned relative to one another.

2.2   Results

2.2.1   Single Transition Metal Ground States

For a Na_xMO_2 system the convex hull is given by the linear combination of ground states which gives the lowest energy at any composition. A voltage curve is generated from the energy differences of these ground states along the convex hull.

Fig. 2-3 and Fig. 2-4 show the hull and voltage curve for the O3-Cr system as an example. Red points on the hull plot indicate computed structures which are higher in energy than the ground state phases. Blue points on the hull indicate the ordered ground state structures for the Cr system. The voltage curve in Fig. 2-4 shows steps corresponding to 8 stable phases occurring at 3/4, 2/3, 5/8, 1/2, 2/5, 1/3, 1/4

49
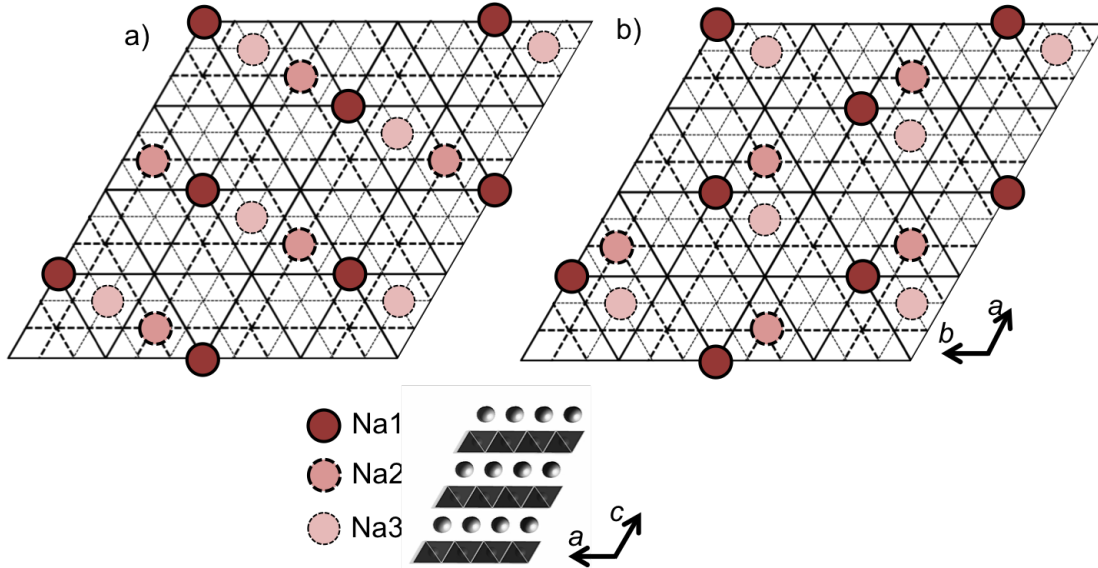
Figure 2-2: Different stacking variants of a $Na_{1/3}MO_2$ ordered layer. Three layers are shown by solid, dashed and dotted lines. Different shades on atoms indicate Na in different layers. a. and b. show the two different types of stacking possible if one Na layer is translated in-plane relative to its adjacent layer.

and $1/7$ Na concentrations. As the voltage curve is the result of 0K calculations, finite temperature entropy effects are expected to smoothen the curves. The figures surrounding the voltage plot depict the Na-vacancy ordering for each ground state in a single Na layer.

Fig. 2-5 shows the calculated O3 voltage curves for all seven Na-intercalating TM oxides. From the computed voltage curves we see that in all seven O3 systems, strong phase transitions are predicted to occur at $1/2$ and $1/3$ Na concentrations, as shown by the large 0.25-0.75 V voltage differences at these steps. The Cr and Mn voltage curves are shallow compared to the other systems, spanning less than 1.5 V (compared to systems such as Ti and V which span between 2 and 3 V). It should be noted our results indicate that topotactic deintercalation to low Na concentrations leads to high energy states, and therefore very high voltages for some systems (e.g. V). It is expected that in these systems non-topotactic structural changes away from O3 may occur.

All single-layer Na-vacancy orderings that appear as a ground state in one or more of the seven systems form the set of 18 structures shown in Fig. 2-6. Several
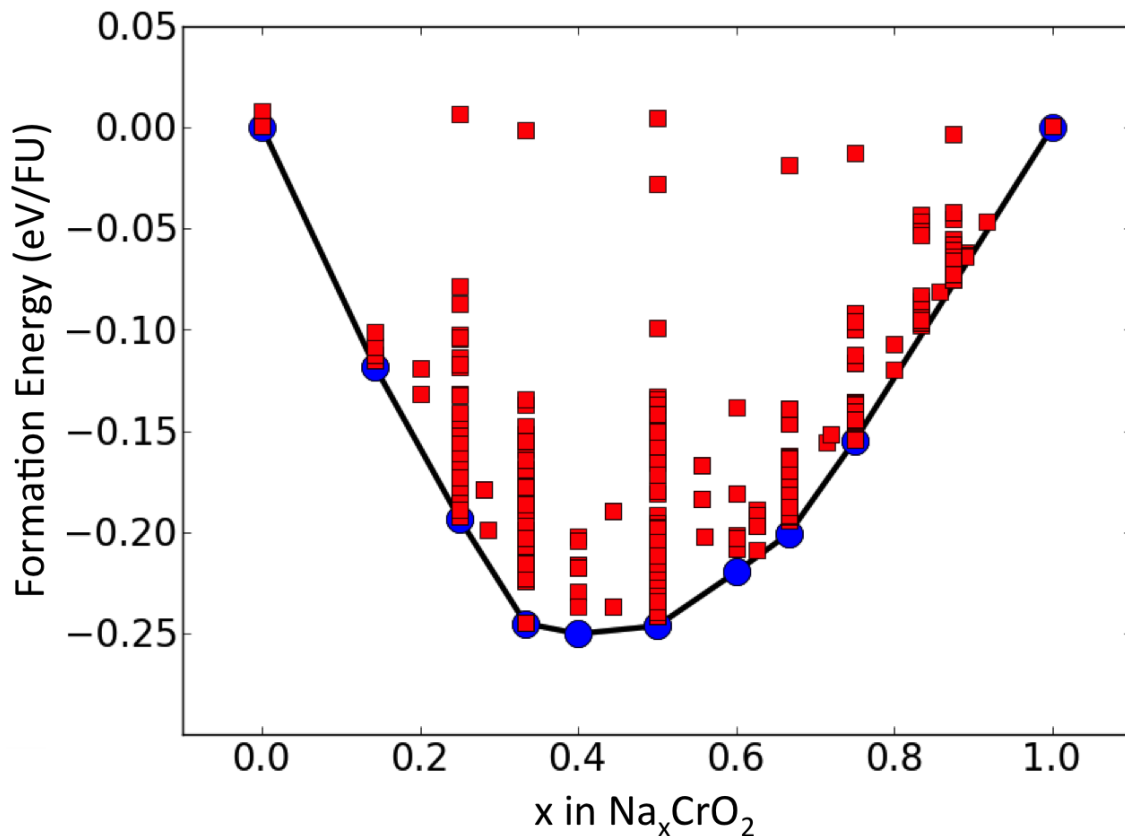
Figure 2-3: Calculated energies for Na-vacancy orderings in the Na_xCrO_2 system. Red points indicate the energies of different enumerated single-Na-layer phases computed at that Na concentration. Blue points are ground states as they are part of the convex energy hull (solid line).
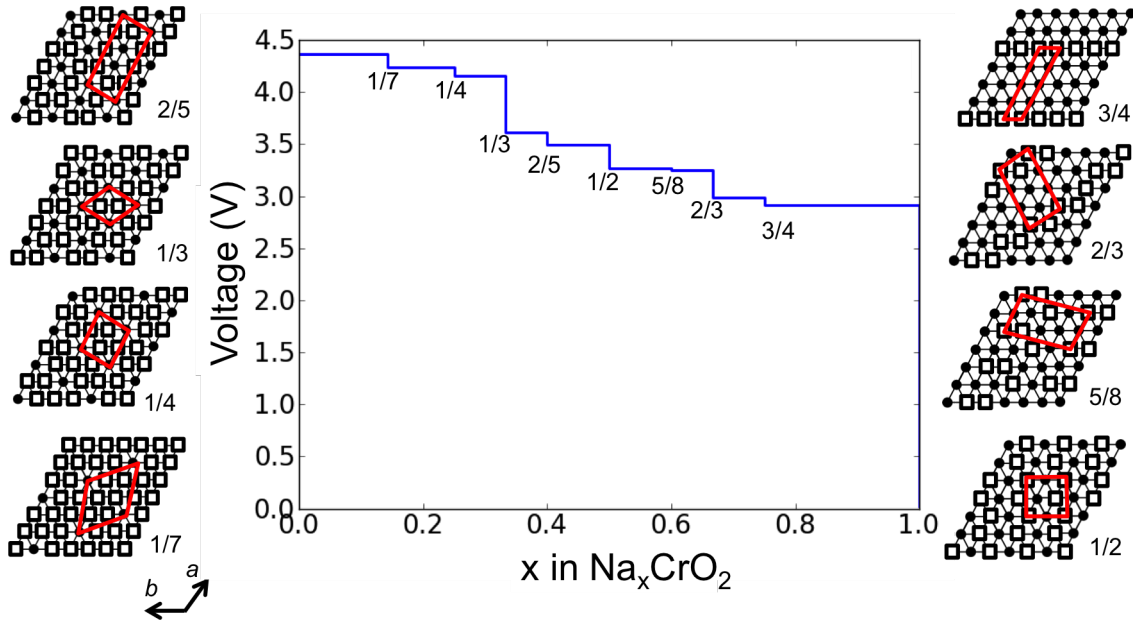
Figure 2-4: Computed O3-lattice voltage curve with predicted ground state Na-vacancy orderings for O3-Na$_x$CrO$_2$

of the ground state orderings have a fairly homogeneous distribution of vacancies and Na (e.g. Fig. 2-6 a, b, c), while others show vacancy clustering in regularly distributed lines (e.g. Fig. 2-6m, n, p). Fig. 2-6(j) shows a unique ground state found experimentally and confirmed computationally in earlier work[9] in which Na ions are relaxed out of their original octahedral sites into distorted octahedra. This structure does not appear as a ground state in TM oxide systems other than the Ni and Mn systems and is related to the strong Jahn-Teller coupling in Na$_x$MnO$_2$.

Some Na-vacancy orderings are present with their symmetrically equivalent structure obtained by exchanging Na ions and vacancies. For example Fig. 2-6(b) and Fig. 2-6(o), and Fig. 2-6(d) and Fig. 2-6(l) represent equivalent orderings. It is remarkable, however, how many of the ground state Na orderings do not occur with their equivalent vacancy pattern. This can only occur if the effective Hamiltonian describing the Na-vacancy interactions is highly asymmetric around x=1/2 due to the presence of strong effective many body interactions[50]. Note that electrostatic interactions, often thought to dominate cation-vacancy ordering, would create a more symmetric system as their ground state solution is symmetric with respect to Na and
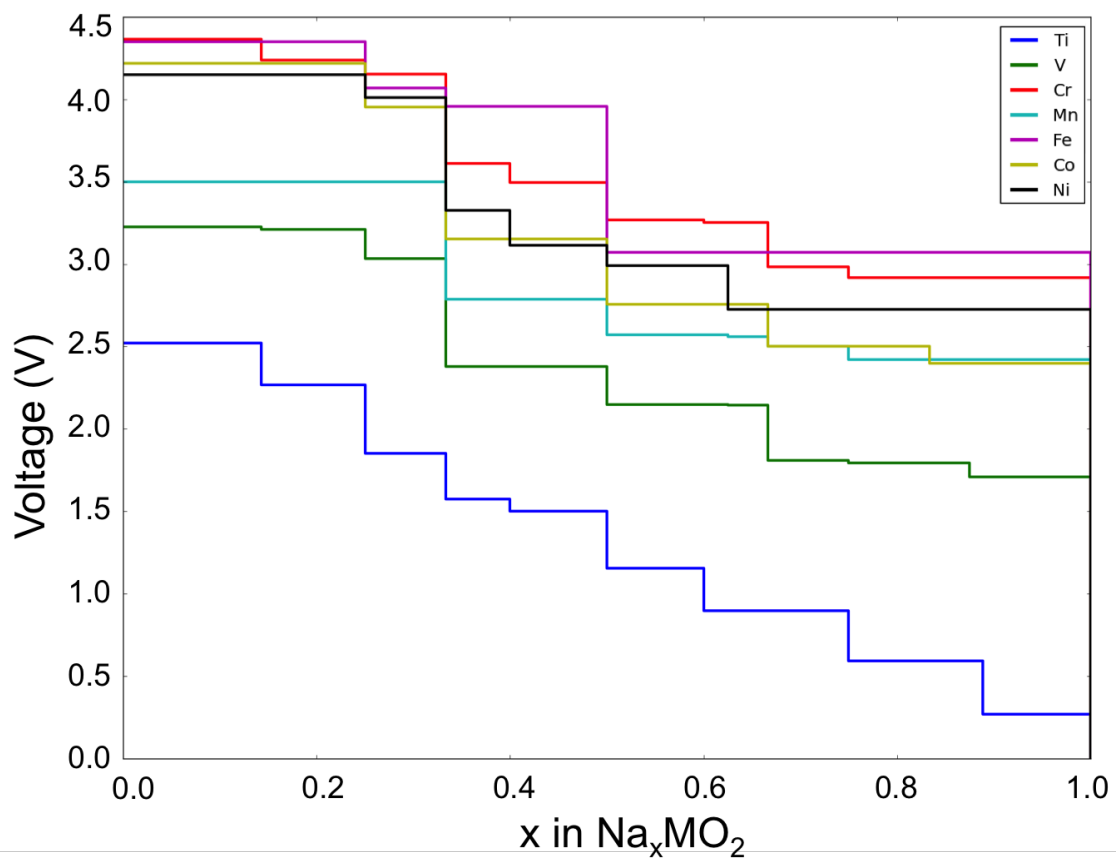
Figure 2-5: Computed voltage curves for Na_xMO_2 (M = Ti, V, Cr, Mn, Fe, Co, Ni). The voltage is referenced against Na metal.
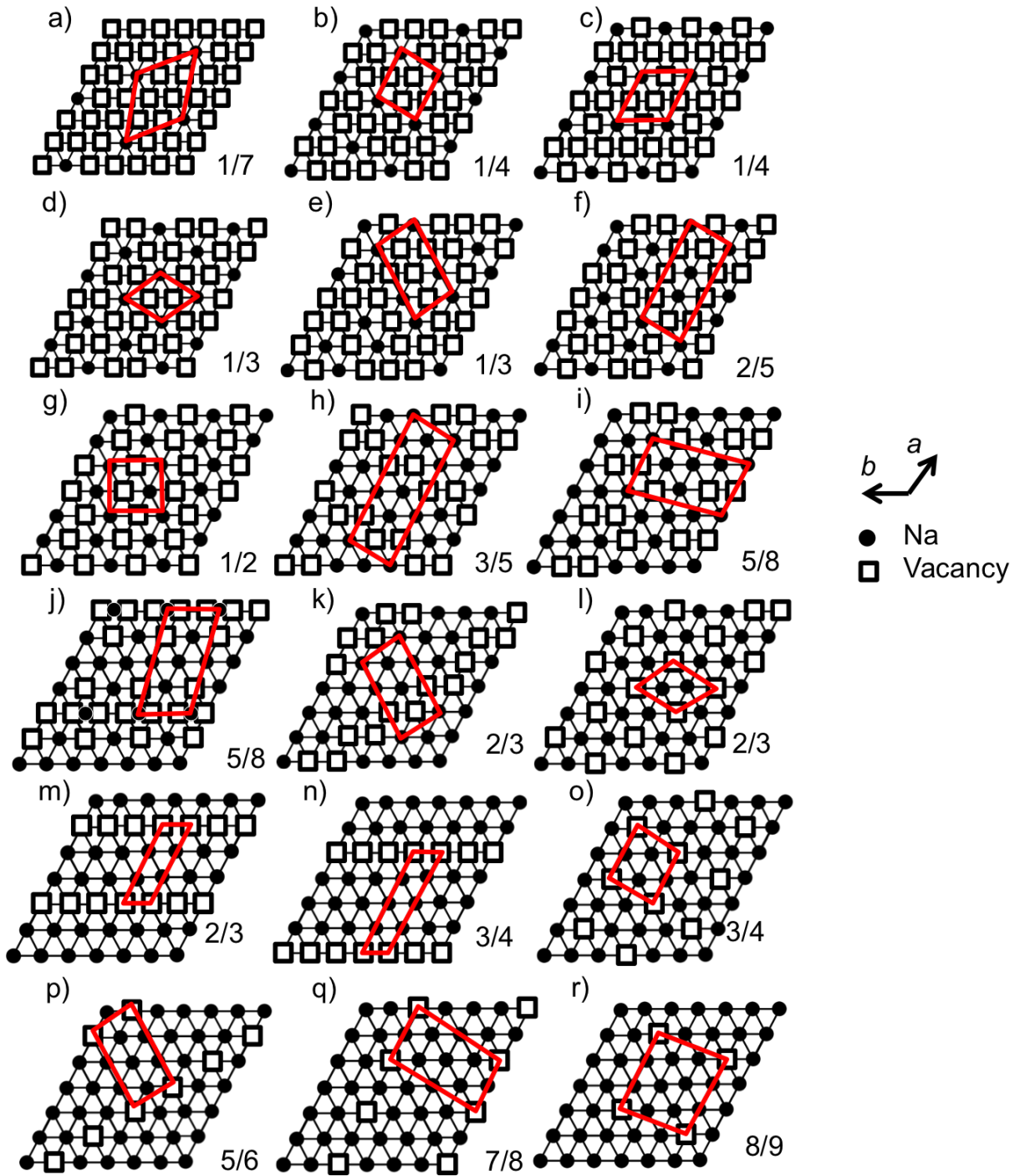
Figure 2-6: a)-r) Na vacancy ordering in single layer phases found as ground state phases in Na_xMO_2 voltage curves (M = Ti, V, Cr, Mn, Fe, Co, Ni). Figure j) depicts a Na ordering described by Li et al.[9] where Na ions are relaxed out of their conventional octahedral sites.

x_{Na}	1/7	1/4		1/3		2/5	1/2	3/5	5/8	5/8	2/3			3/4		5/6	7/8	8/9
TM	a	b	c	d	e	f	g	h	i	j	k	l	m	n	o	p	q	r
Ti																		
V																		
Cr																		
Mn																		
Fe																		
Co																		
Ni																		

- ■ GS
- ■ <10meV above hull
- ■ 10-20 meV above hull
- □ >20 meV above hull
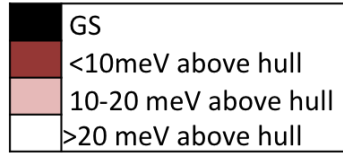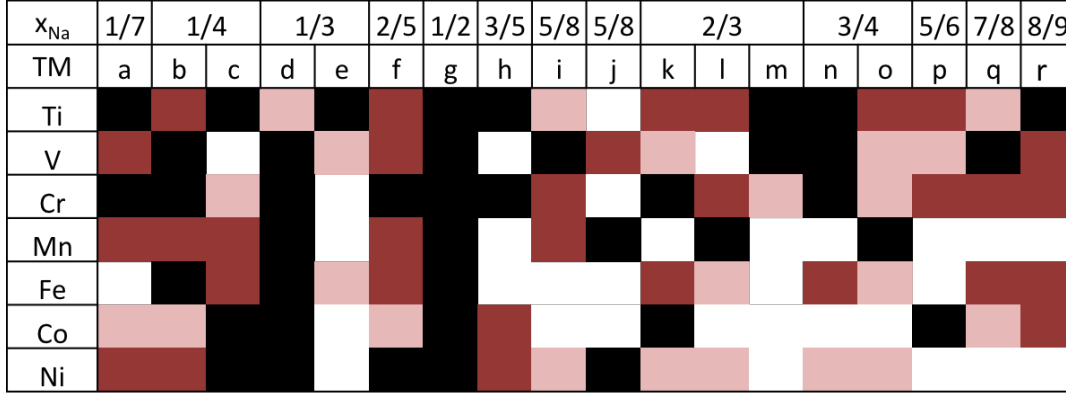
Figure 2-7: Energy above hull for Na_xMO_2 versions of each Na-vacancy ordering type (a-r) shown in Fig. 2-6. The lightest spaces indicate that the structure has been calculated for the transition metal system in question, but does not appear within 20 meV of the hull for that system.

vacancies[78]. Hence, the strong asymmetry in the possible ground states in Fig. 2-6 indicates effective many body interactions play an important role. Such many body interactions can be caused by elastic effects or strong coupling between Na-vacancy ordering and the local electronic structure.

We explored how close to the convex hull each of the candidate orderings in Fig. 2-6 is for each Na_xMO_2 system. These results are summarized in Fig. 2-7. The darkest squares indicate that the ordering type as defined in Fig. 2-6 is a ground state in the particular O3 TM oxide system. Lighter squares in the figure indicate that a structure is not a ground state but is within 0 to 10, and 10 to 20 meV/per Na_xMO_2 formula unit of the convex hull respectively. The lightest color indicates the structure was calculated but was more than 20 meV away from the hull. It is clear from the data in Fig. 2-7 that similar orderings appear as ground state phases for multiple TM oxide systems. The structure shown in Fig. 2-6(g) for $x_{Na} = 1/2$ appears as a stable state in all seven TM systems. For $x_{Na} = 1/3$, all seven TM systems have a ground state phase, and six of these have the same Na ordering, the electrostatically favorable $\sqrt{3}$

x $\sqrt{3}$ ordering (Fig. 2-6(d))[79]. While the remaining Ti system has another ground state for $x_{Na} = 1/3$ the energy of the $\sqrt{3}$ x $\sqrt{3}$ structure is within 20 meV of the hull.

The Ti and Cr systems have a stable ground state at each composition in Fig. 2-7, and many of the non-ground state orderings are close to the convex hull. This indicates a strong degeneracy of ordering energies, which can be caused by either small interactions or long-range frustrated interactions. Some of the competing structures are within 5meV/FU of the ground state implying that entropy effects at finite temperatures or minor compositional variations (as for example those caused by different synthesis techniques), may lead to a different phase. A degeneracy in phases together with a shallow voltage curve and small voltage steps is likely to lead to faster kinetics while cycling through phase transitions and thus would imply better rate capability in the cathode. The concentration differences between phase transitions correlate to the ease of nucleation of the new phase, and the height of each phase transition step corresponds to the energy difference between phases. Thus the Cr and Ti voltage curves indicate better possible kinetics because they have multiple shallow steps. In the Fe system, ground state structures are comparatively more stable than competing ordered structures which are typically 10-20 meV higher in energy, implying that the phases forming in the Fe system are non-degenerate and have higher energetic boundaries (and thus slower kinetics) in cycling. Results similar to Fe can be seen in the Co and Ni systems.

While our results indicate that the total number of distinct ground state Na-vacancy orderings that can be stable is remarkably small, there is significant variation of the ground state set among different TM systems. This implies that the TM selection influences the preferred Na-vacancy ordering, either structurally or electronically. Due to the relatively small energy range within which different orderings appear above the hull for each TM system, we investigate to what extent the adjacent Na layer interaction (position of Na ordering relative to that of an adjacent layer, or layer "stacking") can influence the energy of the system and determine the preferred ground state. Such long-range interlayer interactions are known to be related in part to the electronic structure configuration of the TM ion[9, 76].

2.2.2 Influence of stacking on energy in O3 type layered oxides

To investigate the interlayer interaction we enumerated all distinct lateral translations of the Na pattern in adjacent layers (no rotation of ordering) generated by all linear combinations of primitive vector directions parallel to the Na layer. This leads to between 2 and 6 different possible configurations for each pattern. Fig. 2-8 shows the difference in energy between the highest and lowest energy stacking for each Na concentration, transition metal and ordering type. High total bars (as for orderings "j" and "o" for example) imply that in general the 3D stacking of that ordering strongly influences energy regardless of TM, while for orderings such as "m" and "l" stacking has little effect on the energy. The size of each color-coded bar indicates the difference for that TM. For example, stacking clearly has more influence on energy in Na_xCoO_2 (orange bars) than Na_xCrO_2 (green bars).We find that the effect of layer stacking on energy within a single ordering type is small compared to the effect of Na-vacancy ordering, however it is non-negligible. The energy difference between highest and lowest energy stacking depends on the Na concentration and transition metal in the system, but is generally less than 30 meV per formula unit. The system with ordering type "j" is relatively strongly affected by stacking because the Na-ions in this ordering exist in highly distorted sites due to a correlated effect across layers, so changing their layer stacking increases the energy significantly. It is expected that orderings that have only a small energy change when the stacking changes will have frequent stacking faults and as such may be more difficult to detect in diffraction.

Desodiation of $NaMO_2$ creates 3+/4+ mixed valence on the transition metal. For many TM oxides mixed valence is accommodated by the distribution of discrete M^{3+} and M^{4+} ions. Hence, Na-vacancy ordering can be accompanied by charge ordering on the TM sites. For systems such as P2-Na_xCoO_2[80] and Li_xFePO_4 [81] such coupling has been well documented. We performed a preliminary analysis of this coupling in the V system. Fig. 2-9 shows the Na-vacancy ordering and the oxidation state ordering in the TM oxide layer in two stacking variants of a ground state of the V system. Fig. 2-9(c) shows the TM ion oxidation state ordering in each TM oxide
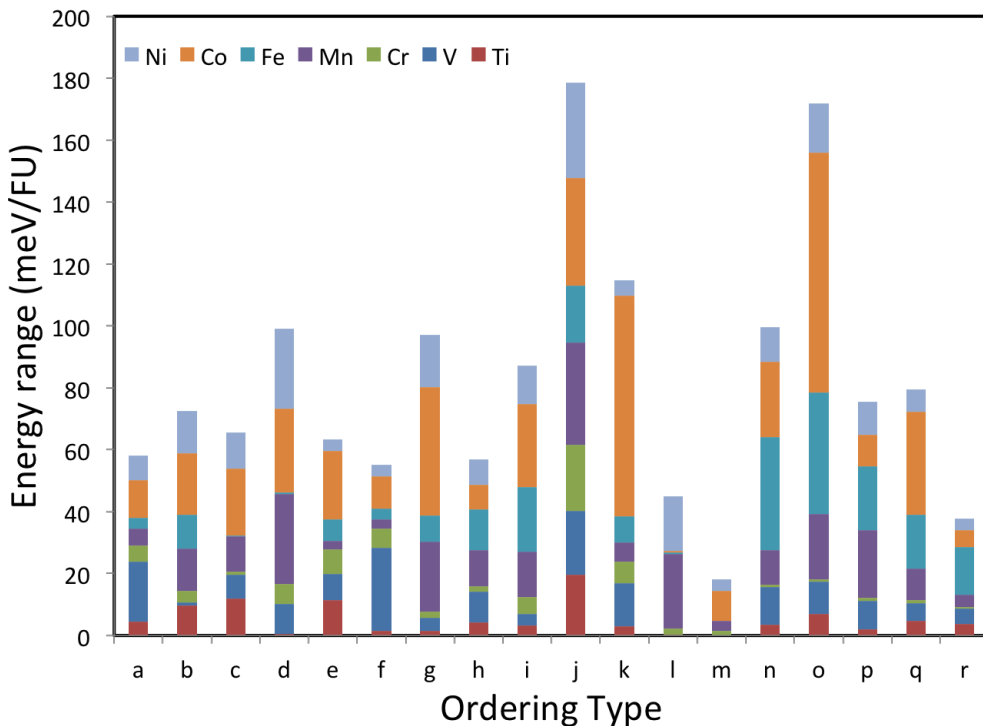
Figure 2-8: Energy difference between highest and lowest energy stacking of the 18 low energy orderings in seven TM systems. The letters refer to the structures as shown in Fig. 2-6. The size of each color-coded bar gives the energy difference between the highest and lowest energy stacking for that TM and ordering type. Hence, high total bars as for orderings "j" and "o" indicate that in general the 3D stacking of that ordering strongly influences the energy, while for orderings such as "m" and "l" there is very little effect of stacking on the energy.

layer. The Na-vacancy ordering in this structure is that of Fig. 2-6(d), with 1/3 Na concentration patterned in a $\sqrt{3}$ x $\sqrt{3}$ ordering, which allows for two possible stockings of adjacent Na layers. The red octahedra represent V^{3+} and blue octahedra represent V^{4+}. Fig. 2-9(a) shows the stacking with an energy 10 meV higher than that of Fig. 2-9(b). Though the TM oxidation state ordering is the same in each of the TM oxide layers, their relative position to the Na layers and to each other changes with stacking.
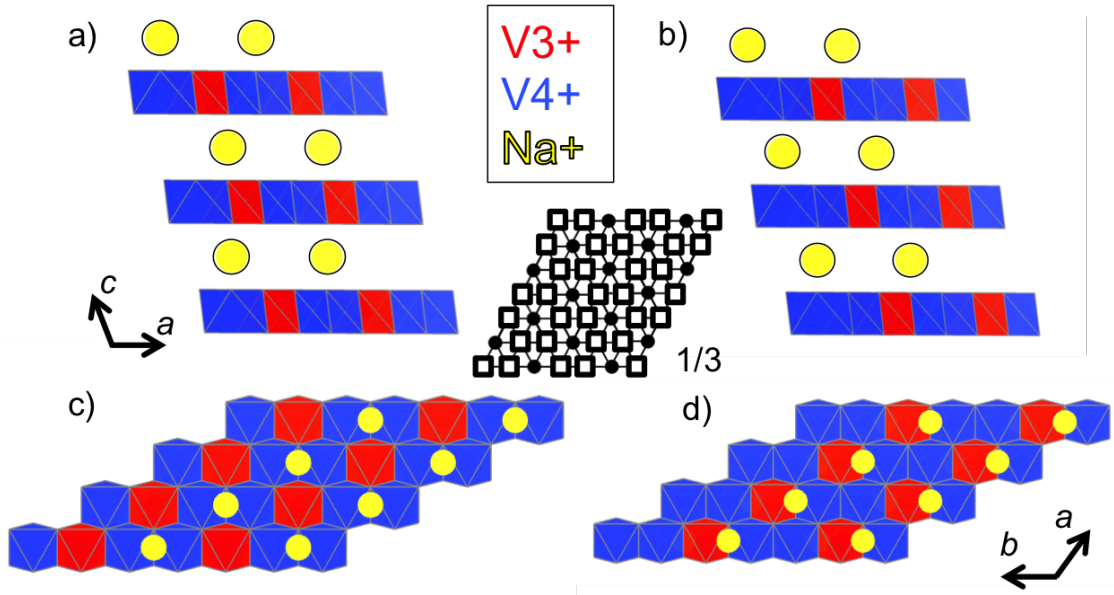
Figure 2-9: Comparison of oxidation state ordering between two stacking variations of the $x_{Na} = 1/3$ ordering shown in Fig. 2-6(d), in the O3 host. Red octahedra indicate V^{3+} ions while blue octahedra indicate V^{4+} ions. The difference in stacking of adjacent layers can be seen as a glide of the middle Na layer while the top and bottom layers remain stationary.

2.2.3 Discussion of vacancy ordering in O3-layered sodium ion metal oxides

Comparison to Experiments

The objective of our study is to investigate the common Na-vacancy orderings that can occur in Na_xMO_2 systems. By extensively calculating seven O3 Na_xMO_2 systems, 18 unique single layer ordering types are found, many of which occur repeatedly in several TM systems. Though few Na-vacancy ordered phases have been fully characterized in O3-type Na-ion intercalation systems, the experimental results available are in good agreement with our observations. Direct comparison with experiments is possible for systems where transition into a P3 host does not occur during cycling, such as Na_xVO_2[10] and Na_xTiO_2[82].

The voltage plots in this study are computed at 0 K, and while temperature can have an effect on whether weakly ordered phases are observed, previous work has shown that 0K phases are good indicators of the phases present at room temperature.
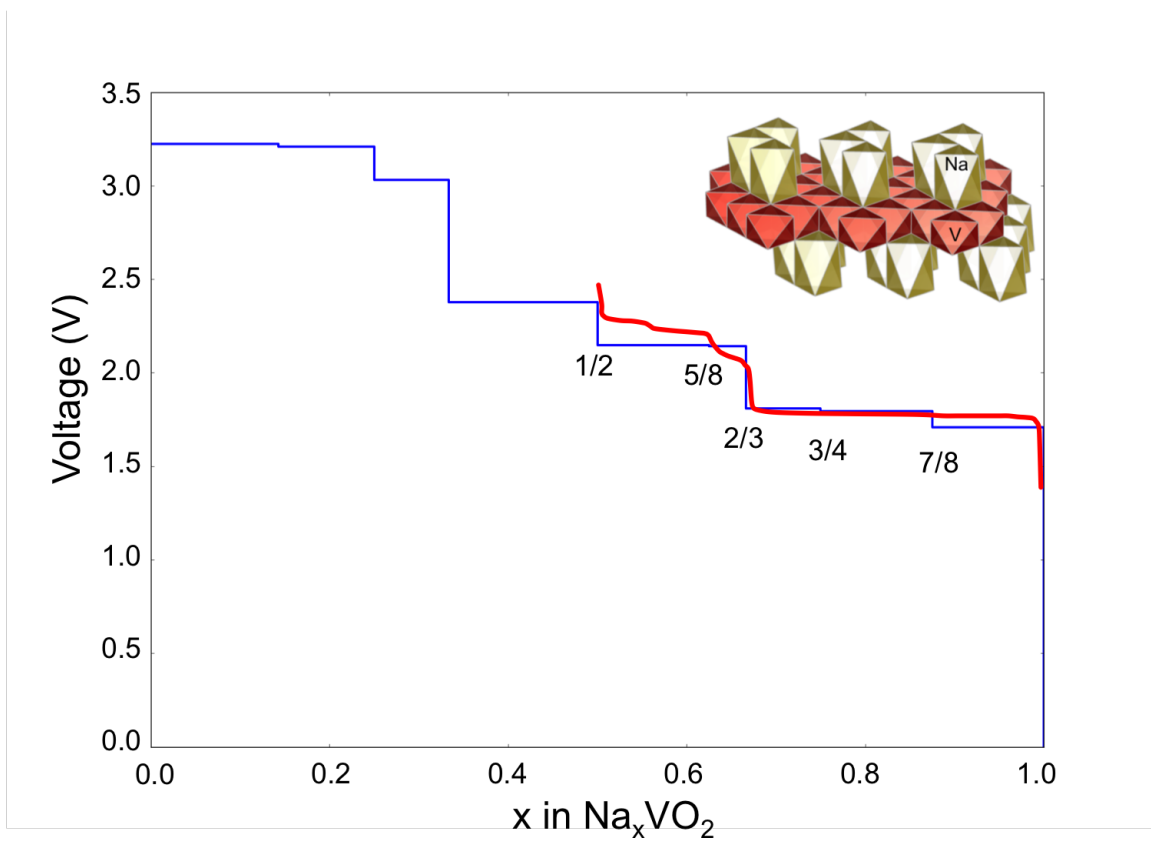
Figure 2-10: Computed and experimental voltage curve of O3-Na_xVO_2. Inset: predicted ground state for O3-$Na_{1/2}VO_2$ also observed experimentally[10].

In $LiCoO_2$ and $LiNiO^2$ for example, where finite temperature phase diagrams have been computed and derived experimentally, low temperature ground state phases are apparent to well above 300K[76, 73]. Due to its relative ionic radius, Na-ion ordering is predicted to be stronger than that of Li ions, leading to even higher disordering temperatures, making experimental validation of this study viable. Indeed, ordering is observed experimentally in Na-intercalating layered oxides, which show numerous voltage steps and plateaus indicating ordering phase transitions even at relatively high cycling rates of C/20 or C/10[83, 38, 65, 84].The degeneracy of phases as uncovered in this study can be an indicator of relative disordering temperatures, with highly degenerate systems tending to lower disordering temperatures.

Fig. 2-10 shows a comparison of the calculated voltage curve with the experimentally measured voltage for Na_xVO_2 which cycles in an O3-type phase between $NaVO_2$ and $Na_{1/2}VO_2$. Agreement between the measured and calculated voltage curve is quite good in terms of Na concentration and voltage matching at phase transitions (steps and plateaus), with the experimental curve falling within 0.1 V of the computed curve at most points. Phase transition positions match at 2/3, 5/8, and 1/2 Na concentrations, and in particular the phase transition at $x_{Na} = 2/3$ matches the computed curve well, with a step height of approximately 0.4 V compared to the computed 0.5 V. The computationally predicted ground states at 3/4 and 7/8 are not apparent in the experimental curve, however it is possible that these are smoothed away at finite temperature due to entropic effects. Additionally, the ground state vacancy ordering of $Na_{1/2}VO_2$ predicted by this study as described by Fig. 2-6(d) matches that characterized by Didier in 2012. The predicted ground state layer stacking is also correct[10]. The comparison captures some limitations to our methods, however, as the experimental curve shows an additional first order phase transition between x_{Na} = 0.5 and x_{Na} = 0.6 which is missing from the computed results.

In several systems (M = Cr, Co, Ni), the fully sodiated phase exists in the O3 structural configuration but the P3 phase appears after approximately 0.2-0.4 Na is de-intercalated from the stoichiometric $NaMO_2$ phase. In these systems, direct comparison with O3-phase calculated voltage plots is only possible in parts of the

experimental curves where the O3 system is more stable. In several single TM layered oxide systems an irreversible phase transformation[12] is apparent when the cathode is charged beyond a particular capacity (typically x_{Na} =0.3-0.5 in Na_xMO_2). This irreversibility is thought to come from transition metal ion migration into the alkali layer, as has been evidenced in the Fe, Cr and Ti systems[85, 86, 58]. Therefore for low Na concentrations, direct comparison with experimental results is not possible, but our calculations suggest likely topotactic ground states at lower Na concentrations.

Common Ground State Phases in O3 Single TM Oxides

Our results give rise to several interesting implications that can be used to predict alkali orderings in layered metal oxide structures. We look closely at the Cr system and results from several other TM oxide systems as examples. We see effects on ground state phase vacancy homogeneity, degeneracy of phases as well as the influence of the Jahn-Teller effect in our analysis.

Electrostatic interaction is clearly an important influence on ground state ordering. As electrostatics is a repulsive interaction one would expect it to drive the minority species (Na for x < 1/2 or vacancies for x > 1/2) as far away from each other as possible leading to a "homogeneous" structure. This is evidenced in our candidate set of orderings, where such "homogeneously distributed" Na-ion patterns are seen as ground states for multiple TM oxide systems, e.g. Fig. 2-6(a),(b) and (c). In several of the systems studied, however, the ground state phases have minority species which are clustered in lines or rows, indicating that pure Na-Na or vacancy-vacancy electrostatic repulsion is not the only contribution to the energy. For example the Cr system described in Fig. 2-4 shows vacancies clustered in rows within the alkali layer at x_{Na} = 3/4 and 2/3. Such "less homogeneous" ordering requires some attractive interactions between like-species. Attractive interactions are caused by either direct hybridization, unlikely for Na ions, or by elastic interactions mediated through the solid[87]. The presence of these interactions and their associated orderings is consistent with the strain associated by inserting or removing the large Na^+ ion.

The Cr system shows many structures very close in energy and near the hull,

implying a number of energetically degenerate phases at each Na-concentration. A highly degenerate phase is more likely to disorder at lower temperatures as only small fluctuations in energy are needed for the system to move between ordered phases. The Cr system can access these phases easily, as indicated by a voltage curve with low slope and voltage steps that are relatively small for $1/2 \leq x_{Na} \leq 1$. The Fe system shows a different trend than Cr: we see non-degenerate Na-vacancy orderings, implying stronger ordered phases. Indeed in Na_xFeO_2, the x=1/2 ground state is so dominant that it creates a two-phase region for $1/2 \leq x_{Na} \leq 1$. One component to the difference between the Cr and Fe system is their electronic structure. Cr^{3+} and Cr^{4+} ions are present in the partially sodiated phases, neither of which have e_g electrons, while high spin Fe^{3+} and Fe^{4+} have two and one unpaired e_g electrons respectively. It has been demonstrated that e_g electrons couple to alkali ordering more strongly than t_{2g} states[76], and hence Fe ions have stronger influence on Na-vacancy ordering.

Ni^{3+} and Mn^{3+} ions are strongly Jahn-Teller active, meaning their TM-O bonds are distorted in the octahedral complex. Therefore the Ni and Mn systems typically exhibit similar Na-vacancy orderings which are different from the other non-Jahn-Teller active TM systems. This is seen in Fig. 2-7 wherein Ni and Mn systems exhibit the same ground state Na ordering at $x_{Na} = 1/3$, 1/2, and 3/4. The Mn and Ni systems also both exhibit an unusual ground state at 5/8 Na concentration (Fig. 2-6(j)), where the Na ions are distorted from their regular octahedral sites. This has been confirmed experimentally for the Mn system[9]. This distortion has not been investigated for other Na concentrations.

Comparison to Li Systems

Only a small number of layered $LiMO_2$ systems have been investigated for Li-vacancy ordering as only the Co and Ni systems show reversible intercalation among the single transition metal $LiMO_2$ systems. The O3-Li_xCoO_2 system has been studied both experimentally and computationally[72, 73, 88, 89]. Computational studies of the phase diagram revealed that the O3 host structure is stable above $x_{Li} = 0.3$, below which the H1-3 host is stable with an ordered structure at $x_{Li} = 1/6$. Computationally,

ordered ground states in the O3 host were found at x_{Li} =1/3, 2/5, 1/2, 3/5, 2/3, 3/4, 5/6, 6/7 and 8/9[72, 73]. The phases at x_{Li} =2/3 and x_{Li} =1/3 exhibit the $\sqrt{3}x\sqrt{3}$ patterns in Fig. 2-6(l) and Fig. 2-6(d) respectively (this ordering is also predicted to be present in alternating O3 layers in the H1-3 structure at x_{Li} =1/6), and the phase at x_{Li} =3/4 has c(2x4) vacancy ordering as in Fig. 2-6(o). The $Li_{1/2}CoO_2$ ordering was confirmed experimentally[88, 89] and is a 2x1 ordering where the alkali ions form rows on the triangular lattice[72, 88, 89]. This ordering was investigated for our study and found to be within 20 meV/FU of the hull for all Na systems. Fig. 2-6(g) ordering in this study was conversely found to be a near-degenerate state in Li_xCoO_2, just 1 meV/FU away from the convex energy hull[73].

The Li_xNiO_2 voltage curve has been shown computationally and experimentally to exhibit ordering phases at room temperature at x_{Li} =1/4, 1/3, 2/5, 1/2 and 3/4[69]. The voltage curve differs significantly from that of Li_xCoO_2 as the presence of Jahn-Teller active Ni^{3+} ions in this structure results in inter-plane interactions between Li ions. Several of the orderings found to be ground states in this system are found in the set of 18 described here. $Li_{1/3}NiO_2$ and $Li_{1/4}NiO_2$ [90] have been characterized experimentally and shown to be the same as the Fig. 2-6(d) and Fig. 2-6(c) patterns predicted in this study. The orderings predicted computationally by Arroyo y de Dompablo in the Li_xNiO_2 system but not described experimentally also match those in the set of 18, for x_{Li} =2/5(Fig. 2-6(f)) and 3/4 (Fig. 2-6(o))[69]. These findings indicate that the set of 18 orderings described in this work can also function as potential candidates for non-Na alkali ordered structures.

2.2.4   Conclusions of Vacancy Ordering Study

Through thorough DFT computation we have predicted voltage curves and stable Na-vacancy orderings for seven Na_xMO_2 O3 compounds. We have found 18 orderings that appear as ground states in on for more of the seven TM systems. Several appear as ground states in more than one system.

While some Na-vacancy orderings are the electrostatically favored pattern, the lack of symmetry of the ground states around $x_{Na} = 1/2$ and the presence of ground states

with inhomogeneous Na-vacancy distributions points to other contributions such as ionic relaxation and electronic structure contributions to the effective Na-vacancy interactions. We believe that these 18 ground state structures form a good set of candidate structures to refine the Na-vacancy ordering in more complex Na_xMO_2 systems.

2.3 Transition metal mixing in layered metal oxides

2.3.1 Transition Metal Mixing for O3 Sodium Ion Layered Oxide Cathodes

For cost reduction purposes and functional design, state of the art transition metal oxide cathode materials are typically synthesized with mixes of several transition metals[91, 11]. TM choice affects the voltage curve, rate capability and capacity of an electrode material, thus TM selection is important for optimizing battery function. For example, manganese retains the O3 structure throughout cycling and adds stability to the layered material, although its lower voltage can be countered with the addition of iron or cobalt. Transition metal mixing can also lead to smoothing of the voltage curve, thereby improving battery cyclability by decreasing the number of first order phase transitions in each cycle.

Practically, layered oxides can only be cycled to 0.3-0.5 sodium content before irreversible phase transformations are evident and there is significant capacity loss. Thus, it is important to understand which transition metals are oxidized first and what oxidation states they take on when mixed. In this section, DFT computations are used to identify what oxidation states the transition metals are in throughout the electrochemical cycling of $O3\text{-}NaFe_{1/3}Co_{1/3}Ni_{1/3}O_2$. The results can be applied to other mixed TM structures.

2.3.2 Computational and Experimental Methods

Transition metal ordering was enumerated for a small (three TM ion) supercell and calculations were performed with different initialization states for transition metals. A comparison of GGA, HSE and GGA+U functionals was performed to establish the most appropriate method for this system (GGA+U). Charge integration was performed on the CHGCAR output file as part of the pymatgen python package[92]. Charge was integrated spatially from the center of each transition metal ion and plotted with respect to radius. The plateaus at ionic radii around 1.5 Angstrom indicated the converged spin of each ion, thereby indicating the charge of the chosen transition metal ion.

Partial densities of states for transition metal ions generated from the VASP output were used to establish the oxidation states at several stages of sodium intercalation (0, 1/3, 2/3, and fully sodiated). Both charge integration and PDOS plots were used to determine the state of oxidation for the transition metal ions at each stage of sodiation. A sample set of plots is shown in Figure 2-11 for fully sodiated $Na_3FeCoNiO_6$ initialized with magnetic moments for Fe4+, Ni2+ and Co3+.

Experimental synthesis and characterization for this study were performed by Dr. Plousia Vassilaras. $NaFe_{1/3}Co_{1/3}Ni_{1/3}O_2$ was synthesized by solid-state reaction. Excess amounts of Na_2O, NiO, Co_3O_4 and Fe_2O_3 were mixed and ball milled for 4 h at 500 rpm rate, and the resulting material was collected in the glove box. About 0.5 g of powder was fired at 800 řC under O_2 for14 h before it was quenched to room temperature and moved to a glove box filled with argon. X-ray diffraction (XRD) patterns were collected on a PANalytical X'Pert Pro equipped with Cu Ka radiation in the 2θ range of 5?85ř. All the samples were sealed with Kapton film to avoid air exposure. Profile matching of the powder diffraction data of the as-prepared $NaFe_{1/3}Co_{1/3}Ni_{1/3}O_2$ was performed with Highscore Plus using space group $R\bar{3}m$.

Cells were configured with Na/1 M NaPF6 in EC:DEC = 1:1/$Na_xNi_{1/3}Fe_{1/3}Co_{1/3}O_2$, Super P carbon black (Timcal, 15 wt.%) as conductive agent, and polyethylenetetrafluoride (PTFE) (DuPont, 5 wt.%) as binder. The 1 M NaPF6 in EC:DEC
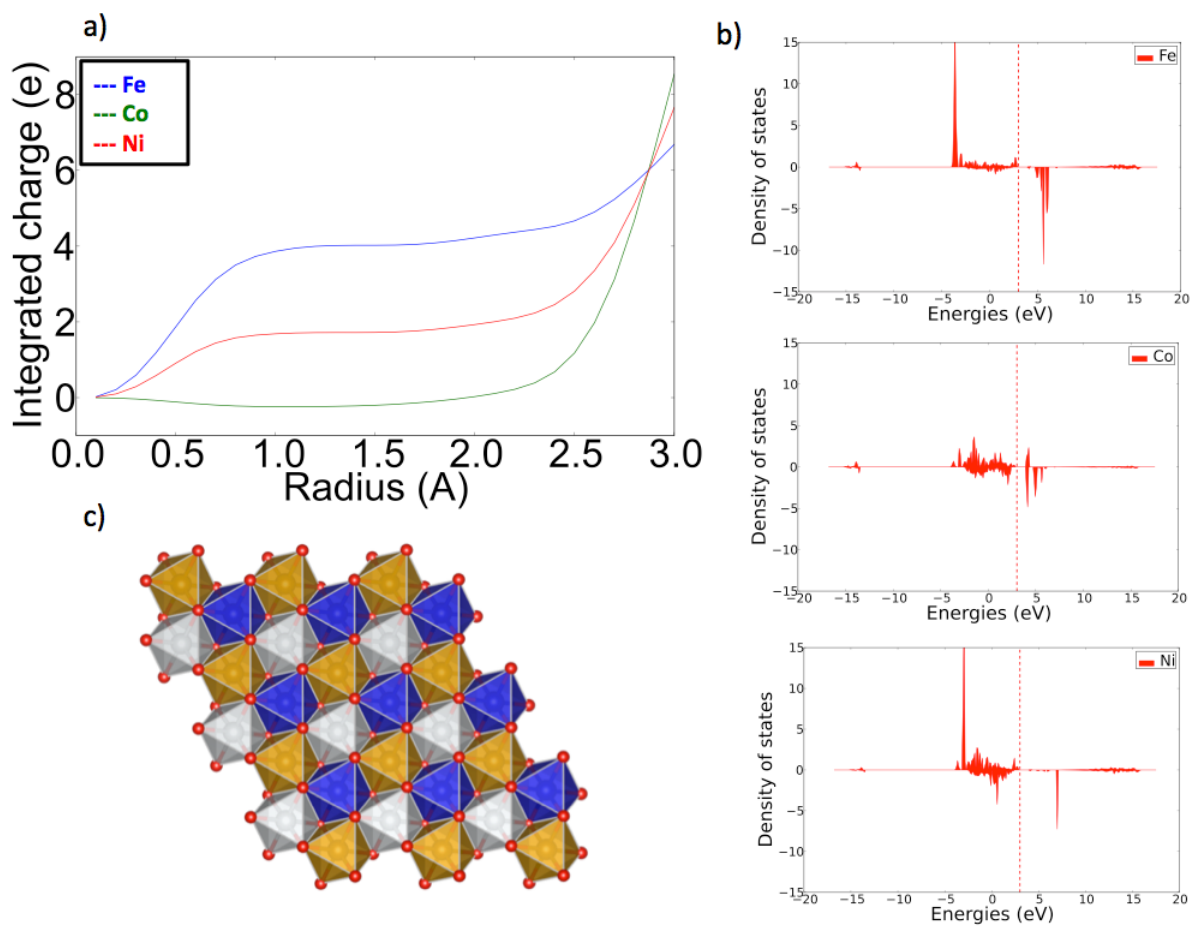
Figure 2-11: (a) Charge integration plot for fully sodiated $NaFe_{1/3}Co_{1/3}Ni_{1/3}O_2$ initialized at Ni2+, Fe4+ and Co3+. (b) Partial density of states plots generated from first principles (c) Schematic showing the "honeycomb" transition metal ionic ordering in the TMO layer.

electrolyte was prepared by dissolving anhydrous NaPF6 (98%, Sigma Aldrich) into EC:DEC (anhydrous, 1:1 in volume ratio). Two pieces of glass fiber served as separators and stainless steel as current collectors in Swagelok cells, assembled in an argon-filled glove box with the moisture level and oxygen level less than 0.1 ppm. The loading density of the active material used was in the range of 2.2?3.1 mg/cm2. The cells were cycled at room temperature using a Solatron 1287 operating in galvanostatic mode and potentiostatic mode.

2.3.3 Computational and Experimental Results and Discussion

As can be seen in Figure 2-12, there is significant sloping and fewer features in the mixed transition metal system during electrochemical cycling than in single TM oxide systems showed earlier in this chapter. Transition metal mixing leads to a much smoother, sloped voltage curve due to the break in coupling between the sodium ions and vacancies in the active ion layer and the transition metal ions in the metal oxide layer. As sodium is removed, transition metal ions are oxidized in a particular preferential order of TM (described below) which prevents the oxidized ions from coupling to the strong, electrostatic interaction of the sodium ions, thereby weakening this interaction instead of strengthening it.

First principles calculations were performed at compositions x = 1, 2/3, 1/3 and 0 for $Na_xNi_{1/3}Fe_{1/3}Co_{1/3}O_2$ in order to estimate the average voltages between these compositions and to determine the order of transition metal oxidation. Results indicate that in the fully sodiated material Ni is close to a + 2 oxidation state and the Co and Fe states are mixed in a state that is partially oxidized to + 3.5. Upon de-sodiation, the Fe/Co system is first oxidized to Fe4 + and Co4 + at 2.72 V followed by Ni2 + oxidation to 3 + and 4 +. The horizontal lines in Fig 2-12 represent the calculated average voltage in each composition domain[48]. While the resulting average voltages are in good agreement with the experimental averages, experimental validation is needed to confirm the unusual oxidation states determined. It is valuable
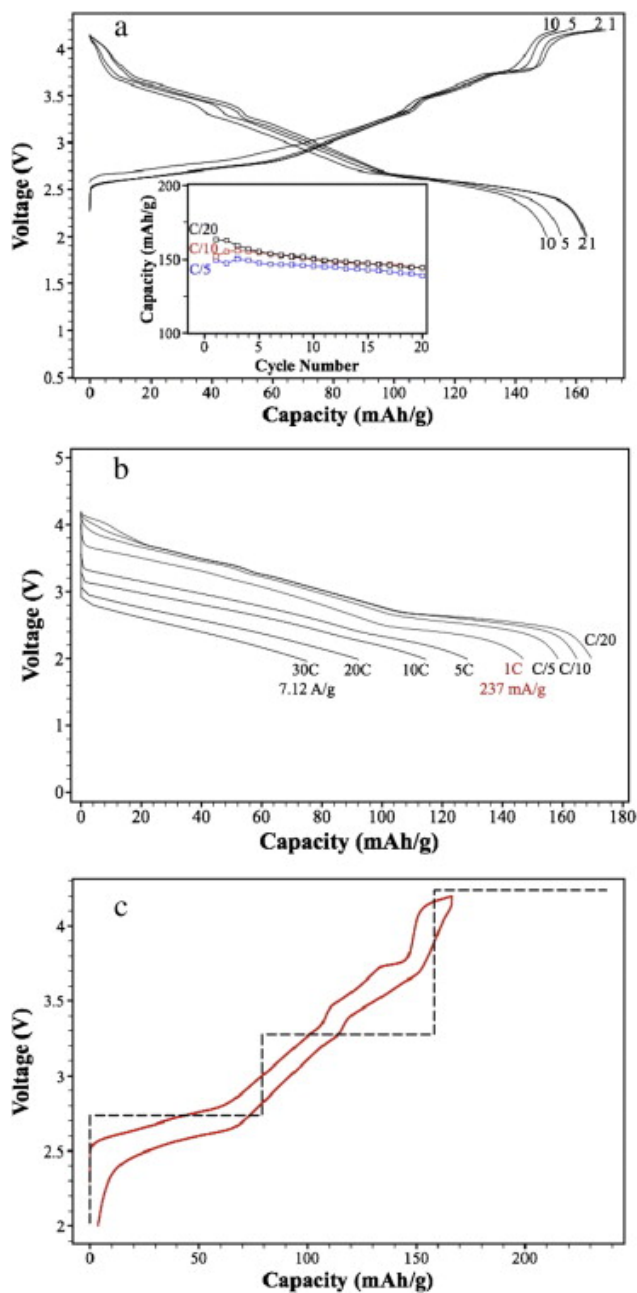
Figure 2-12: (a) Voltage profile of $Na_xNi_{1/3}Fe_{1/3}Co_{1/3}O_2$ for multiple cycles at C/20 and cyclic performance at C/20, C/10 and C/5 as an inset. The cells are galvanostatically cycled between 2.0 and 4.2 V. (b) Rate-capability of NaNi1/3Co1/3Fe1/3O2 in Na cells. The cells were charged to 4.2 V at a rate of C/20 and then discharged at different rates; C/20 (11.86 mA/g) and 30C (7116 mA/g). The sample loading of the active material was 2.18 mg/cm2. (c) Comparison between the experimental second voltage profile (red) and calculated composition-averaged voltages (black) of $NaNi_{1/3}Co_{1/3}Fe_{1/3}O_2$. Originally published by Vassilaras, Toumar and Ceder[11].

to note that nickel is oxidized only after iron and cobalt reach their highest plausible oxidation states for the structure.

2.3.4   Conclusions of Transition Metal Mixing Study

Several important conclusions can be gleaned from this study. The first, chiefly observed experimentally, is that transition metal mixing allows for a much smoother voltage curve than those of single transition metal layered systems. This agrees with the observation made in the previous section of this chapter, that transition metal oxidation state ordering is strongly coupled to sodium ordering, so mixed transition metal systems are likely to have fewer ordering phase transitions. Thus we see fewer first order phase transition features on the electrochemical cycling curve than for the Ni or Co systems, for example. This effect of feature loss can be seen in numerous mixed transition metal oxides when compared to their "component" single transition metal oxides' electrochemical cycling data[65, 93]. The second is in regard to the redox order of the transition metals upon sodium de-intercalation, which shows that oxidation is not necessarily ordered by transition metal (we see Fe and Co oxidized together) and that Ni oxidation is strongly unfavorable and occurs only when Fe and Co have both attained 4+ oxidation states.

2.4   Transition metal migration in layered transition metal oxides

In practice, O3-type layered transition metal oxide cathodes cannot be cycled reversibly between x = 0 and x = 1 sodium content. They suffer from capacity loss at high voltages, when sodium extraction exceeds certain capacity limits. Though slab glide phase transitions, described in Chapter 1, are themselves reversible, they can act as precursors for irreversible phase transitions in layered transition metal oxides. This phenomenon can be seen in O3-type Na_xCrO_2 (Fig 2-13), which undergoes slab glide between x = 0.75 and x = 0.73 and retains a P3-type structure until x = 0.4,

beyond which it transforms back into an O3 phase. At lower sodium content, this system undergoes an irreversible phase transition to a rock-salt structure, likely aided by disproportionation of Cr4+ ions to Cr3+ and Cr6+ ions, the latter preferring a tetrahedral environment[8].

Thoughtful material and cell design must be used to mitigate the capacity loss associated with irreversible phase transitions such as these. The choice of host lattice (P3, O3 or P2) contributes to the ease with which an irreversible phase transition may occur, and the differences between these lattice stacking types is explored in the following chapter.
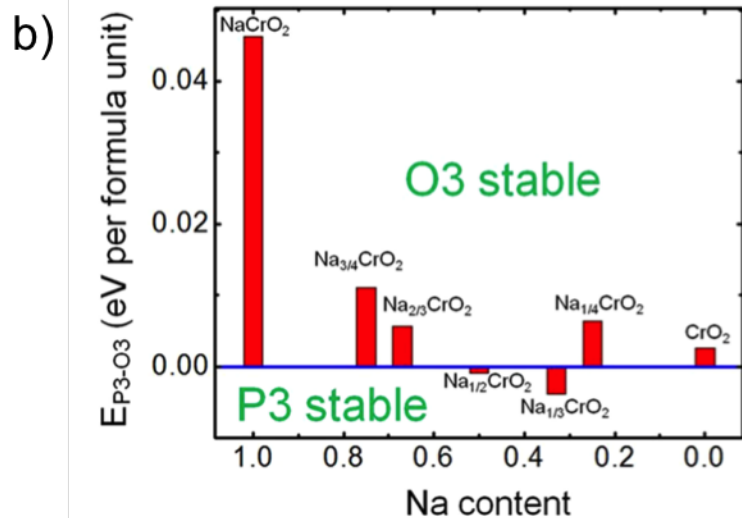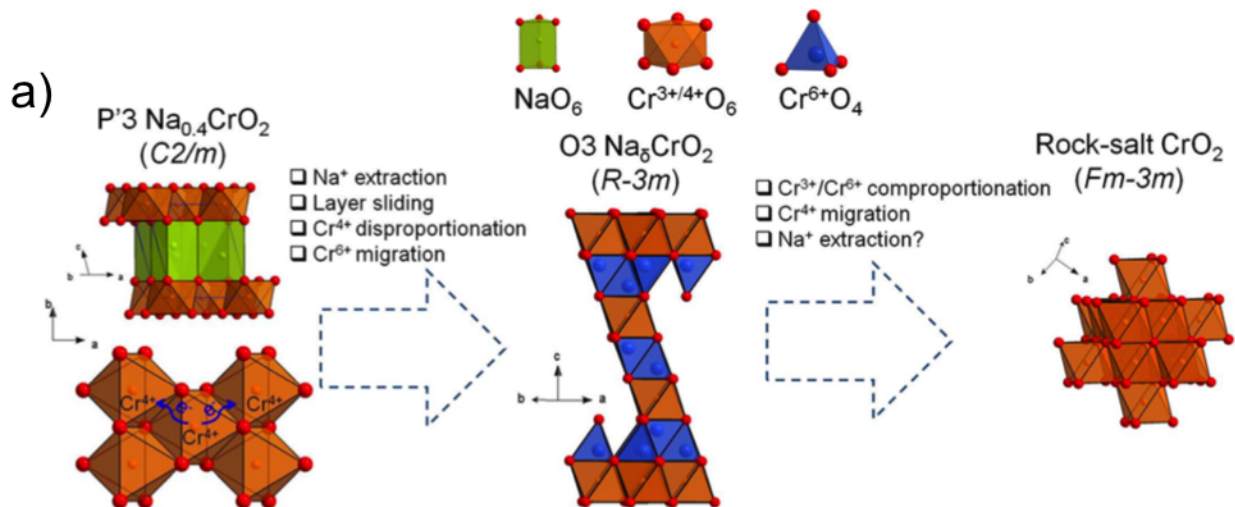
Figure 2-13: (a) Schematic proposal of the P'3-Na$_{0.4}$CrO$_2$ to rock-salt CrO$_2$ structural transition through the O3 intermediate structure. (b) First principles computed energy comparison of structures at different sodium concentrations. P3 is shown to be stable relative to O3 between 0.3 and 0.6 sodium content, beyond which O3 becomes more stable again as more sodium is extracted. Adapted from work originally published by Bo, Li, Toumar and Ceder[8].

Chapter 3

Stability and Synthesis of P2 and P3 Layered Oxides

3.1 Motivation and Prior Work

In the previous chapter, we investigated layered transition metal oxides in the O3 stacking configuration. Sodium ion oxides form layered structures with various stacking types distinct from O3. Each stacking type can be distinguished by the sodium environment and repetition of the oxygen layer stacking. These different stackings are not typically seen in lithium intercalating layered oxides. For sodium systems, the sodium ion can sit in either a prismatic or an octahedral site, and this distinction extends to layered oxides of larger alkali ions (for example, K)[36]. Within the sodium ion battery literature, layered oxides typically crystallize either in the O3, P3 or P2 type structures (Fig. 3-1), according to the nomenclature established by Delmas, who first characterized these different stacking types in the 1980s [67]. P-type compounds have double the number of available sodium ion sites as O-type compounds because the prisms can be closely packed together, however this does not practically change the amount of sodium that can be inserted into the alkali layers, because two neighboring prismatic alkali sites cannot be occupied simultaneously as they are too close together. P3 compounds are related to O3 compounds by a simple translation in the a-b plane (sodium layer plane) of consecutive metal oxide layers relative to each

other. This "glide" can be achieved without breaking metal oxygen bonds, and so this reversible phase transition is often seen upon desodiation from an O3 compound[94]. In contrast, P2 has a different oxygen stacking than P3 that cannot be related back to O3 by a simple translation, and therefore P2 materials require to be synthesized as such. This is illustrated in Figure 1-7 in the first chapter.

In recent studies, P2 has been established as a better electrode candidate material than O3, because its larger interlayer spacing and close-packed prismatic sites allow for faster sodium ion diffusion due to lower diffusion barriers[95, 7]. This means the electrode material has good rate capability and can be charged and discharged more quickly than a chemically comparable O3 material. Mixed-transition-metal P2 oxides can also retain the P-type structure for the majority of the cycling capacity, whereas a phase transition between O3 and P3 type structure is observed even at relatively low potentials in mixed O3 oxides[7, 96, 94]. Retention of stacking is important as repetitive, reversible phase transformations such as slab glide negatively affect rate capability and capacity retention in these materials.

In literature, layered sodium ion P3 and P2 metal oxides are typically synthesized at higher temperatures than O3, at 700 - 800 and 800 - 1300 degrees Celsius for P3 and P2 respectively [85, 97, 98, 99, 100, 101, 102, 103, 104, 105, 106]. Though some are synthesized chemically with heat treatment[59], P3 compounds are most often formed through slab glide during electrochemical desodiation from O3 compounds. A summary of mixed and single transition metal oxides synthesized as P2 is presented in Table 3.1, with their electrochemical capacities if known, with O3 and P3 counterparts mentioned if relevant. This list does not capture all existing P2 compounds, but provides an exemplary guide for transition metal stoichiometries and dopants currently utilized in P2 synthesis. The only single transition metal oxides synthesized as P2 with sodium thus far are Na_xVO_2, Na_xMnO_2 and Na_xCoO_2. The synthesis of P-type compounds is typically achieved at non-stoichiometric sodium ion concentrations (typically around 0.6-0.7) and thus requires a mixed valence on the metal oxide lattice (typically 3+/4+ oxidation states for first row transition metals, to balance the charge of the missing +1 sodium ions). The transition metal ions must remain

stable in their octahedral environment throughout electrochemical cycling, otherwise capacity fading is likely to occur. For transition metals such as iron, for example, Fe4+ prefers a tetrahedral to an octahedral environment, so Fe4+ ions are likely to move out of their octahedral positions in partially desodiated Na_xMO_2 compounds, especially at higher temperatures where they are more likely to have the energy to escape transition metal octahedral sites. In recent years, the sodium concentration window over which the P2 phase is stable has been extended by transition metal selection and mixing, and by the use of inactive transition metals (such as Mg, Zn, and Li) on the metal oxide lattice[103, 102, 101, 107, 108].

There has been some recent work to understand the physical stabilizing mechanisms that make P2 or P3 structures preferentially stable over O3 or over non-layered structures for given transition metals at given synthesis temperatures, and more generally why P type structures are sometimes observed instead of O type structures in sodium ion systems. A recent work from Katcho et al. suggests that electrostatic interaction between oxygen layers is stabilized in P2 over O3 at certain sodium concentrations due to the larger interlayer spacing in P2s[109], however this is an oversimplification because it ignores the influence of transition metal selection on stacking preference, and does not account for the fact that prismatic sites align oxygens in adjacent layers in a way that is electrostatically less stable than the staggered oxygen alignment of O-type structure. Radin et al. recently studied the formation of P3 from O3 via layer glide after desodiation and found that P3 compounds were preferred at intermediate compositions (x $\approx$ 0.5) because sodium-sodium repulsion was minimized in these structures.[36] However, little light has been shone on the relationship between O and P stacking formations and transition metal selection, which is clearly a factor in P-type compound stabilization.

It is of great interest to understand what stabilizes P2, P3 and O3 materials and what makes them synthesizable at given synthesis conditions, both for the optimization of synthesis techniques and for better-guided material design. It is of further interest to understand why some transition metal oxide systems readily form P2 or P3 compounds while others do not.

Table 3.1: Examples of P2 compounds synthesized to date

Compound	Synth. Na	Capacity (mAh/g)	Synth. Temp. (C)
$Na_x[Fe_{1/2}Mn_{1/2}]O_2$	2/3	190	900 (700 for stoichiometric)[85]
$Na_{2/3}Co_xNi_{(1/3-x)}Mn_{2/3}O_2$ (0 < x < 1/3)	2/3	–	900 (700 for P3)[97]
$Na_{2/3}Ni_{1/3}Mn_{2/3-x}Ti_xO_2$ (0 < x < 2/3)	2/3	127 (x = 1/6)	900 - 950 (Ti)[99]
$Na_{2/3}Fe_{1/3}Mn_{2/3}O_2$	2/3	193 (153 sustained)	900[98]
$Na_{0.6}MnO_2$	0.6	140	800[100]
$Na_{2/3}[Mg_{0.28}Mn_{0.72}]O_2$	2/3	220	900 (12 h)[2]
$Na_{0.66}Ni_{0.33-x}Zn_xMn_{0.67}O_2$ (x=0, 0.07, 0.14)	2/3	132	900(15h in air)[82]
$Na_xMg_{0.11}Mn_{0.89}O_2$	–	125	900 (6 h)[103]
$Na_{0.67}Fe_{0.2}Mn_{0.65}Ni_{0.15}O_2$	2/3	350 Wh/kg	900 (6 h)[104]
$Na_x[Ni_{1/3}Mn_{2/3}]O_2$	2/3	150 (125 sustained)	900 (14 h)[105]
$Na_2M_2TeO_6$, (M=Co, Ni, Zn)	2/3	–	900 (24 h)[106]
$Na_xNi_{0.22}Co_{0.11}Mn_{0.66}O_2$	–	–	700-750: P3, 800-900: P2[110]
Na_xCoO_2	0.74	–	850 (24 h)[6]
$Na_{5/6}[Li_{1/4}Mn_{3/4}]O_2$	5/6	200	700 (10 h, air cooled)[2]
$Na_{0.7}Fe_{0.4}Mn_{0.4}Co_{0.2}O_2$	0.7	–	900 (15h, cooled 1C/min)[111]
$Na_{0.74}Ni_{0.58}Sb_{0.42}O_2$	0.74	–	1250 (1 h, quenched)[37]
$Na_{2/3}Mn_{0.8}Fe_{0.1}Ti_{0.1}O_2$	2/3	144	1000 (6h, furnace cooled)[112]
$Na_{0.6}[Cr_{0.6}Ti_{0.4}]O_2$	0.6	–	1000 (15 h)[74]
$Na_{2/3}Co_{2/3}Mn_{1/3}O_2$	2/3	–	950 (12 h)[113]
Na_xVO_2	0.71	–	850 (solid state, 24h under Ar)[114]

3.2 Relative stability of O3, P3 and P2 oxides

3.2.1 Introduction

O3, P2 and P3 layered oxides are characterized by their sodium sites and oxygen layer stacking, as depicted in Figure 3-1. In O3 layered oxides, the sodium ion sits in an octahedral site which is edge-sharing with metal oxide octahedra on both sides of the sodium ion layer. In P3 layered oxides, the metal oxide layers are translated by 1/3 of their a and b lattice parameters (as shown in Figure 1-7). In P3, all sodium ion sites are face-sharing and edge-sharing on one side of the prism, while in P2, there are two types of sites, half of which are edge-sharing and half face-sharing with metal-oxide octahedra.

Once we know a layered structure can be formed at partial sodium concentration, it is of interest to investigate what accounts for the preferential synthesis of the P-type configuration compared to the more commonly seen O-type, and how this is related to transition metal selection. This relatively stability is investigated in the following section by comparing energy hulls and structural parameters of O3, P2 and P3 layered oxides with respect to transition metal and sodium ion concentration. Their relative stability at finite temperatures is also considered using cluster expansion and Monte

76
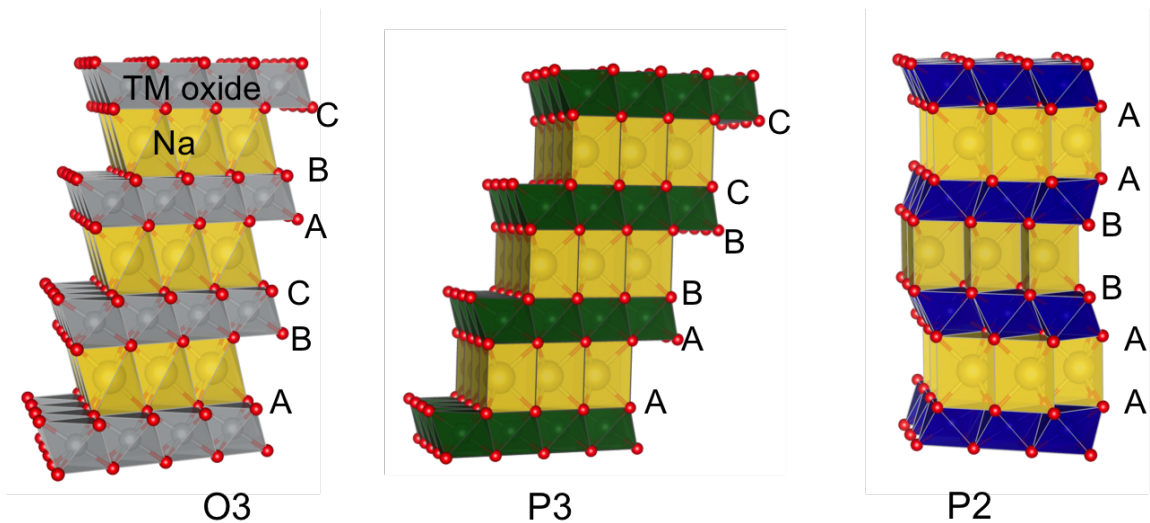
Figure 3-1: Stacking variation for O3, P3 and P2 layered TM oxides. Letters indicate oxygen layer stacking. In O3 and P3, these repeat after three metal oxide layers, while in P2 they repeat after two.

Carlo methods.

3.2.2 Computational Methods

Energy hulls for O3, P2 and P3 lattice types were generated using the method described in Chapter 2 for O3 hulls. For each of the P-type systems for each TM, between 100 and 500 sodium ion vacancy configurations were generated at $1/4$, $1/3$, $1/2$, $2/3$ and $3/4$ sodium concentrations, as well as additional configurations at sodium ion concentrations based on experimentally derived voltage curves.

The cluster expansion method, as described in Chapter 1, was used for P2, P3 and O3 versions of the Cr system, to evaluate their behavior at finite temperatures. The energy Hamiltonian was expanded in terms of site occupancy of sodium ions on the sodium lattice of each structural type. The cluster expansion took into account the additional complexity of charge ordering on the Cr oxide lattice, assigning the 3+ or 4+ relaxed Cr ionic charge based on the relaxed magnetic moment of each Cr ion. The fitting algorithm used an L1 regularized least squares fit with the regularization parameter chosen to minimize the out of sample root-mean-square (RMS) error. The dielectric constant was fit simultaneously with the effective cluster interactions

(ECIs).

The cluster expansions each used datasets of approximately 100-400 distinct configurational energies, as computed with GGA+U. They included double and triplet interactions up to 6 and 4 Ångstrom in radius respectively, and used the electrostatic energies determined by Ewald summation for each configuration to enhance the accuracy of the fit. The cluster expansion fitting algorithm was developed in the Ceder group by Dr William Richards. For the O3 system, 96 unique structures were used to fit the cluster expansion, resulting in 29 non-zero effective cluster interaction coefficients (ECIs) and a best root mean square error (RMSE) of 11 meV per formula unit or approximately 3 meV per atom. For the P3 system, 542 structures were used resulting in 73 non-zero ECIs, with a RMSE of approximately 2.5 meV per atom. For the P2 system, 131 unique structures were utilized in the fit, resulting in 42 non-zero ECIs and a RMSE of approximately 2 meV per atom.

Monte Carlo simulations were used to calculate energy and heat capacity change with temperature in order to estimate the configurational entropy in the Na_xCrO_2. For each system, 16 million sampling steps were used to calculate a temperature sweep between 20 and 4000K, assuming quasi-equilibrium. The Monte Carlo simulations were performed on P2, P3 and O3 ground state structures at 1/2 and 2/3 sodium ion concentrations. For each sodium ion concentration, progressively larger supercells were used to ensure entropy convergence at very high temperature. For Na_xMO_2 with x = 0.5, supercells of 112, 896 and 3024 atoms were used. A Savitzky-Golay smoothing filter was applied to the entropy data. The entropy was calculated cumulatively at each temperature step using the heat capacity derived from the Monte Carlo energy change and the temperature at that step.

$$dS = \frac{C_v}{T}dT \tag{3.1}$$

$$S = \sum dS \tag{3.2}$$

There is a resulting non-zero entropy at 0K due to the Monte Carlo supercell not being infinitely large. This correction accounts for the degeneracy in the starting

78

(ground-state) supercell due to the cell being finite, which allows for the infinite temperature limit entropy of the MC simulation to converge to the true infinite-temperature entropy $xlnx + (1-x)ln(1-x)$. The 0K entropy in the MC simulation is non-zero because there are other equivalent structures with the same energy possible for a finite supercell at 0K. The application of this correction at 0K therefore gives a more accurate estimation of the disordering temperature.

3.2.3   Computational Results

Computational Single Transition Metal Oxide Hulls

Energy hulls are generated for the O3, P2 and P3 lattice types to show the most stable lattice stacking at a given sodium concentration and given transition metal. An example of such a hull for chromium layered systems is shown in Figure 3-2, and this system will be used throughout this chapter as an exemplary system. For the Cr system, O2 phases were also considered and are included in the convex hull. Blue circles on the hull correspond to ground-states among the three systems, with red squares corresponding to configurations that are unstable with respect to the hull, but represent the lowest energy configurations for each of the three stacking types. We see that P-type configurations are ground states at 1/4, 1/3 and 1/2 sodium concentrations. For the exemplary chromium system shown in the figures, the maximum energy differences between host structure types throughout the full range of sodium content (x = 0 to 1 for Na_xCrO_2) span 50 meV per formula unit, or approximately 15 meV per atom between different stacking types. At intermediate concentrations of sodium, however, the energy differences between the three stacking types are considerably smaller. At x = 1/2 all three stacking types are shown to be very close in energy.

Figure 3-3 shows the remaining six transition metal systems in order of atomic number (a-f) that are found to reversibly intercalate sodium (Na_xMO_2 where M = Ti, V, Cr, Mn, Fe, Co and Ni). The figures show that the three stacking types, O3, P3 and P2 have very different energy in the stoichiometric (fully discharged) and fully

discharged concentrations, with O3 being the ground state at these concentrations for all seven first row TM systems. O2 phases, which are rarely recorded in experimental literature and do not appear as ground states in our calculations, have been left out of the remaining six systems for the sake of simplicity. The P3-type stacking is found to be more energetically stable than O3 and P2 at least once at intermediate concentrations between x = 0.2 and 0.6 for Ti, Cr, V and Co systems. The plots also generally show that O3, P2 and P3 draw progressively closer in energy to each other at intermediate sodium concentrations. This is typical for all of the seven first row transition metal systems studied.

In the Mn and Ni systems, O3 is stable for the entirety of the sodium concentration range and the Fe system shows very few ground states, with P2 as the most stable lattice type at 1/3 sodium concentration. The appearance of this P2 phase is unlikely in practice, however, as Fe4+ ions tend to migrate out of the layered structure as sodium ions are removed[93].

Structural comparisons of O and P-type Na ion TM Oxides

It has been hypothesized in recent studies that the relative stability of O3 and P-type transition metal oxide stacking is dependent on interlayer spacing and sodium-sodium distance in the sodium layer during deintercalation[109, 36]. We conducted a comparison of interlayer spacing for O3 and P3 stacking, once again for the Na_xCrO_2 system. P2 results were not included in this, as P2-Na_xCrO_2 has never been experimentally observed. The results are shown in Figure 3-4. This figure shows the evolution of the interlayer spacing with Na content, as computed for the P3 and O3 versions of the Na_xCrO_2 system.

Experimentally derived values are also shown for comparison. In general, interlayer spacing increases as sodium is removed from the structure, and peaks between 0.2 and 0.5 sodium. This trend is apparent in other transition metal oxides, and is indicative of the loss of attraction by sodium ions of the metal oxide layers, which acts as a "glue" or structural pillar at high concentrations of sodium. At very low concentrations (below x = 1/4), the spacing between metal oxide layers decreases
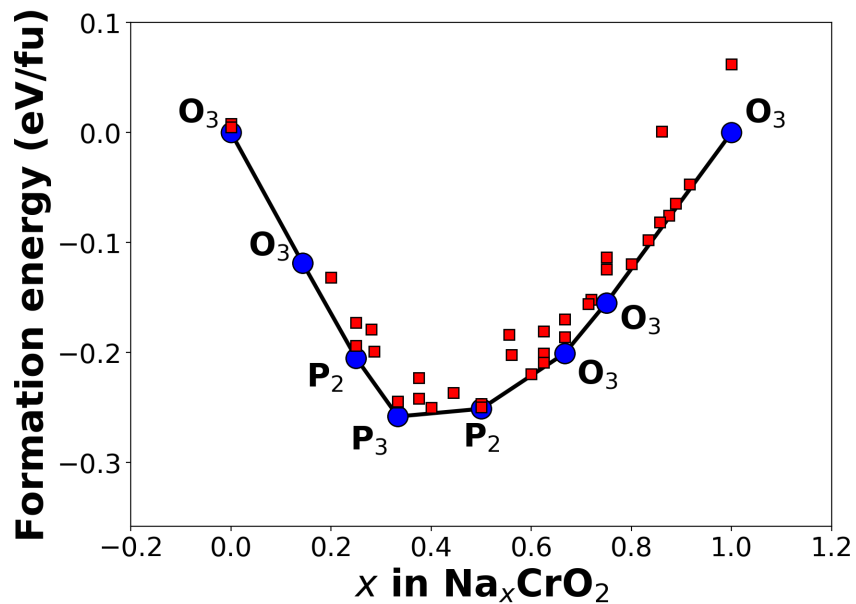
Figure 3-2: Total hull for collection of O3, P3 and P2 energy hulls for Na_xCrO_2. Red squares on the hull plot indicate computed structures which are higher in energy than the ground state phases for that sodium concentration, but represent the lowest energy configuration in their respective lattice type. Blue points on the hull indicate the ordered ground state structures for the Cr system. Black, bold lettering indicates the lattice type of the ground state configuration. At x = 0.5, all three stacking types are very close in energy (within 10 meV per formula unit).
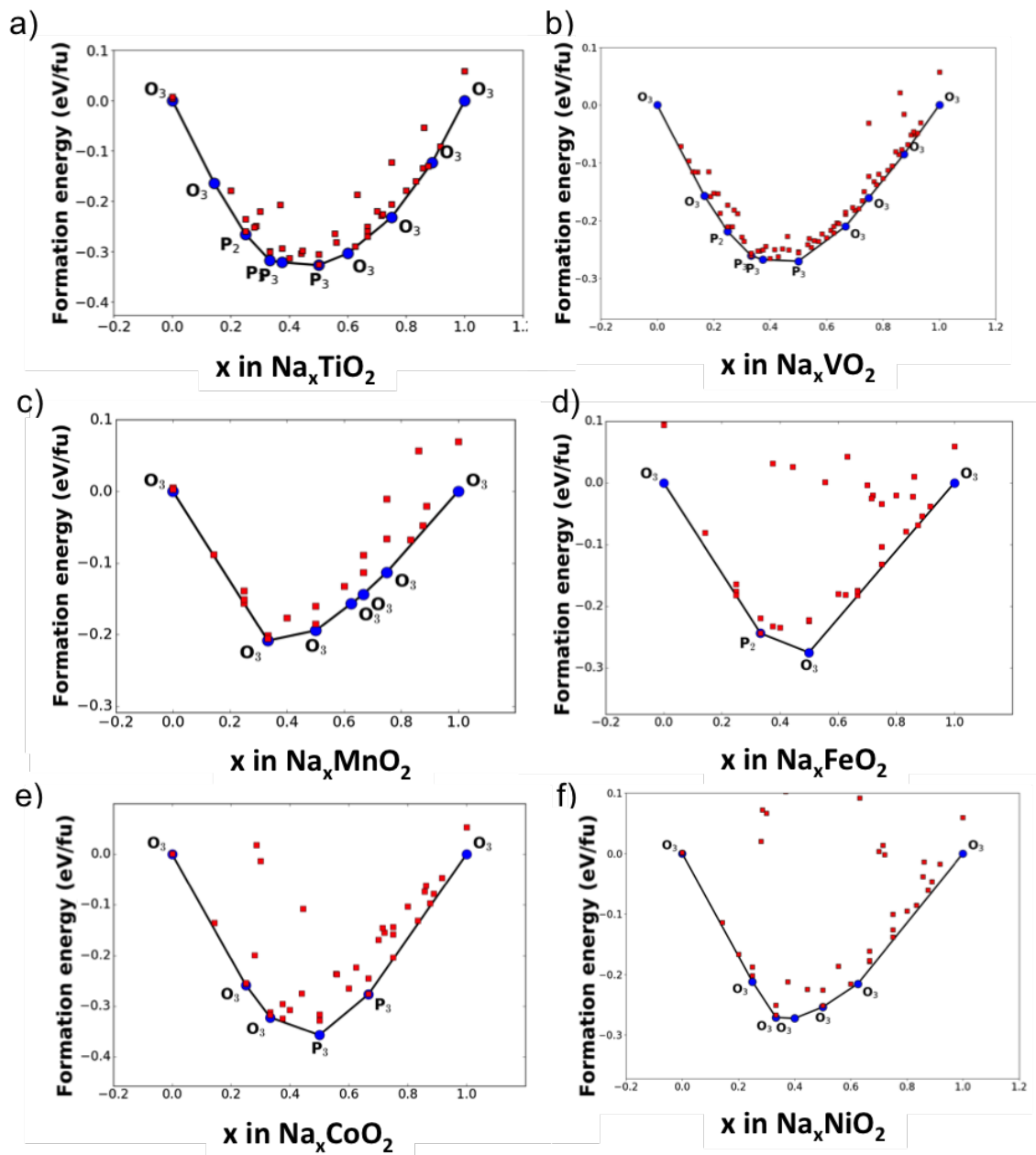
Figure 3-3: O3/P3/P2 energy hulls for Ti, V, Mn, Fe, Co and Ni single transition metal oxide systems.

again as the larger sodium ions are absent and the oxygen-oxygen repulsion alone is not strong enough to maintain the expanded interlayer spacing. The plot also shows the interlayer spacing for fully desodiated structures where one third of the chromium ions has migrated into the tetrahedral (T) and octahedral (O) sites in the sodium layer. P3 interlayer spacing is consistently larger than O3. Experimental work on Na_xCrO_2 reveals that P3-type phases begin to emerge and dominate below approximately 0.7 sodium content in the Cr system, becoming pure P-type phases below x = 0.65[12].

The figure also notes the computed interlayer spacing of fully desodiated layered Cr O3-type structures with one third of the Cr ions having migrated into the alkali layer, either in the tetrahedral (T) or octahedral (O) site. The relaxed interlayer spacing for this configuration is naturally much smaller than that of the empty layer configuration.

The average close-ranged sodium-sodium distance for the lowest energy computed P3, P2 and O3 structures for the seven sodium ion intercalating transition metal oxide systems over a range of several sodium concentrations. The results for this are shown in Figure 3-5. For sodium concentrations of 1, 3/4 and 2/3, a cutoff radius of 3.5 Å was used and the inter-sodium distances within this radius for all sodium ions in the structure was sampled. For sodium concentrations of 1/2 and 1/3, a 4.5 Å and 5.5 Å radius was used respectively, to capture the larger inter-ionic distances in these configurations. The distance calculation was limited to sodium ions within a single sodium layer.

Figure 3-5 shows that O3 structures generally feature larger sodium-sodium distances within the sodium layer than P2 type systems, except at intermediate sodium concentrations for V, Cr and Ti. This can be seen as the majority of the curves are below zero for the majority of the sodium concentration for both the P2 subplot. The most significant differences in sodium ion spacing can be seen at 1/2 sodium content. All except the Cr system exhibit smaller sodium spacing in the P2 stacking type at this concentration, and this interestingly corresponds to it being the only system with a P2 thermodynamic ground state at x = 1/2, as seen in Figure 3-2. In the
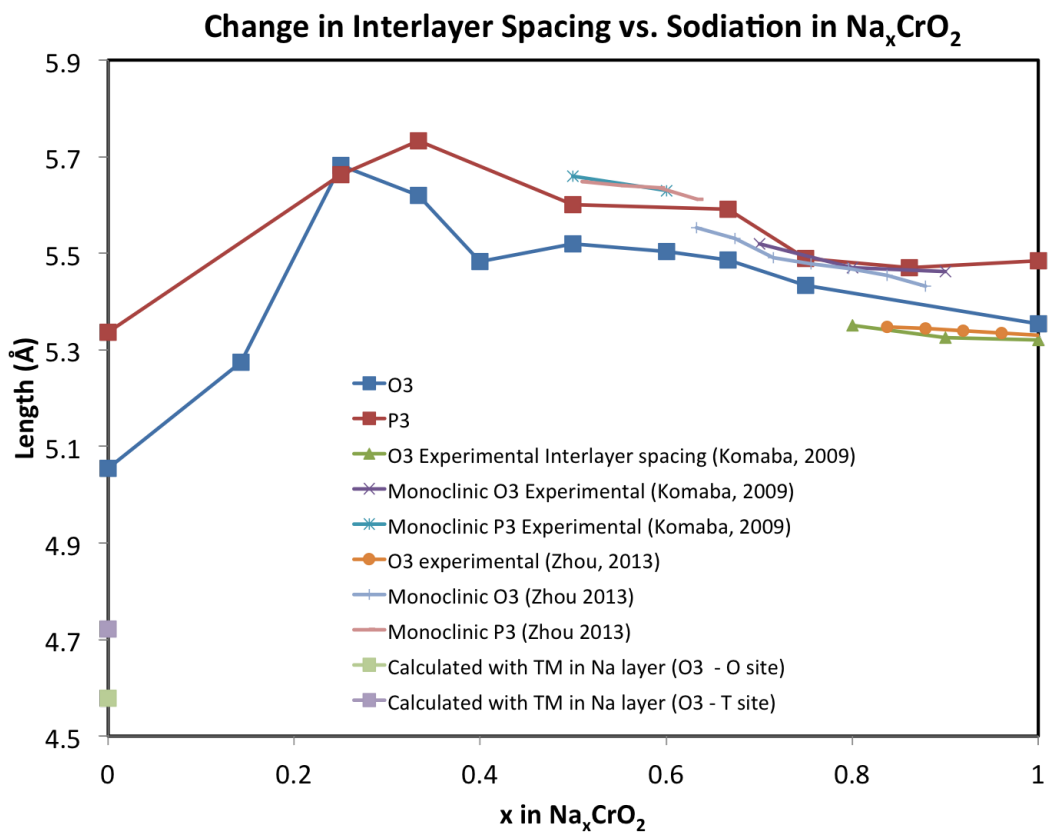
Figure 3-4: Interlayer spacing comparison between computed and experimental data on O3 and P3 Na_xCrO_2. Experimental interlayer spacing adapted from work by Komaba and Zhou[12, 13]

comparison between the P3 and O3 systems, Ti, V, Cr, Mn, and Fe all have larger sodium ion spacing than O3, with Co retaining a very similar sodium ion spacing for both the O3 and P3 systems for the entire sodium concentration range. Similarly at 2/3 sodium content, P3-Ni, V, Cr, Mn and Fe have sodium ion spacing larger than O3.

Though the plots in Figure 3-5 indicate that the difference in in-layer sodium spacing does increase between O and P type systems as sodium is removed, the correlation is reversed for P3 and P2, with P3 generally having larger in-layer sodium spacing than O3, while P2 has smaller. Both figures 3-4 and 3-5 indicate that the stacking type (O or P) is strongly dependent on electrostatic repulsion between the metal oxide layers, and correlated to the average spacing between sodium ions. At intermediate sodium concentrations, the presence of prismatic sodium sites allow for slightly larger inter-sodium spacing and larger interlayer spacing, thereby reducing the electrostatic repulsion in the system.

Stabilization of P-type phases by configurational entropy

In P-type phases there are twice the number of prismatic crystallographic sites as there are octahedral sites for alkali ions in O-type structures. As P3 and P2 lattice types have double the number of sodium ion or vacancy sites of O3, an additional stabilizing factor for P-type sodium ion oxides may come from the energy contribution of the configurational entropy at higher temperatures. P2 has two energetically different site types while all Na sites are equivalent in P3 or O3 structures. Additionally, in P-type systems, adjacent sites cannot be occupied by Na, which means sodium ion concentration has a strong influence on configurational entropy. The upper limit of configurational entropy influence in a P-type material versus an O-type can be computed analytically by considering all sites in the P-type material to be equivalent. This limit is only applicable at infinitely high temperatures, however, and breaks down in P2 at operational and synthesis temperatures because of electrostatic differences between sites. Half the available sodium sites are prisms that share edges with neighboring MO octahedra, while the other half are edge-sharing
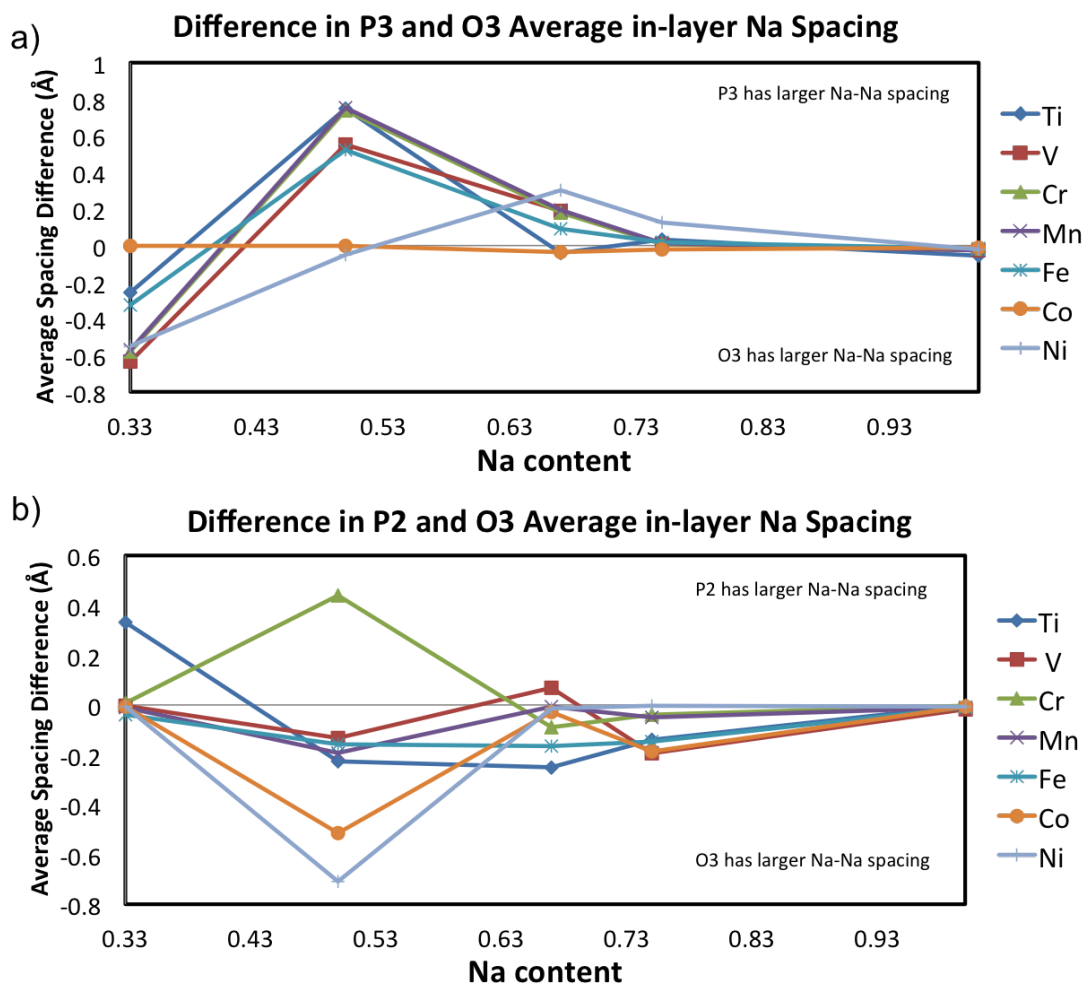
Figure 3-5: Average nearest and next-nearest neighbor Na-Na in-layer spacing within radii of 3.5 Å (x = 1, 3/4, 2/3) and 4.5 Å (x = 1/2), and 5.5 Å (x =1/3) for (a) P3 and (b) P2 computed lowest energy structures relative to O3 lowest energy structure for given Na concentration and transition metal system. The lowest energy structures here are the lowest energy sodium ion/vacancy ordered structures for a given sodium concentration and structure type. Above the horizontal for each subplot, Na-Na spacing is larger on average in the given host than in O3.

on both sides of the prismatic site. It also breaks down in P3, because as sodium is removed some transition metals in the MO layer become oxidized, so sodium sites are no longer electrostatically equivalent through each prismatic site has an edge-sharing and face-sharing end.

While all sodium sites in a P3 system are face and edge sharing on each side, making them equivalent (given all else being equal), the two sodium sites in P2 vary strongly in electrostatic energy. The energy differences of the sites in P2 for different transition metals were studied using DFT with GGA+U. These were considered maximum limits for face and edge sharing site energy as they were calculated at stoichiometric Na ($NaMO_2$). Differences appeared to be significant, on the order of 50 meV/atom. The lowest energy differences were seen in Ni and Co systems, indicating that these sites are most electrostatically similar, thus making it possible for configurational entropy to be a stronger stabilizing influence in these systems. The results are tabulated in Table 3.2

Table 3.2: Edge-sharing and face-sharing site energies for fully sodiated P2 transition metal oxides.

TM	Face-sharing (eV/atom)	Edge-sharing (eV/atom)	Difference (meV/atom)
Ti	-7.12	-7.18	-63.41
V	-6.60	-6.67	-70.70
Cr	-6.53	-6.59	-60.50
Mn	-6.23	-6.32	-91.73
Fe	-5.85	-5.91	-59.50
Co	-5.32	-5.36	-42.73
Ni	-4.62	-4.66	41.32

The actual influence of configurational entropy can be examined using Monte Carlo methods and cluster expansions of the DFT-computed configurational energies. Canonical Monte Carlo was used with three cluster expansions in the exemplary Cr system to estimate the relative influence of entropy at 1/2 stoichiometric sodium content, where sodium and vacancy disorder could be maximized. The entropy was computed from the cumulative integration of the heat capacity change with respect to temperature, and is shown in Figure 3-6. The resulting free energy plots in Figure 3-7 derived from $G = E_M C - T S_M C$ indicate that the configurational entropy influence
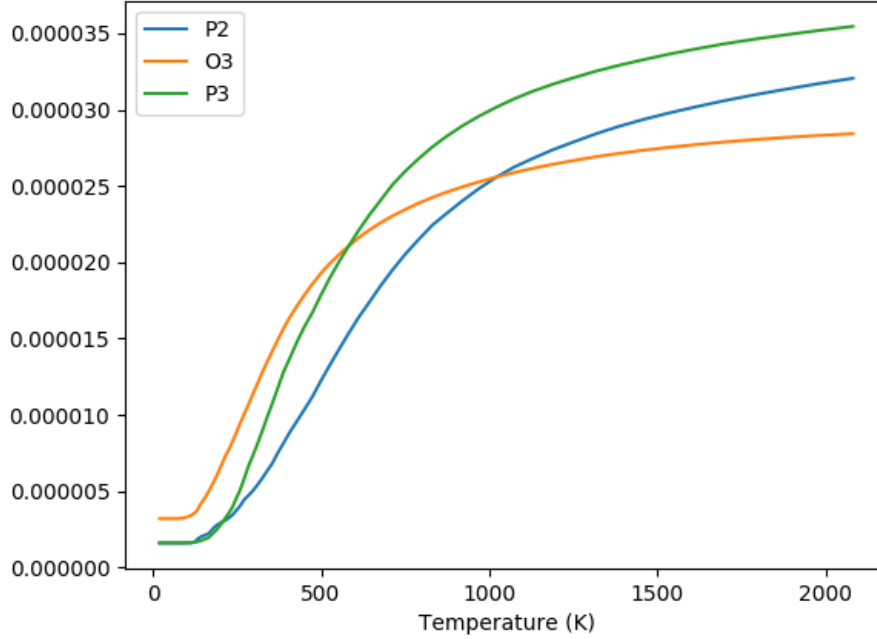
Figure 3-6: Configurational entropy vs temperature from canonical Monte Carlo simulations of the O3, P2 and P3 Na_xCrO_2 for temperatures between 20K to 2000K.

on energy changes with temperature according to the host lattice type. At very high temperatures, the entropy converges to the mixing entropy associated with doubling the number of available sodium sites in the P-type systems.

Figure 3-7 shows that although P2 starts out with the lowest free energy of the three stacking types, this is replaced by P3 at approximately 2000K. Though O3 starts out with the highest configurational entropy of the three systems at low temperatures, P3 overtakes this at approximately 600K, and P2 at 1000K. The energetic influence of entropy is very small, even at high temperatures, with the free energy difference at 2000K being within 10meV per atom between the highest and lowest energy stacking types (P2 and O3 respectively). We conclude that configurational entropy is not a dominant stabilizing mechanism for P2 at high temperatures.
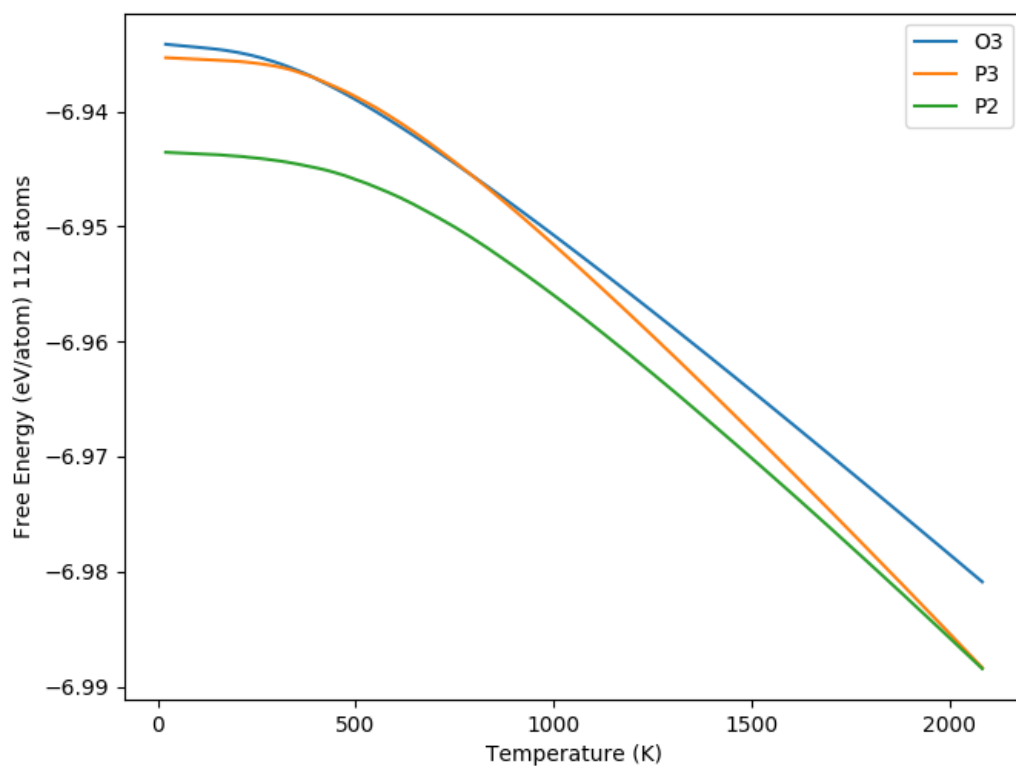
Figure 3-7: Free energy vs. temperature from canonical Monte Carlo simulations of the O3, P2 and P3 Na_xCrO_2 systems for temperatures between 20K to 2000K.

3.2.4 Discussion and Conclusions

Evidence in this section has been presented to suggest that P-type structures tend to be more stable than O-type structures at intermediate sodium ion concentrations for several single transition metal systems (Ti, V, Cr, Fe, and Co). This coincides with structural changes, wherein the average Na-Na distances and interlayer spacing in P-type structures are both shown to be larger at intermediate concentrations (between x = 0.3 and 0.7 in Na_xMO_2) for specific transition metals.

In P3 and O3 structures the sodium sites are all equivalent in terms of their immediate transition metal and oxygen environment. In O3, the sodium sites in the sodium layer are edge-sharing with transition metal oxide octahedra on either side of the layer, while in P3 all sodium prismatic sites share one edge-sharing and one face-sharing face with the metal oxide layers. P2 structures are different, however, and contain two different types of prismatic sites, where each prism is either edge-sharing or face-sharing on both sides. P2 site energy differences are estimated to be on the order of 10s of meV/atom, with lowest differences for Co and Ni. More energetically equivalent sites are expected to result in higher configurational entropy. Monte Carlo simulations indicate that the contribution from configurational entropy in the Cr system at x = 1/2 is most significant for P3 at high temperatures, however the site energy differences and restriction on filling neighboring sites in P-type structures means the contribution of the entropy to the relative stability of the three systems is small. Indeed, it appears that P-type structures are generally stabilized by electrostatics.

This stability argument lays the foundation for the more applicable understanding of what factors are needed to synthesize P2, which is discussed in the next section.

3.3 Requirements for Synthesis of P2 Layered Transition Metal Oxides

3.3.1 Introduction

The previous section examined the relative stabilities between P and O type layered morphologies in sodium ion transition metal oxide cathodes. It is interesting from a materials design perspective to understand what stabilizes the P and O stacking types. While O3 layered oxides are synthesizable for all seven first row transition metals both in single TM forms and with multiple mixed transition metals, P2 layered synthesis is particularly difficult, as explained in the previous section, as it requires a non-stoichiometric sodium content, specific transition metal selection and high synthesis temperatures. It is interesting to investigate why the mixed P2 layered oxide can be synthesized at high temperature preferentially over O3 at non-stoichiometric concentrations (typically between x = 0.6 and 0.7 for Na_xMO_2). This can lead to effective material design of the more preferable P2 stacked oxides and to an understanding of why some synthesis methods do not work. This section investigates a mechanism that may stabilize P2 over O3, and what makes P2 synthesizable with regards to transition metal selection.

We examine this through data-mining known materials in the ICSD to determine the preference of transition metals for forming mixed valence oxide phases. As P2 must be synthesized at a non-stoichiometric sodium concentration, it requires the transition metal ions to be partially oxidized above their 3+ state to compensate for the removal of sodium ions. This mixed valence structure must still form a cohesive layered octahedral structure for P2 to be synthesized. We can therefore search for prevalence of mixed versus single valence state phases in the database of known oxides for each transition metal to gauge the likelihood of stable mixed valence oxide formation. We also use data-mining of known phases to estimate the likelihood for a material to undergo a phase transition away from the layered phase at higher temperatures. An abundance of competing phases, indicated by numerous existing

stable 3+ and 4+ oxides for the transition metal in question, may be a barrier for the synthesis of P2 at high temperatures.

Ligand field theory indicates that higher spin complexes result from lower crystal field splitting energy and weak field ligands (e.g. Ti3+, Fe3+), while low spin complexes with high field ligands, such as Co3+/4+ or Ni3+/4+ result in more rigid, stronger bonds with metal[115]. This makes it easier for Ti3+ and Fe3+ ions to distort from perfect symmetry in the octahedral bond configuration. As O and P type materials have different sodium sites (octahedral and prismatic respectively), this also changes the symmetry of the metal oxide octahedra which they neighbor. We hypothesize that weak field ligand transition metal ions have a smaller tendency for perfect octahedral environments than their more rigidly bonded counterparts, and that P type metal oxide octahedra have slightly less distortion than O type, thereby making P2 synthesis more likely for low spin complexes such as Co3+ and 4+. This hypothesis can be tested using mode analysis, which quantifies the distortion of a crystallographic site from its perfect shape.

In all, these hypotheses can be seen as testing the "adaptability" of the transition metal ion, and its relation to the likelihood of P2 formation. "Adaptability" may help or hinder P2 synthesis, depending on whether the transition metal oxide can easily form lower energy non-layered structures at high temperatures.

3.3.2 Computational Methods

To test the above hypotheses, a collection of structurally and chemically unique prototypes from the 2012 version of the Inorganic Crystal Structure Database (ICSD) was gathered and labelled the "ICSD unique" collection[116]. The ICSD unique collection was sampled for binary and ternary transition metal oxides (i.e. single transition metal oxides and metal oxide ternary compounds with Na, K, Li, Cs, Rb, Ca, Mg, Ba, and Sr) and their frequency counted for each of the seven first row transition metals. The transition metal oxidation state for each compound was computed by assigning known common anionic valence and cationic valence states to the other chemical species in each compound (i.e. -2 for oxygen, and +1 or +2 for alkali or
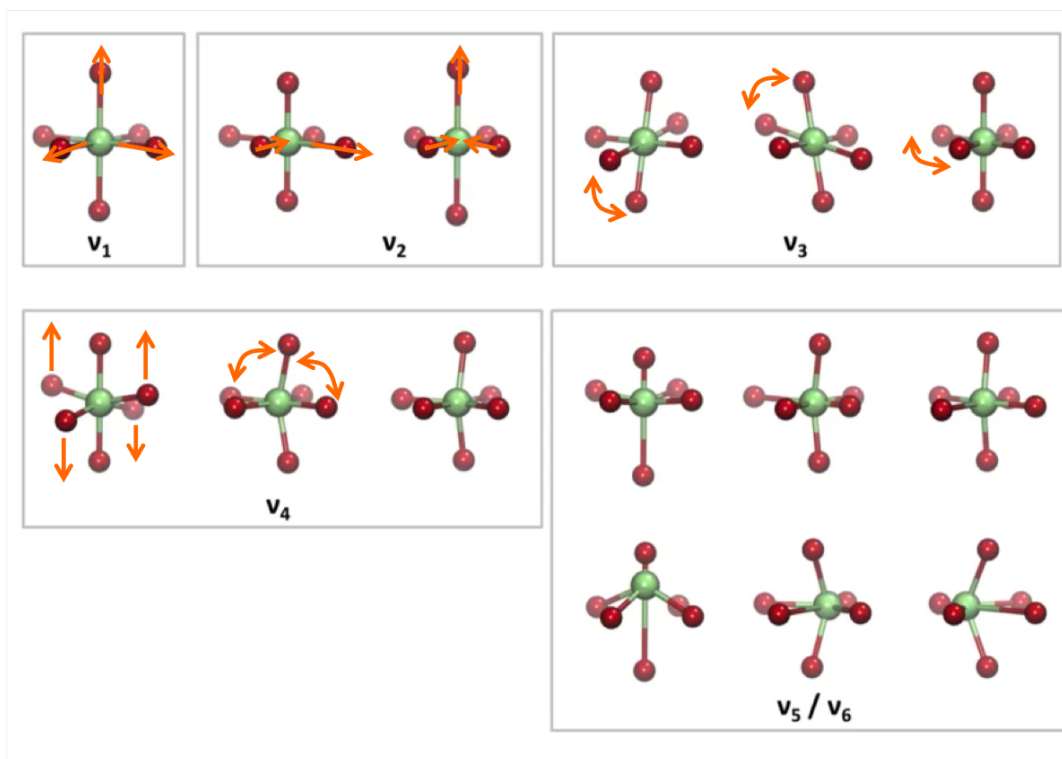
Figure 3-8: Mode analysis modes showing distortion from the perfect metal oxide octahedron. V1 mode is simple scaling, V2 is extension or contraction along one axis, V3 is the distortion of the angle between two axes, V4 is the distortion of the angles between two sets of axes and V5/V6 are modes combining V2, V3 and V4. Image adapted courtesy of Dr. Alexander Urban.

alkali earth metals respectively). The frequency of these oxidation states was tallied and the whole number oxidation state frequency was compared to "mixed valence" oxidation state frequency - i.e. how often a transition metal appeared in a binary or ternary oxide with a non-whole-number average oxidation state.

Mode Analysis for Metal Oxide Octahedra

Mode analysis for the P2 and O3 metal oxide octahedra was performed by Dr. Alexander Urban. This analysis quantified the distortion of the metal oxide octahedron from the perfectly symmetrical shape, in three degrees of freedom for each distortion mode. The modes are shown in Figure 3-8. The size of the overall distortion for each mode was given by the "norm" value which gave the absolute value of the distortion along all degrees of freedom.

93

3.3.3 Computational Results

Mode Analysis and P2 vs O3 Stability

We hypothesize that P2 complexes have less distorted TM octahedra than O3 (because the a and b lattice parameters are shorter than in O3 for equivalent Na concentration), thereby making them energetically preferable for low spin complexes. That is, when a transition metal is surrounded by weak field ligands, it has a greater tendency to distort. Conversely, this can be stated as more "flexible" high spin TM oxides favoring the O3 phase over the P2 phase.

The topotactic ground state at 2/3 Na content for both O3 and P2 systems for 7 TMs was calculated by high throughput DFT calculations as described in Chapter 2. This concentration was chosen because it allowed for simple sodium vacancy ordering and is the concentration point around which P2 is typically synthesized in experimental studies. The chosen sodium content was low enough so that both O3 and P2 could be stabilized either through synthesis (P2) or deintercalation from the stoichiometric phase (O3). For each relaxed ground state, mode analysis was performed on metal oxide octahedra for both O3 and P2 and the results compared. These results allow us to see how the octahedra deviate from perfect metal oxide octahedra. The norm indicates the (normalized) magnitude of distortion in a particular mode along three degrees of freedom.

Table 3.3: Total distortion in P2 and O3 low energy structures from perfect octahedron by TM and oxidation state (summation of v2,v3 and v4 norms)

	O3		P2	
TM	3+ total	4+ total	3+ total	4+ total
Ti	0.19	0.18	0.18	0.12
V	0.26	0.26	0.25	0.28
Cr	0.26	0.23	0.21	0.25
Mn	0.56	0.17	0.53	0.17
Fe	0.24	0.33	0.24	0.27
Co	0.21	0.19	0.21	0.19
Ni	0.43	0.16	0.26	0.27

Figure 3-9 shows the results for the V3 mode, which showed the largest distortion
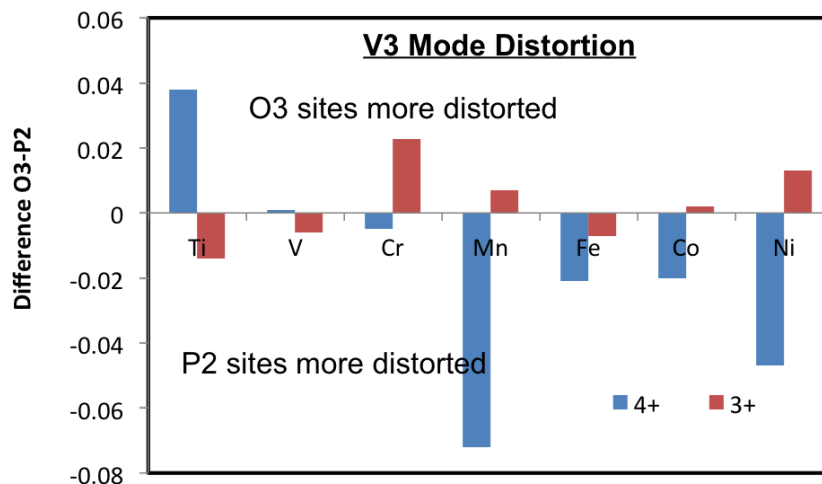
Figure 3-9: Difference in magnitude of V3 Mode distortion for 3+ and 4+ ions for O3 and P2 ground state structures. Ground state structures are the lowest energy structures appearing on the topotactic convex energy hulls for each host structure type at 2/3 sodium content.

modes by far of any of the modes examined. Other modes showed significantly smaller norms and thus negligible distortions. The largest distortions for both systems were seen in the Mn3+ and Ni3+ exhibiting the Jahn-Teller effect. The V3 mode most affected in the 3+ octahedra. O3 3+ ions tended to have slightly higher distortion than P2 3+ ions overall. The lowest distortion was apparent in O3/P2 Ti octahedra. 3+ and 4+ octahedra distortion norms were very similar, except in Ni and Mn, where strong distortion apparent in Ni3+ and Mn3+ due to Jahn-Teller effect.

Preference for forming mixed valence structures

Layered sodium ion intercalating P2 transition metal oxides are typically synthesized with approximately 2/3 of the stoichiometric sodium content of a typical O3-type transition metal oxide. In order for this to be possible, the transition metals in the oxide must have a mixed transition metal valence, to compensate for the missing sodium ions. For the seven first row transition metals examined in this thesis, this is typically a mix of 3+ and 4+ transition metal ions (though other pairings and mixes can be used). Thus transition metals that have a disinclination or difficulty in forming mixed valence phases are less likely to form P2.

This can be broadly tested by mining known, existing oxide structures recorded in the 2012 ICSD database and computing the average transition metal valence for each existing phase. Transition metals that readily exist in mixed valence states will occur more frequently as non-integer valences than those that are unstable in such arrangements. Additionally, we can mine whether 3+ or 4+ valence compounds are likely to form at all for a particular transition metal.

Results of the data-mined search, shown in Table 3.4, show that V, Mn, Co and Ni frequently appear in mixed valence states (proportion of single to mixed valence oxides is larger than 1), while Ti, Cr, Fe appear more frequently as single valence compounds. V, Mn and Co have thus far been synthesized as single TM P2 compounds. We hypothesize that Ni may also be a likely candidate for P2 but has not yet been synthesized because of its difficulty in reaching the 4+ oxidation state during synthesis. Additionally, Cr and Ni have relatively few compounds with valence between 3 and 4 (inclusive). Cr is easily oxidized to 6+ while Ni is reduced to 2+.

Table 3.4: Proportion of mixed valence to integer valence compounds in the ICSD Unique collection for binaries and ternaries of transition metal oxides with alkali and alkali earth metals.

TM	Proportion Integer to Mixed	# of compounds with average TM valence 3-4
Ti	1.5	303
V	0.73	104
Cr	4.8	35
Mn	0.56	208
Fe	3.5	257
Co	0.27	176
Ni	0.46	60

Existence of competing transition metal oxides

As P2 is typically synthesized at high temperature, some transition metal systems do not form P2 because there are many other energetically competitive phases they can form when at higher temperatures. We can test this by analyzing the 2012 ICSD database for unique structures. Unique ICSD dataset analyzed for transition metal oxides with commonly occurring elements in groups 1 and 2 (Li, Na, K, Rb, Cs, Mg,

Ca, Sr, Ba). Note, may be biased by how easy certain materials are to study (their frequency of appearance in the ICSD).

We find that Fe and Ti have largest numbers of oxide compounds, also shown in Table 3.4. This is due to the fact that iron and titanium are versatile transition metals with weak field ligands, making them adaptable to different oxide environments and ligand settings. This makes these transition metals more likely to form non-layered oxide phases at higher temperatures.The hypothesis is not supported with cobalt, as it appears to have relatively many stable competing binary oxides and ternary oxides, however still exists as a layered P2 oxide.

3.3.4   Discussion and Conclusions

Stabilization by Ligand Distortion

No apparent trend was observed for 3+ and 4+ TMO octahedra distortion in P2 vs O3. Though in O3, 3+ transition metal oxide octahedra are slightly more distorted than in P2, the difference in effect is so small as to be considered insignificant for the stabilization of either system. Ti octahedra had the lowest distortion in both P2 and O3, because of the Ti3+/4+ larger ionic radius, which is closest in size to Na+ ions of all the seven first row transition metal ions in 3+ and 4+ oxidation states.

Transition Metal Dependence

P2 synthesis requires a TM that can easily exist in mixed valence states, and forms 3+ and 4+ oxidation states readily. Both are necessary conditions for P2 synthesis. There is not a strong correlation between the number of potential competing structures and the tendency to form P2. In general, Ti and Fe have the most studied oxides, possibly due to their adaptability as weak field ligand forming ions. The tendency for nickel to form mixed valence oxides indicates that it is a viable transition metal to be synthesized in the P2 layered stacking, although the number of known nickel oxide compounds with a Ni valence between 3+ and 4+ is low and therefore not promising. The single TM form of P2 Na_xNiO_2 is likewise not found in literature. We propose

that this is due to the difficulty of synthesizing Ni3+ and 4+ ions in the correct ratio for P2 to be formed, as Ni3+ ions have a tendency to reduce to 2+ ions.

3.4   Conclusions and Future Work

We conclude that the existence of P-type layered metal oxide structures depends on the advantage in alkali ion and interlayer spacing provided by stabilizing the alkali ions in prismatic sites. This has some dependence on the transition metal selection in the system, as the electronic structure of the transition metal determines the localization of charge in the metal oxide lattice, which in turn determines the strength of electrostatic interaction between both the metal oxide layers and between the sodium ions in the alkali layers. The actual ability to synthesize P2 type structures at non-stoichiometric sodium ion concentrations further depends on the transition metal selection. The transition metal must be such that it can be synthesized at higher valence (typically 3+ and 4+ for first row transition metals) and remain stable in an octahedral environment. The transition metal must also have the tendency to form mixed valence structures. Given these conditions, P2 structures can be synthesized at high temperatures.

The analysis presented in this chapter will be completed to present a complete understanding of the stabilization mechanisms. In particular, the configurational entropy analysis is currently being applied to the Ni system, with the idea that a Ni-rich P2 oxide may eventually be synthesized given appropriate oxidizing and temperature conditions. Work is also being done on the role vibrational entropy plays in stabilizing P-type materials over O-type materials using *abinitio* phonon calculations. DFT calculations for the thermodynamic stabilities of the three competing systems are also being extended to mixed transition metal systems and systems doped with inactive materials. This work is being done by myself and other colleagues in the Ceder group, in preparation for publication this year.

Chapter 4

Sodium Ion Battery Anodes

4.1 Making graphite work for sodium

4.1.1 Introduction

As described in the previous chapters, the cost of lithium is increasing as global demand for renewable energy storage and electric vehicles grows. Reliable alternatives to lithium ion batteries are therefore needed. Sodium is globally abundant and has low-cost precursor materials, making sodium ion batteries a logical next step for large scale energy storage and EV applications[26, 57, 27]. Theoretical work has pointed out the fundamental difference between Na and Li intercalation that makes sodium ion cathodes more stable against transformation into other structures[3]. Thus, sodium ion battery cathodes are typically transition metal oxides or polyanionic compounds which can be sourced from a wide chemical space. These are very promising in terms of energy density and kinetics. Similarly, sodium ion liquid electrolytes are stable for sufficiently wide voltage windows[2]. Anode technology is rapidly becoming the chief bottleneck for commercialization of sodium ion battery technology. Current state of the art sodium ion technology uses porous hard carbon anodes[117], however these have disadvantages namely because of their relatively lower density and more costly production process. There are similar issues with the use of sodium metal alloys as anodes, which have low volumetric energy densities[118]. The use of sodium

metal is generally also seen as unstable due to dendrite formation and inhomogeneous plating when used with existing Na-ion battery electrolytes[119]. Dendrite formation presents a significant safety issue as it can cause short circuiting in the cell and lead to catastrophic cell failure.

Graphite has a number of advantages as an intercalating anodic material - it is cheap to produce, has a high volumetric density and is already a long-established technology[120, 121]. Commercial lithium ion technology chiefly relies on graphite as a negative electrode due to its high energy density and low cost. While graphite intercalates lithium reversibly, however, experiments have shown convincingly that sodium ions do not form graphite intercalation compounds (GICs). This is not, as many have suggested, simply a size issue, as graphite easily intercalates larger ions alkali ions such as potassium, cesium and rubidium, forming AC_8 complexes where A = K, Cs and Rb, for example[122] (see Fig. 4-1). Previous *abinitio* work has attempted to explain sodium's disinclination to form GICs as a combination of sodium's weak binding to graphitic sheets and the energy cost for graphitic interlayer spacing expansion[122, 123]. Furthermore, Ling's and Mizuno's ab initio calculations showed sodium ions as having positive adsorption energies on pristine graphene sheets with respect to a metallic sodium reference state[124]. While these studies help towards understanding this phenomenon, do not explain the underlying physics which makes sodium ions so profoundly different from their neighbors in the alkali column of the periodic table.

Recent work has shown that changing the chemical and electronic structure of graphene and graphitic sheets can allow them to bind sodium ions successfully[125, 124, 126]. Computational studies on boron-doped graphene sheets show successful Na adsorption[124]. Partially oxidized (expanded) graphites[125] have been shown to reversibly intercalate sodium ions, sodium ions in coordination with electrolyte molecules or electronegative elements have been shown to form GICs[127]. Jache and Kim successfully reversibly cycled Na ions in graphite using electrolyte co-intercalation phenomena[128, 129]. These types of solutions are not ideal, however, because they require difficult pre-treatment of the graphite (such as partial reduction of oxidized
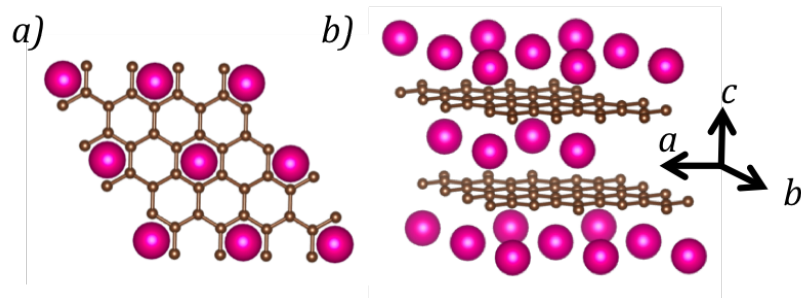
Figure 4-1: Alkali ions intercalated into graphite in a stage I structure with the AC_8 stoichiometry. Stage I structure refers to a graphite intercalated compound where all layers contain the intercalant, i.e. there is just one graphitic sheet between each layer of intercalant.

graphite) and typically result in relatively low densities of stored sodium and relatively high interlayer spacing. Previous work on sodium co-intercalation with alkaline earth metals has shown very limited to no success[130]. It would be extremely beneficial to enable sodium ion intercalation into graphite close to the morphologies and atomic densities of other existing alkali GICs, such as potassium. Earlier work has also been conducted suggesting that sodium ions can co-intercalate into graphite when paired with potassium ions to form an allegedly stage-I GIC with the composition NaK_2C_{12} [131, 132]. If real, this material could pave the way for co-intercalation battery electrodes with two more more active ions, where both Na^+ and K^+ ions are cycled from a mixed Na-K cathode, or a pre-potassiated graphitic anode for sodium ion batteries.

4.1.2 Graphite Co-Intercalation

In this chapter, the underlying physical cause of graphite's inability to intercalate sodium ions is examined. Initially, the likelihood of sodium intercalation through electronic alteration of the graphite lattice is tested through graphite oxidation via a hypothetical fluoride dopant. It is then shown, through experimental and computational methods, that Na-K co-intercalation into graphite is not thermodynamically favorable and previously identified NaK_2C_{12} compounds are likely unstable, and in reality are combinations of the Na_2K alloy and the KC_8 GIC. This chapter further aims to explain physically why sodium does not readily intercalate into undoped

graphite sheets, and propose design principles based on a combination of experimental and computational work, as well as findings in literature, on how graphite may be chemically altered to intercalate sodium ions for use in sodium ion battery anodes.

4.1.3 Computational Methods

Initial hypothetical "fluoridated" sodium-intercalated graphite calculations were computed with DFT with GGA+U as described in previous chapters. DFT energy calculations for this chapter were performed using the Vienna Ab initio Simulation Package (VASP) [42] within the projector-augmented wave approach[43], using the Perdew-Burke-Ernzerhof (PBE) generalized-gradient approximation (GGA) [44] functional and the vdW-DF2 functional, encompassing van der Waals interactions[133]. Van der Waals interactions were used in the simulation to more accurately represent the weak interactions between the graphitic sheets.

Several van der Waals methods were tested and the vdW-DF2 functional, as implemented in VASP, was found to give the highest accuracy in terms of lattice parameters and voltages of known GICs. This functional was also established as the most accurate for determining lattice constants, diffusion barriers and binding energies for Li ions within a layered graphite matrix[134]. The benchmarking parameters used are described in Tables 4.1 and 4.2, with vdW-DF2 showing negative intercalation voltages for sodium ions, as observed in experiments. Experimental lattice parameters were derived from the Inorganic Crystal Structure Database (ICSD)[116] and sources found through WebElements.com[135, 136].

Table 4.1: Benchmarking *ab initio* techniques against experimentally obtained lattice parameters (atomic separation in metallic solid) and interlayer spacing

Compound	Experimental (Å)	GGA	DFT-D2	vdW-DF2
C	3.35	3.80	3.33	3.42
LiC_6	3.71	3.70	3.67	3.70
KC_8	5.40	5.38	5.36	5.41
K (separation in solid)	4.61	4.69	4.59	4.59
Na (separation in solid)	3.72	3.71	3.53	3.65

Table 4.2: Benchmarking *ab initio* techniques against experimentally observed intercalation voltages

Compound	DFT-D2	vdW-DF2	GGA
LiC_6	0.75	0.14	0.18
NaC_8	0.36	-0.16	0.09
NaC_6	0.36	-0.14	-0.01
KC_8	0.57	0.31	0.30

The average intercalation potential of the graphite anodes was obtained using energies computed within DFT[48, 3],

$$V = -\frac{E(A_nH) - E(A_{n-x}H) - xE(A)}{xe} \qquad (4.1)$$

where A is the alkali ion, H is the host structure and e is the electronic charge.

Co-intercalated K-Na GIC structures were generated based on the stage-I KC_8 and stage-I LiC_6 crystal structure files in the ICSD. The convex hull of an intercalation system is given by the linear combination of ground states which gives the lowest energy at any composition between a completely empty and a completely full host complex. A voltage curve is generated from the energy differences of these ground states along the convex hull. A ternary phase diagram extends this to two dimensions with three end compositions, in this case C, Na and the co-intercalating alkali metal. The ternary phase diagrams in this chapter were constructed using the energy hull method with use of the pymatgen code package[47].

Possible K_2NaC_{12} crystal structures were generated using the KC_8 GIC crystal structure from the Inorganic Crystal Structure Database (ICSD)[116]. As the alkali metal concentration in the proposed phase is higher than that of KC_8, potential additional metal sites were identified between the potassium sites in a hexagonal (close-packed) arrangement, leading to an MC_2 structure. The M sites were then enumerated with Na and K atoms to give a K_2NaC_{12} (MC_4) composition. The "distorted" structures were generated by moving one half of the metal ions either above or below the in-layer plane, and enumerated with the appropriate metal composition. A total of approximately 800 test structures were computed for the potassium system.

For subsequent Cs and Rb phase diagrams, the $\approx$200 lowest energy configurations from the potassium system were selected (less than 20 meV per atom above the hull) and computed with Cs and Rb in place of the K ions.

Table 4.3: U Values for Seven First Row Transition Metals in an Oxide Environment

Composition	Number of Configurations	Na:K ratio
$NaKC_{16}$	15	1:1
Na_3KC_{32}	175	3:1
Na_7KC_{64}	35	7:1
$Na_{15}KC_{128}$	171	15:1

4.2 Computational Results

4.2.1 Graphite Oxidation for Sodium Ion Intercalation

An initial study was conducted to evaluate how the oxidation of graphite through doping could contribute to sodium ion intercalation. This was achieved by inserting fluorine into the graphite structure at various points within the graphite layers, as depicted in Figure 4-3. Fluorine bonds strongly with carbon and fluorine GICs are well documented[137, 138], so the non-physical fluorinated structures used in this study placed fluorine close to the graphite lattice in order to slightly oxidize the electronic structure of the graphite layers.

Figure 4-4 shows that the insertion voltage of sodium ions is negative for pure graphite, meaning it does not spontaneously intercalate, which agrees with experimental observation. Insertion voltage for sodium with F replacing one of the sodium ions is also shown to be negative, meaning spontaneous intercalation is not possible. For F adjacent to sodium ions, however, either in a vacant site or in an interstitial configuration, the insertion voltage becomes positive, meaning sodium ions would spontaneously intercalate into this lattice based on thermodynamics alone. This implies that only a small chemical change is needed for sodium insertion into graphite to become spontaneous.
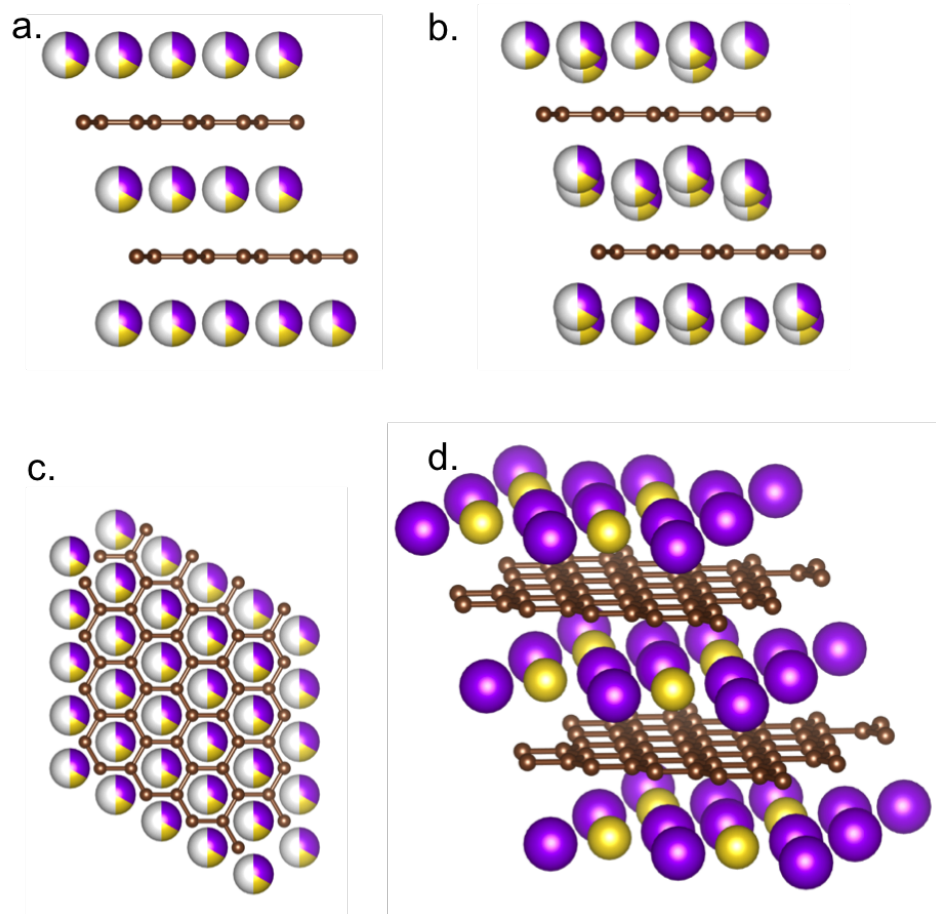
Figure 4-2: Development of potential K_2NaC_{12} structures
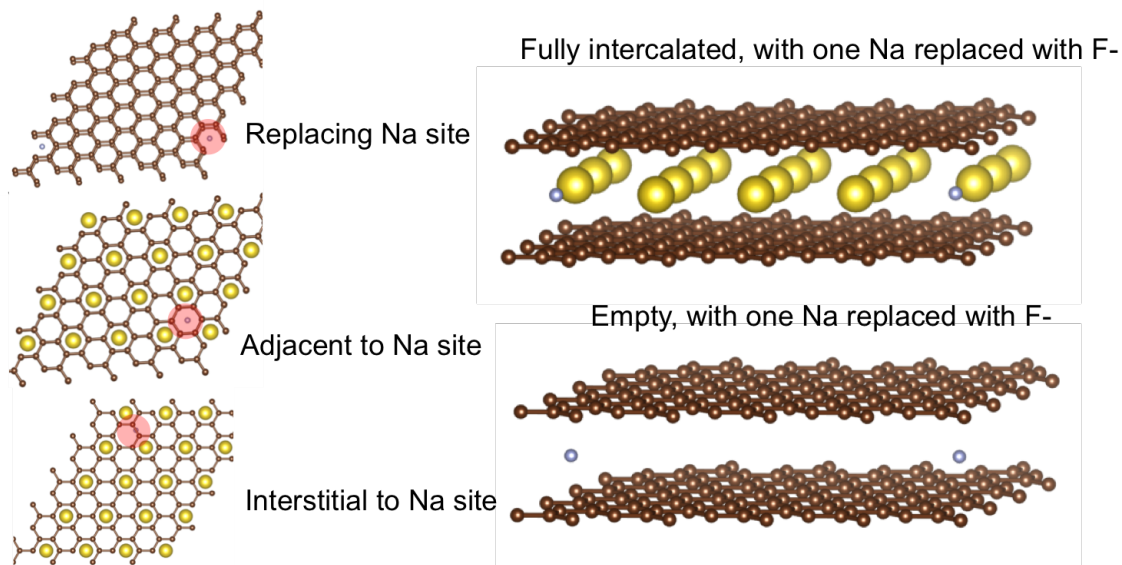
Figure 4-3: Tested graphite structures with intercalated sodium and hypothetical fluorine doping. Sodium is placed in the AC_6 configuration observed in lithium GICs. Fluorine is inserted at and interstitial to potential sodium sites. Fluorine insertion positions are highlighted in red.
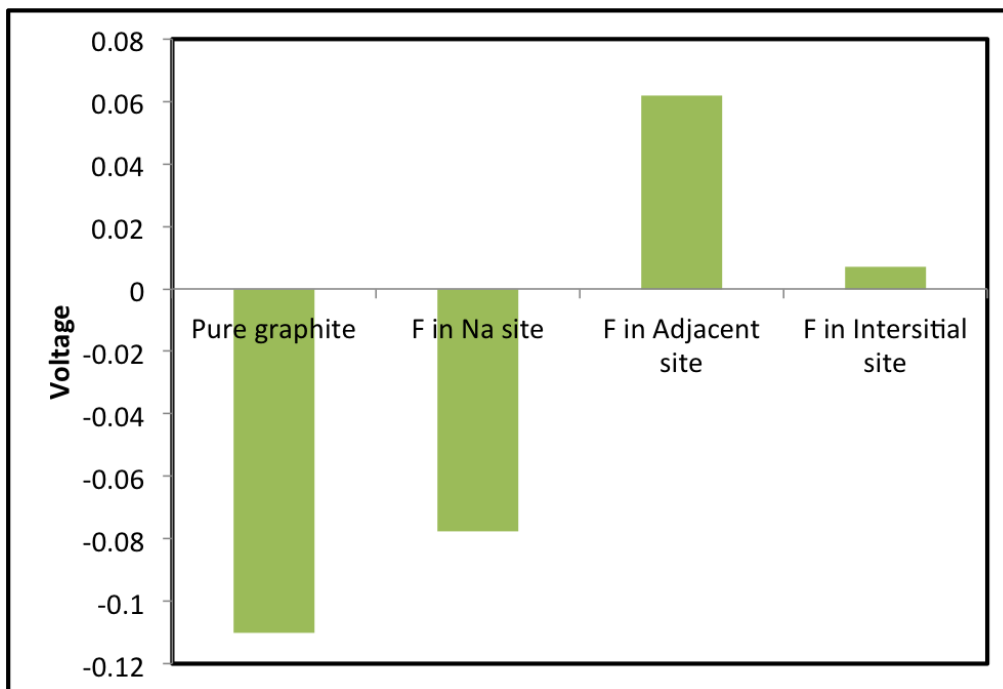
Figure 4-4: Insertion voltage for sodium into graphite shown with fluorine doping. Insertion voltage for sodium into pure graphite and with F replacing one of the sodium ions is shown to be negative, meaning spontaneous intercalation is not possible. For F adjacent to sodium ions either in a vacant site or in an interstitial configuration the insertion voltage becomes positive.
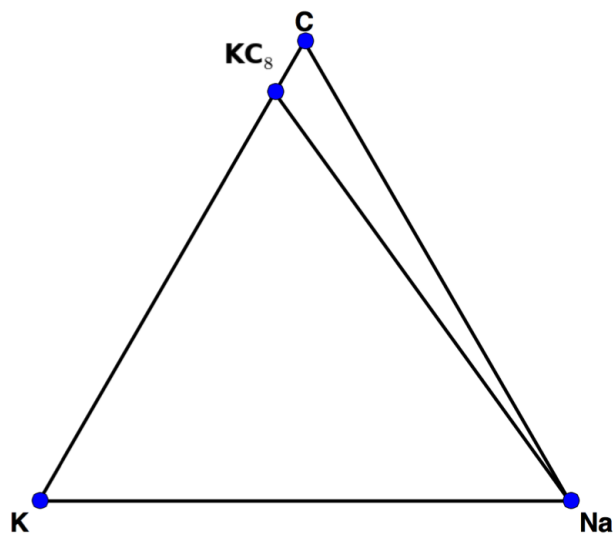
Figure 4-5: Van der Waals computational phase diagram at 0K of Na, K, C with stable phases marked

4.2.2 Potassium and Sodium Co-Intercalation into Graphite

Several van der Waals *abinitio* methods were benchmarked using intercalation voltage for several experimentally known GICs and the lattice parameters of graphite, K-GIC and metals. The 0 Kelvin Na-K-C phase diagram was constructed computationally based on the vdW-DF2 computed energies. It was found that no thermodynamically stable co-intercalated Na-K GICs exist, including compositions where Na and K are staged (filling alternate layers) and mixed in-plane. The sample set also included compositions where some graphite layers were left empty (stage-I/II hybrid structures). *Abinitio* energy calculations similarly showed that none of the proposed K_2NaC_{12} appeared on the energy hull.

Similar phase diagrams were constructed for the Na-Cs-C and Na-Rb-C systems also using vdW-DF2 computed energies. These are shown in Figures 4-6 and 4-7. In these systems, it was similarly confirmed that thermodynamically stable co-intercalation was not possible.

107
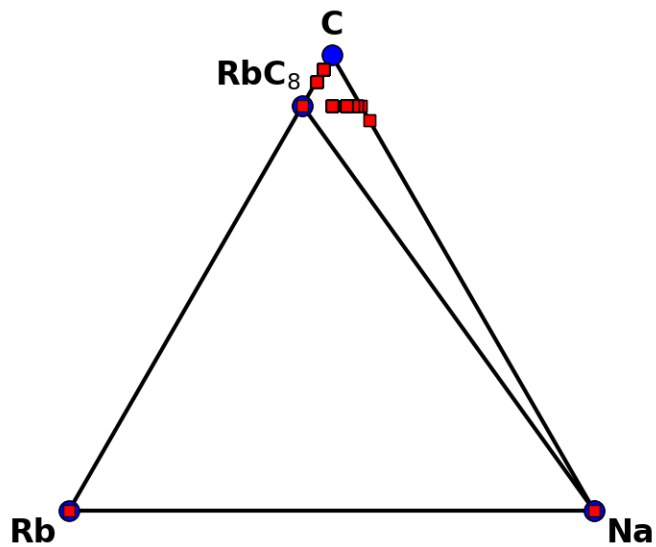
Figure 4-6: Van der Waals computational phase diagram at 0K of Na, Rb, C with stable phases marked in blue and unstable phases marked in red.
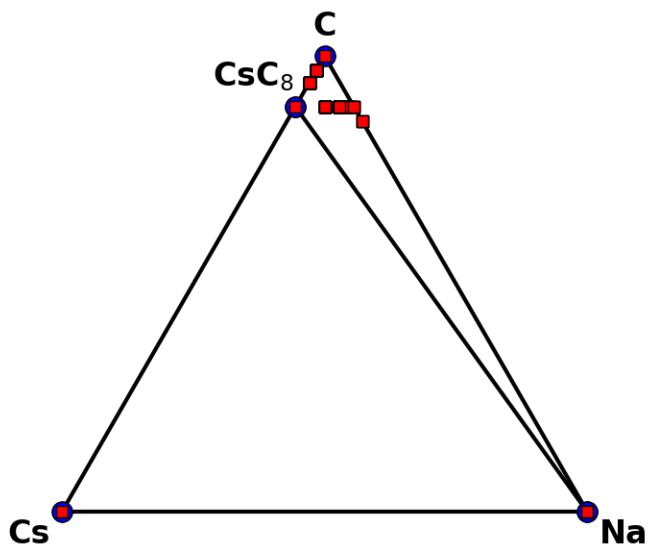
Figure 4-7: Van der Waals computational phase diagram at 0K of Na, Cs, C with stable phases marked in blue and unstable phases marked in red.

4.2.3 Stability of K_2NaC_{12} Phase

4.3 Experimental Results

Attempts to synthesize a stable K-Na co-intercalated GIC proved unsuccessful. A mixed K/Na electrolyte system (half cell and full cell) was prepared to test the possibility of co-intercalation of potassium and sodium, and electrochemically cycled. No evidence of sodium co-intercalation was present in the electrochemical characterization. Next, pre-potassiated graphite was also synthesized to be used as an electrode material, and this too proved unsuccessful in intercalating sodium ions, as shown in Figure 4-8. Simulated x-ray diffraction (XRD) patterns were constructed from computed potential crystal structures for K_2NaC_{12}, for comparison with known experimentally observed XRD patterns for this proposed GIC, as well as pure graphite, stage-I KC_8 and Na_2 metal alloy. The comparison was not fruitful, however, as attempted intercalation was unsuccessful, and thus experimentally derived XRD patterns could be identified only as K-GIC.

4.4 Discussion and Conclusions

4.4.1 Existence of stable K-Na GICs and K_2NaC_{12}

While K GICs are well documented, K-Na GICs are not plausible given the results of this study. We propose that sodium ion intercalation requires specific electronic interaction between graphite and sodium ions, which can only be achieved when the graphite is slightly oxidized or when the sodium ion is changed chemically (for example when surrounded by co-intercalating ligands). Intercalated potassium does not significantly change the electronic structure of the graphite and thus is not effective in allowing for sodium intercalation. Furthermore, the metallic density in a proposed intercalated K_2NaC_{12} GIC would be too high for the proposed interlayer spacing. Inter-ionic distances between Na and K would have to be below 3 Å which would result in very strong electrostatic repulsion. The atomic density is twice as high as
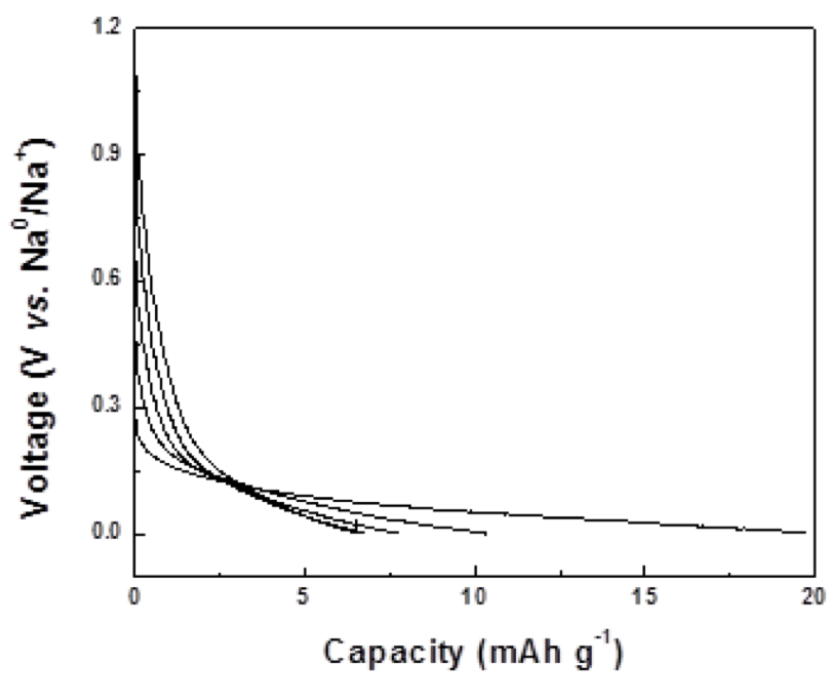
Figure 4-8: Electrochemical testing of KC8 with Na metal with charges to 0.4 V, 0.6 V, 0.8 V, 1.0 V and 1.2 V and discharging to 0.001 V. No noticeable Na storage was observed. Synthesis and electrochemical testing conducted by Haegyeom Kim.

it is in known KC_8 and higher even than the highest attainable density of stage-I intercalated lithium GIC (LiC_6).

The intercalation voltage changes from positive to negative when a fluoride ion is inserted into the graphite structure in a simulated phase. The strong C-F pairing changes the electronic structure of graphite sufficiently to allow sodium intercalation to occur. We thereby propose that slight "effective" graphite oxidation of the graphite lattice is needed to intercalate sodium ions, though not so for other alkali metals.

The alkali metals are the most electropositive group of metals, meaning they are most likely to donate an electron and have very low ionization energies. When moving down the alkali metal group from lithium, to sodium, potassium and heavier alkali metals, the electropositivity of the element increases (its electronegativity decreases). Thus the larger, more electropositive alkali metals interact with the electronic structure of the graphite, making them thermodynamically favorable intercalants. Lithium ions are exceptional to this trend, however their smaller size and closer packing on the graphite lattice layer (LiC_6 versus AC_8) means they can interact with graphite sufficiently to allow for stable intercalation.

4.5   Future Work

As noted earlier in this chapter, potassium has also been explored as a possible candidate active ion to replace lithium and sodium in rechargeable batteries[139]. Though K-ions are significantly larger than either, they have been shown to reversibly intercalate both into layered oxides[140] and also into graphite[141], making K-ion batteries potentially fruitful for future battery material development. Current capacities for K-ion layered oxide cathodes remain low, however they are a viable avenue for further study in alternatives to lithium ion battery technology. This work is on-going in the Ceder group[142].

Chapter 5

Design Principles and Conclusions

5.1 Design Principles for Sodium Ion Battery Cathodes

This thesis gleans insights into the functional properties of layered metal oxide cathodes for sodium ion batteries from first principles investigations. From extensive high-throughput computation we can observe trends based on transition metal selection, host type and sodium ion concentration, and use these to make recommendations for general sodium ion oxide cathode material design.

5.1.1 Transition metal mixing

Transition metal ion oxidation state ordering in layered single transition metal oxides is strongly coupled to the sodium ion ordering, as shown in Chapter 2. This can be mitigated by transition metal mixing and doping the transition metal oxide layer with inactive species to break up strong, long range electrostatic interactions of strongly coupled, highly ordered patterns. The decoupling of sodium ion interaction and transition metal oxidation state ordering leads to weaker sodium ion ordering, which leads to fewer first order vacancy-ordering phase transitions throughout the electrochemical cycle. As phase transitions lead to lower cyclability, removing reversible phase transitions from the electrochemical cycling process is useful.

Transition metal mixing is also required to optimize the functional properties of the active cathode material. The 3+ to 4+ oxidation voltage for each transition metal contributes to the overall energy density of the material. Therefore a higher concentration of "high voltage" transition metals such as Fe or Co are preferable when optimizing the material for energy density. Mixing transition metals must be done with care, however, as interaction between transition metals within the metal oxide lattice can result in an undesirable oxidation state. For example, the presence of easily-reduced Ni3+ ions with easily oxidized Fe3+ ions results in the oxidation of Fe to 4+ and the reduction of Ni3+ to 2+. The 2+ to 3+ oxidation voltage is lower than Fe3+ to 4+ and Ni3+ to 4+, thereby resulting in an overall lower average voltage for the entire electrochemical cycle of the cathode material.

5.1.2 Host lattice stacking

The host metal oxide lattice stacking (synthesized either as O3 or P2) influences the material function. P2 is generally found to be vastly superior to O in terms of diffusivity and rate capability as it does not rely on the divacancy mechanism for alkali ion diffusion. It has also been found to retain its stacking for a larger sodium concentration range than O3 for certain transition metal combinations, as the latter has a tendency to transform to a P3 stacking through slab glide.

5.2 Conclusions

Alternatives to lithium ion batteries are becoming an inevitability in today's energy storage landscape. With sodium ion batteries, we are presented with an opportunity to utilize existing infrastructure to produce safe, reliable batteries on a commercial and industrial scale. Energy density for sodium ion batteries is limited by sodium's standard electrode potential. Due to their larger size, however, sodium ions are well suited to stabilize a wide variety of layered systems. In terms of simple, single transition metal layered oxides, sodium ions can be reversibly intercalated for all seven first row transition metals, compared to just two (cobalt and nickel) for lithium

ions. When considering that these can also be mixed in multiple proportions, this provides us with a vast chemical space in which to search for cathode materials. Sodium ion transition metal layered oxides are currently the state of the art for sodium ion cathode materials, however little is understood about the mechanisms that govern their synthesis and behavior during electrochemical cycling. It is of great importance to establish how sodium ion layered oxides are stabilized and what phase transitions they undergo during (de)-intercalation, as this can lead to a more complete understanding of the materials, and thus efficient, intelligent material design. These insights can also be extrapolated to provide understanding of other alkali systems and non-layered systems. The Ceder group is uniquely suited to gain such insights, as it incorporates theoretical, computational and experimental studies and allows for efficient and open collaboration between these fields.

In this thesis, sodium-intercalating layered transition metal oxides were studied to examine their tendency to transition between phases during electrochemical cycling, as well as their tendency to form different stacking types. The most commonly synthesized O3-type layered oxides were considered in Chapter 2, where their potential sodium ion vacancy ordering phase transitions were predicted for all seven single transition metal systems, and the energy effects of ordering within sodium layers and stacking between adjacent layers was studied. Additionally, the effect of mixing transition metals was discussed, as well as phase transitions away from the layered structure.

In Chapter 3, the relative stability of P-type stacking configurations of sodium ion layered transition metal oxides was discussed with regard to sodium content and transition metal selection. Parameters required for the synthesis of P2 layered oxides were hypothesized and tested. The relative stability at 0K of P2, P3 and O3 layered oxides was considered for all seven first row TM systems, and possible mechanisms for their relative stabilization were described. Through data-mining of existing transition metal oxide structures present in the ICSD, P2 synthesis was found to be possible for transition metals that occur frequently in mixed-valence oxide compounds, i.e. where their average oxidation state is non-integer. We concluded that Ni, which

is also frequently found in mixed-valence nickel oxide compounds, could exist as a single transition metal P2 oxide if it can be synthesized in a sufficiently oxidizing environment.

Chapter 4 examined the possibility of altering graphite to make it feasible as an anode material for sodium ion batteries by oxidation or by co-intercalation with potassium, which is known to form graphite intercalated compounds (GICs) while sodium does not. It was shown that oxidation is at least hypothetically a viable route for sodium ion intercalation, though oxidized graphite may not be practically better than other existing anode materials. It also showed that co-intercalation with other ions is not viable as it does not alter the electronic structure of the graphite sufficiently to make sodium ions intercalate, thus disputing previously published work.

When summarized, these studies show the possibilities and pitfalls associated with making sodium ion batteries viable. Phase transformations in layered oxide cathodes affect battery function and differ greatly between well-known lithium ion batteries and sodium-ion batteries, and so require understanding to facilitate novel material design. Layered sodium ion transition metal oxides in particular differ greatly from their lithium ion counterparts, and undergo numerous reversible phase transitions during electrochemical cycling because of the stronger electrostatic interaction between sodium ions. Though transition metal choice is important to cathode function, stable sodium ion vacancy ordering patterns occur repeatedly among all seven first row transition metal oxide systems. Transition metal oxidation state ordering is coupled to sodium ion vacancy ordering, so the mixing of transition metals in the oxide lattice can help improve cyclability by reducing ordering strength.

Sodium ions can exist in prismatic as well as octahedral sites in these layered systems, allowing for P-type systems to be synthesized both chemically and electrochemically from O-type. Such P-type systems are known to generally have better rate capability than O-type systems because of their different diffusion mechanism and higher alkali ion diffusivity in their layers. We show that the ability to form P-type structures is dependent on both sodium ion content and transition metal selection. We see that the unique interaction between sodium ions and pure graphite

116

does not allow for sodium intercalation, though larger alkali ions can be intercalated. This means that either the graphitic anodes or sodium ion intercalants must be altered chemically before graphite can be used in sodium ion batteries. From these pieces of fundamental understanding we can recommend design criteria for active materials in sodium ion batteries that allow for them to be competitive and commercially viable.

Bibliography

[1] J.-M. Tarascon and M. Armand. Issues and challenges facing rechargeable lithium batteries. *Nature*, 414(6861):359–367, nov 2001.

[2] Naoaki Yabuuchi, Kei Kubota, Mouad Dahbi, and Shinichi Komaba. Research Development on Sodium-Ion Batteries. *Chem. Rev.*, 114(23):11636–11682, dec 2014.

[3] Shyue Ping Ong, Vincent L. Chevrier, Geoffroy Hautier, Anubhav Jain, Charles Moore, Sangtae Kim, Xiaohua Ma, and Gerbrand Ceder. Voltage, stability and diffusion barrier differences between sodium-ion and lithium-ion intercalation materials. *Energy Environ. Sci.*, 4(9):3680, 2011.

[4] Raphaële J. Clément, Peter G. Bruce, and Clare P. Grey. Review-Manganese-Based P2-Type Transition Metal Oxides as Sodium-Ion Battery Cathode Materials. *J. Electrochem. Soc.*, 162(14):A2589–A2604, 2015.

[5] Xin Li, Yan Wang, Di Wu, Lei Liu, Shou-Hang Bo, and Gerbrand Ceder. JahnâĂŞTeller Assisted Na Diffusion for High Performance Na Ion Batteries. *Chem. Mater.*, 28(18):6575–6583, sep 2016.

[6] C DELMAS, J BRACONNIER, C FOUASSIER, and P HAGENMULLER. Electrochemical intercalation of sodium in NaxCoO2 bronzes. *Solid State Ionics*, 3-4:165–169, aug 1981.

[7] Yifei Mo, Shyue Ping Ong, and Gerbrand Ceder. Insights into Diffusion Mechanisms in P2 Layered Oxide Materials by First-Principles Calculations. *Chem. Mater.*, 26(18):5208–5214, 2014.

[8] Shou Hang Bo, Xin Li, Alexandra J. Toumar, and Gerbrand Ceder. Layered-to-Rock-Salt Transformation in Desodiated NaxCrO2 (x 0.4). *Chem. Mater.*, 28(5):1419–1429, 2016.

[9] Xin Li, Xiaohua Ma, Dong Su, Lei Liu, Robin Chisnell, Shyue Ping Ong, Hailong Chen, Alexandra Toumar, Juan-Carlos Idrobo, Yuechuan Lei, Jianming Bai, Feng Wang, Jeffrey W Lynn, Young S Lee, and Gerbrand Ceder. Direct visualization of the Jahn-Teller effect coupled to Na ordering in Na5/8MnO2. *Nat. Mater.*, 13(6):586–92, jun 2014.

[10] Christophe Didier, Marie Guignard, Jacques Darriet, and Claude Delmas. O'3-NaxVO2 System: A Superstructure for Na 1/2 VO 2. *Inorg. Chem.*, 51(20):11007–11016, oct 2012.

[11] Plousia Vassilaras, Alexandra J. Toumar, and Gerbrand Ceder. Electrochemical properties of NaNi1/3Co1/3Fe1/3O2 as a cathode material for Na-ion batteries. *Electrochem. commun.*, 38:79–81, jan 2014.

[12] Shinichi Komaba, Tetsuri Nakayama, Atsushi Ogata, Takaya Shimizu, Chikara Takei, S Takada, A Hokura, and I Nakai. Electrochemically Reversible Sodium Intercalation of Layered NaNi0.5Mn0.5O2 and NaCrO2. In *ECS Trans.*, pages 43–55. ECS, 2009.

[13] Yong-Ning Zhou, Jing-Jing Ding, Kyung-Wan Nam, Xiqian Yu, Seong-Min Bak, Enyuan Hu, Jue Liu, Jianming Bai, Hong Li, Zheng-Wen Fu, and Xiao-Qing Yang. Phase transition behavior of NaCrO2 during sodium extraction studied by synchrotron-based X-ray diffraction and absorption spectroscopy. *J. Mater. Chem. A*, 1(37):11130, 2013.

[14] Kei Kubota and Shinichi Komaba. Review-Practical Issues and Future Perspective for Na-Ion Batteries. *J. Electrochem. Soc.*, 162(14):A2538–A2550, 2015.

[15] David Linden and Thomas B. Reddy, editors. *Handbook of Batteries*. McGraw-Hill, 3rd edition, 2002.

[16] Weidong Zhou, Yutao Li, Sen Xin, and John B. Goodenough. Rechargeable Sodium All-Solid-State Battery. *ACS Cent. Sci.*, page acscentsci.6b00321, jan 2017.

[17] Ian Lawrence Matts. *Multi-redox active polyanionic cathodes for alkali-ion batteries*. PhD thesis, Massachusetts Institute of Technology, 2016.

[18] J. Vetter, P. Novák, M.R. Wagner, C. Veit, K.-C. Möller, J.O. Besenhard, M. Winter, M. Wohlfahrt-Mehrens, C. Vogler, and A. Hammouche. Ageing mechanisms in lithium-ion batteries. *J. Power Sources*, 147(1-2):269–281, sep 2005.

[19] Kisuk Kang and Gerbrand Ceder. Factors that affect Li mobility in layered lithium transition metal oxides. *Phys. Rev. B*, 74(9):094105, sep 2006.

[20] Alexander Urban, Dong-Hwa Seo, and Gerbrand Ceder. Computational understanding of Li-ion batteries. *npj Comput. Mater.*, 2:16002, mar 2016.

[21] Zelang Jian, Liang Zhao, Huilin Pan, Yong-Sheng Hu, Hong Li, Wen Chen, and Liquan Chen. Carbon coated Na3V2(PO4)3 as novel electrode material for sodium ion batteries. *Electrochem. commun.*, 14(1):86–89, jan 2012.

[22] Hyungsub Kim, Inchul Park, Dong-Hwa Seo, Seongsu Lee, Sung-Wook Kim, Woo Jun Kwon, Young-Uk Park, Chul Sung Kim, Seokwoo Jeon, and Kisuk Kang. New Iron-Based Mixed-Polyanion Cathodes for Lithium and Sodium Rechargeable Batteries: Combined First Principles Calculations and Experimental Study. *J. Am. Chem. Soc.*, 134(25):10369–10372, jun 2012.

[23] Tsutomu Ohzuku and Yoshinari Makimura. Layered Lithium Insertion Material of LiNi 1/2 Mn 1/2 O 2 : A Possible Alternative to LiCoO 2 for Advanced Lithium-Ion Batteries. *Chem. Lett.*, 30(8):744–745, aug 2001.

[24] Xin Xia and J. R. Dahn. NaCrO2 is a Fundamentally Safe Positive Electrode Material for Sodium-Ion Batteries with Liquid Electrolytes. *Electrochem. Solid-State Lett.*, 15(1):A1, 2012.

[25] L. Wang, T. Maxisch, and G. Ceder. A First-Principles Approach to Studying the Thermal Stability of Oxide Cathode Materials. *Chem. Mater.*, 19(3):543–552, feb 2007.

[26] Michael D. Slater, Donghan Kim, Eungje Lee, and Christopher S. Johnson. Sodium-Ion Batteries. *Adv. Funct. Mater.*, 23(8):947–958, feb 2013.

[27] Sung-Wook Wook Kim, Dong-Hwa Hwa Seo, Xiaohua Ma, Gerbrand Ceder, and Kisuk Kang. Electrode Materials for Rechargeable Sodium-Ion Batteries: Potential Alternatives to Current Lithium-Ion Batteries. *Adv. Energy Mater.*, 2(7):710–721, jul 2012.

[28] Rachel Brazil. A salt ion battery. *Chem. Ind.*, 78(10):24–27, oct 2014.

[29] P. A. Cox. *Transition Metal Oxides: An introduction to their electronic structure and properties.* Oxford University Press, Oxford, 1992.

[30] J.D. Dunitz and L.E. Orgel. Electronic properties of transition-metal oxidesâĂŤI. *J. Phys. Chem. Solids*, 3(1-2):20–29, jan 1957.

[31] J.D. Dunitz and L.E. Orgel. Electronic properties of transition-metal oxides-II. *J. Phys. Chem. Solids*, 3(3-4):318–323, jan 1957.

[32] K. Ghiassi and R. J. Lancashire. Jahn-Teller Distortions, 2016.

[33] Kliment I Kugel' and D I KhomskiÄŋ. The Jahn-Teller effect and magnetism: transition metal compounds. *Sov. Phys. Uspekhi*, 25(4):231–256, apr 1982.

[34] Jeremy K. Burdett. *Chemical Bonding in Solids.* Oxford University Press, Oxford, 1995.

[35] Alexandra J. Toumar, Shyue Ping Ong, William Davidson Richards, Stephen Dacek, and Gerbrand Ceder. Vacancy Ordering in O3-Type Layered Metal Oxide Sodium-Ion Battery Cathodes. *Phys. Rev. Appl.*, 4(6):064002, dec 2015.

[36] Maxwell D. Radin and Anton Van der Ven. Stability of Prismatic and Octahedral Coordination in Layered Oxides and Sulfides Intercalated with Alkali and Alkaline-Earth Metals. *Chem. Mater.*, 28(21):7898–7904, nov 2016.

[37] O.A. Smirnova, M. Avdeev, V.B. Nalbandyan, V.V. Kharton, and F.M.B. Marques. First observation of the reversible O3âĘŤP2 phase transition. *Mater. Res. Bull.*, 41(6):1056–1062, jun 2006.

[38] Xiaohua Ma, Hailong Chen, and Gerbrand Ceder. Electrochemical Properties of Monoclinic NaMnO2. *J. Electrochem. Soc.*, 158(12):A1307, 2011.

[39] Jürgen Hafner, Christopher Wolverton, and Gerbrand Ceder. Toward Computational Materials Design: The Impact of Density Functional Theory on Materials Research. *MRS Bull.*, 31(09):659–668, sep 2006.

[40] Kieron Burke. *The ABC of DFT*. Berkeley, 2007.

[41] M. Born and R. Oppenheimer. Zur Quantentheorie der Molekeln. *Ann. Phys.*, 389(20):457–484, 1927.

[42] G. Kresse and J. Furthmüller. Efficient iterative schemes for ab initio total-energy calculations using a plane-wave basis set. *Phys. Rev. B*, 54(16):11169–11186, oct 1996.

[43] P. E. Blöchl. Projector augmented-wave method. *Phys. Rev. B*, 50(24):17953–17979, dec 1994.

[44] John P. Perdew, Matthias Ernzerhof, and Kieron Burke. Rationale for mixing exact exchange with density functional approximations. *J. Chem. Phys.*, 105(22):9982, 1996.

[45] Lei Wang, Thomas Maxisch, and Gerbrand Ceder. Oxidation energies of transition metal oxides within the GGA+U framework. *Phys. Rev. B*, 73(19):195107, may 2006.

[46] Anubhav Jain, Geoffroy Hautier, Shyue Ping Ong, Charles J. Moore, Christopher C. Fischer, Kristin A. Persson, and Gerbrand Ceder. Formation enthalpies by mixing GGA and GGA + U calculations. *Phys. Rev. B - Condens. Matter Mater. Phys.*, 84(4):1–10, 2011.

[47] Anubhav Jain, Geoffroy Hautier, Charles J. Moore, Shyue Ping Ong, Christopher C. Fischer, Tim Mueller, Kristin A. Persson, and Gerbrand Ceder. A high-throughput infrastructure for density functional theory calculations. *Comput. Mater. Sci.*, 50(8):2295–2310, jun 2011.

[48] M. K. Aydinol, A. F. Kohan, G. Ceder, K. Cho, and J. Joannopoulos. Ab initio study of lithium intercalation in metal oxides and metal dichalcogenides. *Phys. Rev. B*, 56(3):1354–1365, jul 1997.

[49] J. Sanchez and D. de Fontaine. Theoretical prediction of ordered superstructures in metallic alloys. In *Ind. Chem. Libr. Struct. Bond. Cryst. 2*, pages 117–132. Academic Press, 1981.

[50] G. Ceder, H. Dreyssé, and D. de Fontaine. Triplet interactions and the c(2x2) overlayer phase diagram. *Phys. A Stat. Mech. its Appl.*, 193(1):105–113, feb 1993.

[51] A. Van der Ven and G. Ceder. Vacancies in ordered and disordered binary alloys treated with the cluster expansion. *Phys. Rev. B*, 71(5):054102, feb 2005.

[52] M. K. Y. Chan, J. Reed, D. Donadio, T. Mueller, Y. S. Meng, G. Galli, and G. Ceder. Cluster expansion and optimization of thermal conductivity in SiGe nanowires. *Phys. Rev. B*, 81(17):174303, may 2010.

[53] Lance J. Nelson, Gus L. W. Hart, Fei Zhou, and Vidvuds OzoliĀȨš. Compressive sensing as a paradigm for building physics models. *Phys. Rev. B*, 87(3):035125, jan 2013.

[54] Greg Mills and Hannes Jónsson. Quantum and thermal effects in H2 dissociative adsorption: Evaluation of free energy barriers in multidimensional quantum s. *Phys. Rev. Lett.*, 72(7):1124–1127, feb 1994.

[55] Geoffroy Hautier, Anubhav Jain, Hailong Chen, Charles Moore, Shyue Ping Ong, and Gerbrand Ceder. Novel mixed polyanions lithium-ion battery cathode materials predicted by high-throughput ab initio computations. *J. Mater. Chem.*, 21(43):17147, 2011.

[56] Allen J. Bard and Larry R. Faulker. *Electrochemical Methods: Fundamentals and Applications*. Wiley New York, 2 edition, 2001.

[57] Shinichi Komaba, Wataru Murata, Toru Ishikawa, Naoaki Yabuuchi, Tomoaki Ozeki, Tetsuri Nakayama, Atsushi Ogata, Kazuma Gotoh, and Kazuya Fujiwara. Electrochemical Na Insertion and Solid Electrolyte Interphase for Hard-Carbon Electrodes and Application to Na-Ion Batteries. *Adv. Funct. Mater.*, 21(20):3859–3867, oct 2011.

[58] A. Maazaz, C. Delmas, and P. Hagenmuller. A study of the Na x TiO2 system by electrochemical deintercalation. *J. Incl. Phenom.*, 1(1):45–51, 1983.

[59] C. Didier, M. Guignard, C. Denage, O. Szajwaj, S. Ito, I. Saadoune, J. Darriet, and C. Delmas. Electrochemical Na-Deintercalation from NaVO2. *Electrochem. Solid-State Lett.*, 14(5):A75, 2011.

[60] J.J. Braconnier, C. Delmas, and P. Hagenmuller. ETUDE PAR DESINTERCALATION ELECTROCHIMIQUE DES SYSTEMES NaxCrO 2 ET NaxNiO 2. *Mat. Res. Bull.*, 17:993–1000, 1982.

[61] Shinichi Komaba, Chikara Takei, Tetsuri Nakayama, Atsushi Ogata, and Naoaki Yabuuchi. Electrochemical intercalation activity of layered NaCrO2 vs. LiCrO2. *Electrochem. commun.*, 12(3):355–358, mar 2010.

[62] A. Mendiboure, C. Delmas, and P. Hagenmuller. Electrochemical intercalation and deintercalation of NaxMnO2 bronzes. *J. Solid State Chem.*, 57(3):323–331, may 1985.

[63] Yasuo Takeda, Kazuaki Nakahara, Motoaki Nishijima, Nobuyuki Imanishi, Osamu Yamamoto, Mikio Takano, and Ryoji Kanno. Sodium deintercalation from sodium iron oxide. *Mater. Res. Bull.*, 29(6):659–666, jun 1994.

[64] S. Kikkawa, S. Miyazaki, and M. Koizumi. Electrochemical aspects of the deintercalation of layered AMO2 compounds. *J. Power Sources*, 14(1-3):231–234, jan 1985.

[65] P. Vassilaras, X. Ma, X. Li, and G. Ceder. Electrochemical Properties of Monoclinic NaNiO2. *J. Electrochem. Soc.*, 160(2):A207–A211, nov 2012.

[66] Marie Guignard, Christophe Didier, Jacques Darriet, Pierre Bordet, Erik Elkaïm, and Claude Delmas. P2-NaxVO2 system as electrodes for batteries and electron-correlated materials. *Nat. Mater.*, 12(1):74–80, nov 2012.

[67] C. Delmas, C. Fouassier, and P. Hagenmuller. Structural classification and properties of the layered oxides. *Phys. B+C*, 99(1-4):81–85, jan 1980.

[68] Zhonghua Lu and J. R. Dahn. In Situ X-Ray Diffraction Study of P2-Na2/3Ni1/3Mn2/3O2. *J. Electrochem. Soc.*, 148(11):A1225, 2001.

[69] M. E. Arroyo y de Dompablo, A. Van der Ven, and G. Ceder. First-principles calculations of lithium ordering and phase stability on LixNiO2. *Phys. Rev. B*, 66(6):064112, aug 2002.

[70] Yanli Wang, Yi Ding, and Jun Ni. Ground-state phase diagram of Na x CoO 2 : correlation of Na ordering with CoO 2 stacking sequences. *J. Phys. Condens. Matter*, 21(3):035401, jan 2009.

[71] Ying S. Meng, Yoyo Hinuma, and Gerbrand Ceder. An investigation of the sodium patterning in NaxCoO2 (0.5âĽďxâĽď1) by density functional theory methods. *J. Chem. Phys.*, 128(10):104708, mar 2008.

[72] C. Wolverton and Alex Zunger. First-Principles Prediction of Vacancy Order-Disorder and Intercalation Battery Voltages in LixCoO2. *Phys. Rev. Lett.*, 81(3):606–609, jul 1998.

[73] A. Van der Ven, M. K. Aydinol, G. Ceder, G. Kresse, and J. Hafner. First-principles investigation of phase stability in LixCoO2. *Phys. Rev. B*, 58(6):2975–2987, aug 1998.

[74] Yuesheng Wang, Ruijuan Xiao, Yong-Sheng Hu, Maxim Avdeev, and Liquan Chen. P2-Na0.6[Cr0.6Ti0.4]O2 cation-disordered electrode for high-rate symmetric rechargeable sodium-ion batteries. *Nat. Commun.*, 6:6954, apr 2015.

[75] Makoto Kaburagi and Junjiro Kanamori. Ground State Structure of Triangular Lattice Gas Model with up to 3rd Neighbor Interactions. *J. Phys. Soc. Japan*, 44(3):718–727, mar 1978.

[76] M.E Arroyo y de Dompablo and G Ceder. First-principles calculations on LixNiO2: phase stability and monoclinic distortion. *J. Power Sources*, 119-121:654–657, jun 2003.

[77] Gus L. W. Hart and Rodney W. Forcade. Algorithm for generating derivative structures. *Phys. Rev. B*, 77(22):224115, jun 2008.

[78] Gerbrand Ceder and Anton Van der Ven. Phase diagrams of lithium transition metal oxides: investigations from first principles. *Electrochim. Acta*, 45(1-2):131–150, sep 1999.

[79] Yukio Saito and Ganji Tabe. \(\sqrt{3}\times\sqrt{3}\) Structure on the Triangular Lattice. *J. Phys. Soc. Japan*, 54(8):2955–2962, aug 1985.

[80] Yoyo Hinuma, Ying S. Meng, and Gerbrand Ceder. Temperature-concentration phase diagram of P2-NaxCoO2 from first principles. *Phys. Rev. B*, 77(22):224111, jun 2008.

[81] Fei Zhou, Thomas Maxisch, and Gerbrand Ceder. Configurational Electronic Entropy and the Phase Diagram of Mixed-Valence Oxides: The Case of LixFePO4. *Phys. Rev. Lett.*, 97(15):155704, oct 2006.

[82] Di Wu, Xin Li, Bo Xu, Nancy Twu, Lei Liu, and Gerbrand Ceder. NaTiO 2 : a layered anode material for sodium-ion batteries. *Energy Environ. Sci.*, 8(1):195–202, 2015.

[83] David Hamani, Mohamed Ati, Jean-Marie Tarascon, and Patrick Rozier. NaxVO2 as possible electrode for Na-ion batteries. *Electrochem. commun.*, 13(9):938–941, sep 2011.

[84] Man Huon Han, Elena Gonzalo, Montse Casas-Cabanas, and Teófilo Rojo. Structural evolution and electrochemistry of monoclinic NaNiO2 upon the first cycling process. *J. Power Sources*, 258:266–271, jul 2014.

[85] Naoaki Yabuuchi, Masataka Kajiyama, Junichi Iwatate, Heisuke Nishikawa, Shuji Hitomi, Ryoichi Okuyama, Ryo Usui, Yasuhiro Yamada, and Shinichi Komaba. P2-type Nax[Fe1/2Mn1/2]O2 made from earth-abundant elements for rechargeable Na batteries. *Nat. Mater.*, 11(6):512–517, apr 2012.

[86] Kei Kubota, Issei Ikeuchi, Tetsuri Nakayama, Chikara Takei, Naoaki Yabuuchi, Hiromasa Shiiba, Masanobu Nakayama, and Shinichi Komaba. New Insight into Structural Evolution in Layered NaCrO2 during Electrochemical Sodium Extraction. *J. Phys. Chem. C*, 119(1):166–175, jan 2015.

[87] G CEDER, P D TEPESCH, A F KOHAN, and A VAN DER VEN. A Model to Predict Ionic Disorder and Phase Diagrams: Application to CaO-MgO, Gd2O3-ZrO2 and to Sodium βâĂİ-Alumina'. *J. Electroceramics*, 1(1):15–26, 1997.

[88] Jan N. Reimers. Electrochemical and In Situ X-Ray Diffraction Studies of Lithium Intercalation in Li[sub x]CoO[sub 2]. *J. Electrochem. Soc.*, 139(8):2091, 1992.

[89] Y. Shao-Horn, S. Levasseur, F. Weill, and C. Delmas. Probing Lithium and Vacancy Ordering in O3 Layered Li[sub x]CoO[sub 2] (x=0.5). *J. Electrochem. Soc.*, 150(3):A366, 2003.

[90] C. Chazel, M. Ménétrier, L. Croguennec, and C. Delmas. Coupled Ion/Electron Hopping in Li x NiO 2 : A 7 Li NMR Study. *Inorg. Chem.*, 45(3):1184–1191, feb 2006.

[91] Xin Li, Di Wu, Yong-Ning Zhou, Lei Liu, Xiao-Qing Yang, and Gerbrand Ceder. O3-type Na(Mn0.25Fe0.25Co0.25Ni0.25)O2: A quaternary layered cathode compound for rechargeable Na ion batteries. *Electrochem. commun.*, 49:51–54, dec 2014.

[92] Shyue Ping Ong, William Davidson Richards, Anubhav Jain, Geoffroy Hautier, Michael Kocher, Shreyas Cholia, Dan Gunter, Vincent L. Chevrier, Kristin A. Persson, and Gerbrand Ceder. Python Materials Genomics (pymatgen): A robust, open-source python library for materials analysis. *Comput. Mater. Sci.*, 68:314–319, feb 2013.

[93] Hiroaki Yoshida, Naoaki Yabuuchi, and Shinichi Komaba. NaFe0.5Co0.5O2 as high energy and power positive electrode for Na-ion batteries. *Electrochem. commun.*, 34:60–63, sep 2013.

[94] Christophe Didier, Marie Guignard, Matthew R. Suchomel, Dany Carlier, Jacques Darriet, and Claude Delmas. Thermally and Electrochemically Driven Topotactical Transformations in Sodium Layered Oxides Na x VO 2. *Chem. Mater.*, 28(5):1462–1471, mar 2016.

[95] Anton Van der Ven, John C. Thomas, Qingchuan Xu, Benjamin Swoboda, and Dane Morgan. Nondilute diffusion from first principles: Li diffusion in LixTiS2. *Phys. Rev. B*, 78(10):104306, sep 2008.

[96] Lei Liu, Xin Li, Shou-Hang Bo, Yan Wang, Hailong Chen, Nancy Twu, Di Wu, and Gerbrand Ceder. High-Performance P2-Type Na 2/3 (Mn 1/2 Fe 1/4 Co 1/4)O 2 Cathode Material with Superior Rate Capability for Na-Ion Batteries. *Adv. Energy Mater.*, 5(22):1500944, nov 2015.

[97] Zhonghua Lu, R. A. Donaberger, and J. R. Dahn. Superlattice Ordering of Mn, Ni, and Co in Layered Alkali Transition Metal Oxides with P2, P3, and O3 Structures. *Chem. Mater.*, 12(12):3583–3590, dec 2000.

[98] Jie Zhao, Jing Xu, Dae Hoe Lee, Nikolay Dimov, Ying Shirley Meng, and Shigeto Okada. Electrochemical and thermal properties of P2-type Na2/3Fe1/3Mn2/3O2 for Na-ion batteries. *J. Power Sources*, 264:235–239, oct 2014.

[99] Hiroaki Yoshida, Naoaki Yabuuchi, Kei Kubota, Issei Ikeuchi, Arnd Garsuch, Martin Schulz-Dobrick, and Shinichi Komaba. P2-type Na2/3Ni1/3Mn2/3-xTixO2 as a new positive electrode for higher energy Na-ion batteries. *Chem. Commun.*, 50(28):3677, 2014.

[100] A. Caballero, L. Hernán, J. Morales, L. Sánchez, J. Santos Peña, and M. A. G. Aranda. Synthesis and characterization of high-temperature hexagonal P2-Na0.6 MnO2 and its electrochemical behaviour as cathode in sodium cells. *J. Mater. Chem.*, 12(4):1142–1147, mar 2002.

[101] Naoaki Yabuuchi, Ryo Hara, Kei Kubota, Jens Paulsen, Shinichi Kumakura, and Shinichi Komaba. A new electrode material for rechargeable sodium batteries: P2-type Na 2/3 [Mg 0.28 Mn 0.72]O 2 with anomalously high reversible capacity. *J. Mater. Chem. A*, 2(40):16851–16855, aug 2014.

[102] Xuehang Wu, Gui-Liang Xu, Guiming Zhong, Zhengliang Gong, Matthew J. McDonald, Shiyao Zheng, Riqiang Fu, Zonghai Chen, Khalil Amine, and Yong Yang. Insights into the Effects of Zinc Doping on Structural Phase Transition of P2-Type Sodium Nickel Manganese Oxide Cathodes for High-Energy Sodium Ion Batteries. *ACS Appl. Mater. Interfaces*, 8(34):22227–22237, aug 2016.

[103] Daniel Buchholz, Christoph Vaalma, Luciana Gomes Chagas, and Stefano Passerini. Mg-doping for improved long-term cyclability of layered Na-ion cathode materials âĂŞ The example of P2-type NaxMg0.11Mn0.89O2. *J. Power Sources*, 282:581–585, may 2015.

[104] Elahe Talaie, Victor Duffort, Hillary L. Smith, Brent Fultz, and Linda F. Nazar. Structure of the high voltage phase of layered P2-Na2/3-z[Mn1/2Fe1/2]O2 and the positive effect of Ni substitution on its stability. *Energy Environ. Sci.*, 8(8):2512–2523, 2015.

[105] Dae Hoe Lee, Jing Xu, and Ying Shirley Meng. An advanced cathode for Na-ion batteries with high rate and excellent structural stability. *Phys. Chem. Chem. Phys.*, 15(9):3304, 2013.

[106] Romain Berthelot, Whitney Schmidt, A.W. Sleight, and M.A. Subramanian. Studies on solid solutions based on layered honeycomb-ordered phases P2-Na2M2TeO6 (M=Co, Ni, Zn). *J. Solid State Chem.*, 196:225–231, dec 2012.

[107] Raphaële J. Clément, Juliette Billaud, A. Robert Armstrong, Gurpreet Singh, Teófilo Rojo, Peter G. Bruce, and Clare P. Grey. Structurally stable Mg-doped P2-Na 2/3 Mn 1-y Mg y O 2 sodium-ion battery cathodes with high rate performance: insights from electrochemical, NMR and diffraction studies. *Energy Environ. Sci.*, 9(10):3240–3251, 2016.

[108] R. J. Clément, J. Xu, D. S. Middlemiss, J. Alvarado, C. Ma, Y. S. Meng, and C. P. Grey. Direct evidence for high Na + mobility and high voltage structural processes in P2-Na x [LiyNizMn(1-y-z)]O2 (x, y, z<1) cathodes from solid-state NMR and DFT calculations. *J. Mater. Chem. A*, 5(8):4129–4143, 2017.

[109] Nebil A. Katcho, Javier Carrasco, Damien Saurel, Elena Gonzalo, Man Han, Frederic Aguesse, and Teofilo Rojo. Origins of Bistability and Na Ion Mobility Difference in P2- and O3-Na 2/3 Fe 2/3 Mn 1/3 O 2 Cathode Polymorphs. *Adv. Energy Mater.*, page 1601477, sep 2016.

[110] Daniel Buchholz, Luciana Gomes Chagas, Christoph Vaalma, Liming Wu, and Stefano Passerini. Water sensitivity of layered P2/P3-Na x Ni 0.22 Co 0.11 Mn 0.66 O 2 cathode material. *J. Mater. Chem. A*, 2(33):13415, jun 2014.

[111] Young Hwa Jung, Ane S. Christiansen, Rune E. Johnsen, Poul Norby, and Do Kyung Kim. In Situ X-Ray Diffraction Studies on Structural Changes of a P2 Layered Material during Electrochemical Desodiation/Sodiation. *Adv. Funct. Mater.*, 25(21):3227–3237, jun 2015.

[112] Man Huon Han, Elena Gonzalo, Neeraj Sharma, Juan Miguel López del Amo, Michel Armand, Maxim Avdeev, Jose Javier Saiz Garitaonandia, and Teófilo Rojo. High-Performance P2-Phase Na 2/3 Mn 0.8 Fe 0.1 Ti 0.1 O 2 Cathode Material for Ambient-Temperature Sodium-Ion Batteries. *Chem. Mater.*, 28(1):106–116, jan 2016.

[113] D. Carlier, J. H. Cheng, R. Berthelot, M. Guignard, M. Yoncheva, R. Stoyanova, B. J. Hwang, and C. Delmas. The P2-Na2/3Co2/3Mn1/3O2 phase: structure, physical properties and electrochemical behavior as positive electrode in sodium battery. *Dalt. Trans.*, 40(36):9306, 2011.

[114] Marie Guignard, Dany Carlier, Christophe Didier, Matthew R. Suchomel, Erik Elkaïm, Pierre Bordet, Rodolphe Decourt, Jacques Darriet, and Claude Delmas. Vanadium Clustering/Declustering in P2-Na 1/2 VO 2 Layered Oxide. *Chem. Mater.*, 26(4):1538–1548, feb 2014.

[115] C. J. Ballhausen. *Ligand Field Theory.* McGraw-Hill, New York, 1962.

[116] Mariette Hellenbrandt. The Inorganic Crystal Structure Database (ICSD)-Present and Future. *Crystallogr. Rev.*, 10(1):17–22, jan 2004.

[117] Ryohei Morita, Kazuma Gotoh, Mika Fukunishi, Kei Kubota, Shinichi Komaba, Naoto Nishimura, Takashi Yumura, Kenzo Deguchi, Shinobu Ohki, Tadashi

Shimizu, and Hiroyuki Ishida. Combination of solid state NMR and DFT calculation to elucidate the state of sodium in hard carbon electrodes. *J. Mater. Chem. A*, 4(34):13183–13193, 2016.

[118] V. L. Chevrier and G. Ceder. Challenges for Na-ion Negative Electrodes. *J. Electrochem. Soc.*, 158(9):A1011, 2011.

[119] Zhi Wei Seh, Jie Sun, Yongming Sun, and Yi Cui. A Highly Reversible Room-Temperature Sodium Metal Anode. *ACS Cent. Sci.*, 1(8):449–455, nov 2015.

[120] S Basu. Ambient temperature rechargeable battery, 1983.

[121] R. Yazami and Ph. Touzain. A reversible graphite-lithium negative electrode for electrochemical generators. *J. Power Sources*, 9(3):365–371, jan 1983.

[122] Yuanyue Liu, Boris V. Merinov, and William A. Goddard. Origin of low sodium capacity in graphite and generally weak substrate binding of Na and Mg among alkali and alkaline earth metals. *Proc. Natl. Acad. Sci.*, 113(14):3735–3739, apr 2016.

[123] Ping-chun Tsai, Sai-Cheong Chung, Shih-kang Lin, and Atsuo Yamada. Ab initio study of sodium intercalation into disordered carbon. *J. Mater. Chem. A*, 3(18):9763–9768, 2015.

[124] Chen Ling and Fuminori Mizuno. Boron-doped graphene as a promising anode for Na-ion batteries. *Phys. Chem. Chem. Phys.*, 16(22):10419–24, jun 2014.

[125] Yang Wen, Kai He, Yujie Zhu, Fudong Han, Yunhua Xu, Isamu Matsuda, Yoshitaka Ishii, John Cumings, and Chunsheng Wang. Expanded graphite as superior anode for sodium-ion batteries. *Nat. Commun.*, 5, jun 2014.

[126] Denis Y. W. Yu, Petr V. Prikhodchenko, Chad W. Mason, Sudip K. Batabyal, Jenny Gun, Sergey Sladkevich, Alexander G. Medvedev, and Ovadia Lev. High-capacity antimony sulphide nanoparticle-decorated graphene composite as anode for sodium-ion batteries. *Nat. Commun.*, 4, dec 2013.

[127] Claire Hérold, Albert Hérold, and Philippe Lagrange. Ternary graphite intercalation compounds associating an alkali metal and an electronegative element or radical. *Solid State Sci.*, 6(1):125–138, jan 2004.

[128] Birte Jache and Philipp Adelhelm. Use of Graphite as a Highly Reversible Electrode with Superior Cycle Life for Sodium-Ion Batteries by Making Use of Co-Intercalation Phenomena. *Angew. Chemie Int. Ed.*, 53(38):10169–10173, sep 2014.

[129] Haegyeom Kim, Jihyun Hong, Young-Uk Park, Jinsoo Kim, Insang Hwang, and Kisuk Kang. Sodium Storage Behavior in Natural Graphite using Ether-based Electrolyte Systems. *Adv. Funct. Mater.*, 25(4):534–541, jan 2015.

[130] Sébastien Pruvost, Claire Hérold, Albert Hérold, and Philippe Lagrange. Co-intercalation into graphite of lithium and sodium with an alkaline earth metal. *Carbon N. Y.*, 42(8-9):1825–1831, jan 2004.

[131] Laurence Antoine, Jean-Claude Gachon, Vera A. Nalimova, Dmitri E. Sklovsky, Alexei Filatov, and Daniel Guerard. On the Ternary System Graphite-Sodium-Potassium. *Mol. Cryst. Liq. Cryst. Sci. Technol. Sect. A. Mol. Cryst. Liq. Cryst.*, 340(1):65–70, mar 2000.

[132] Laurence Antoine, Raphaël Janot, Alexei Filatov, Dmitri E Sklovsky, Vera A Nalimova, and Daniel Guérard. Behaviour of NaK2-graphite powders at various pressures. *Carbon N. Y.*, 40(4):589–596, apr 2002.

[133] Kyuho Lee, Éamonn D. Murray, Lingzhu Kong, Bengt I. Lundqvist, and David C. Langreth. Higher-accuracy van der Waals density functional. *Phys. Rev. B*, 82(8):081101, aug 2010.

[134] P. Ganesh, Jeongnim Kim, Changwon Park, Mina Yoon, Fernando A. Reboredo, and Paul R. C. Kent. Binding and Diffusion of Lithium in Graphite: Quantum Monte Carlo Benchmarks and Validation of van der Waals Density Functional Methods. *J. Chem. Theory Comput.*, 10(12):5318–5323, dec 2014.

[135] Lin-gun Liu. Compression and polymorphism of potassium to 400 kbar. *J. Phys. Chem. Solids*, 47(11):1067–1072, jan 1986.

[136] M. Winter. WebElements Ltd, 2017.

[137] T Nakajima, M Molinier, and M Motoyama. Structure of fluorine-graphite intercalation compounds. *Carbon N. Y.*, 29(3):429–437, 1991.

[138] A. M. Panich and T. Nakajima. Physical Properties and C-F Bonding in Fluorine-Graphite Intercalation Compounds as Seen by NMR. *Mol. Cryst. Liq. Cryst. Sci. Technol. Sect. A. Mol. Cryst. Liq. Cryst.*, 340(1):77–82, mar 2000.

[139] Xuanpeng Wang, Xiaoming Xu, Chaojiang Niu, Jiashen Meng, Meng Huang, Xiong Liu, Ziang Liu, and Liqiang Mai. Earth Abundant Fe/Mn-Based Layered Oxide Interconnected Nanowires for Advanced K-Ion Full Batteries. *Nano Lett.*, 17(1):544–550, jan 2017.

[140] Yuya Hironaka, Kei Kubota, and Shinichi Komaba. P2- and P3-K x CoO 2 as an electrochemical potassium intercalation host. *Chem. Commun.*, 2017.

[141] Takeshi Inoshita, Kenji Nakao, and Hiroshi Kamimura. Electronic Structure of Potassium-Graphite Intercalation Compound: C 8 K. *J. Phys. Soc. Japan*, 43(4):1237–1243, oct 1977.

[142] Haegyeom Kim, Jae Chul Kim, Shou-Hang Bo, Tan Shi, Deok-Hwang Kwon, and Gerbrand Ceder. K-Ion Batteries Based on a P2-Type K 0.6 CoO 2 Cathode. *Adv. Energy Mater.*, page 1700098, apr 2017.